TAMPEREEN TEKNILLINEN YLIOPISTO
TAMPERE UNIVERSITY OF TECHNOLOGY

TEEMU SAARINEN
DETERMINING REACTIVITY PARAMETERS FOR TWO BIOMASS
FUELS

Master of Science Thesis

Examiners: Prof. Antti Oksanen and
D.Sc. Henrik Tolvanen
Examiners and topic approved by
the Faculty Council of the Faculty of
Engineering Sciences on 9th Sep-
tember 2015

ABSTRACT

TEEMU SAARINEN: Determining reactivity parameters for two biomass fuels
Tampere University of Technology
Master of Science Thesis, 95 pages, 4 Appendix pages
December 2016
Master's Degree Programme in Automation technology
Major: Powerplant and combustion technology
Examiners: Prof. Antti Oksanen, D.Sc. Henrik Tolvanen

Keywords: biomass, CFD, char oxidation, drop tube reactor, Fluent, pulverized biomass, pyrolysis

Lacking resources of fossil fuels and a global concern of the climate change have compelled to search for alternative fuels having less carbon footprint than fossil fuels. Biomass has proven to be one promising alternative for many fossil fuels, e.g. coal, oil and natural gas which are most commonly used in burner fired boilers in power plant solutions. In order to use pulverized biomass in the boiler applications, a careful design is needed for reducing effort later in the start-up phase and preventing unwanted surprises with the boiler functionality, such as lowered availability or high amount of unburned particles in the flue gas.

Computational fluid dynamics has become popular in designing power plant solutions. A CFD program Ansys Fluent is commonly used nowadays and it has many particle combustion models already programmed. Thus, using the combustion modeling of Fluent is less time-consuming and highly cost-efficient way to simulate biomass conversion in burner applications. However, the particle combustion models of Fluent have originally been developed for pulverized coal combustion which differs greatly from that of pulverized biomass. Investigating applicability of the combustion setup of Fluent to simulate the biomass conversion is in interest and it is the main issue of this thesis.

Reactivity parameters for two different biomass fuels were determined by fitting the output of the model using the similar modeling structure as Fluent into the experimental data. This study is divided into the experiments conducted with a drop tube reactor in Tampere University of Technology, and optimizing the reactivity parameters with the model. In order to model the particle combustion similarly as it is conducted in Fluent, all the same assumptions and switching conditions of the models were used, even though they proved to be inaccurate and rather coarse. A great effort was made in investigating the modeling details from the product support of Ansys.

The experiments were conducted successfully and the modeling results were mostly promising. With the relatively coarse model most of the experiments were described well. However, assumptions made in the modeling phase resulted in incapability of the model to describe the conversion process if plenty of oxygen was present. In addition, some of the experiments were not so successful due to too small test reactor or mistakes made during the experiments. Many targets for development were found in almost every section of the thesis which could improve the accuracy of the modeling results in the future.

TIIVISTELMÄ

TEEMU SAARINEN: Kahden eri biomassan reaktiivisuusparametrien selvittäminen
Tampereen teknillinen yliopisto
Diplomityö, 95 sivua, 4 liitesivua
Joulukuu 2016
Automaatiotekniikan diplomi-insinöörin tutkinto-ohjelma
Pääaine: Voimalaitos- ja polttotekniikka
Tarkastajat: prof. Antti Oksanen, TkT Henrik Tolvanen

Avainsanat: Biomassa, CFD, Fluent, hiilen hapettuminen, pudotusputkireaktori, pyrolyysi

Fossiilisten polttoaineiden ehtyminen ja yleinen huoli ilmastonmuutoksesta ovat pakottaneet etsimään vaihtoehtoisia polttoaineita, joiden hiilijalanjälki on pienempi. Biomassasta on tullut vaihtoehto monille fossiilisille polttoaineille, ja sitä voidaan käyttää korvaamaan hiiltä, maakaasua tai öljyä, joita energiantuotannossa käytetään usein poltinsovelluksissa. Biomassan käyttö voimalaitoskattiloissa tulee kuitenkin suunnitella huolellisesti, jotta vältytään ikäviltä yllätyksiltä, kuten hyötysuhteen tai käytettävyyden laskulta.

Laskennallisesta virtaussimuloinnista (CFD) on tullut suosittu työkalu erilaisten polttoprosessien suunnittelussa. CFD-ohjelmisto Ansys Fluent on nykyisin suosittu virtauksen ja palamisen simuloinnissa, ja se sisältää monia valmiiksi ohjelmoituja malleja partikkelin palamisen simulointiin. Näiden valmiiden mallien hyödyntäminen biomassan konversioprosessin mallintamisessa olisi siten erittäin suoraviivaista ja kustannustehokasta. Fluentin partikkelin palamismallit on kuitenkin alun perin kehitetty hiilen pölypolton simulointiin, mistä biomassan pölypoltto poikkeaa huomattavasti. Tämän työn päätavoite on tutkia Fluentin mallien soveltuvuutta pölymäisen biomassan palamiseen.

Tässä työssä selvitettiin kahden eri biomassan reaktiivisuusparametrit sovittamalla partikkelin palamista kuvaavan mallin ulostulo kokeelliseen dataan. Työ jakautui kahteen osioon, joista ensimmäinen koostui biomassan palamiskokeista pudotusputkireaktorilla Tampereen Teknillisen Yliopiston laboratoriotiloissa. Toinen osa-alue oli biomassan palamisen mallintaminen, missä tarkoitus oli mallintaa kiinteän polttoaineen palaminen käyttäen samoja mallioletuksia ja yksinkertaistuksia kuin Fluent, jotta mallin avulla saatavat reaktiivisuusparametrit olisivat mahdollisimman yhteensopivia CFD-simulointeihin. Mallioletuksien selvittämisessä turvauduttiin Ansyksen tuotetuen asiantuntijapalveluihin, jotta työssä käytetty malli kuvaisi partikkelin konversioprosessia mahdollisimman samankaltaisesti kuin Fluent.

Kokeet onnistuivat hyvin ja reaktiivisuusparametrien optimointi oli suurelta osin onnistunutta. Suhteellisen yksinkertaisella mallilla ja karkeilla oletuksilla oli mahdollista kuvata biomassan palaminen hyvin. Kuitenkin karkeat mallinnusoletukset näkyivät selvästi mallinnettaessa palamista korkeassa happipitoisuudessa. Lisäksi kaikki kokeet eivät täysin onnistuneet johtuen liian pienestä testireaktorista ja epätarkkuuksista mittauksissa. Työn aikana löydettiin monia kehityskohteita, joiden avulla tulosten tarkkuutta voitaisiin parantaa tulevaisuudessa.

PREFACE

TABLE OF CONTENTS

APPENDIX A: The code for particle combustion model

APPENDIX B: Optimization software for two-competing rates pyrolysis model

TABLE OF FIGURES

LIST OF SYMBOLS AND ABBREVIATIONS

CCS	Carbon capture and storage
CFD	Computational fluid dynamics
CO	Carbon monoxide
CO_2	Carbon dioxide
DAF	Dry ash free
DTR	Drop tube reactor
PCC	Pulverized coal combustion
TGA	Thermogravimetric analysis

A	Frequency factor	1/s
A_p	Particle surface area	m^2
Bi	Biot number	-
c_p	Specific heat	kJ/kgK
C_1	Diffusion rate constant	1/s
C_2	Pre-exponential factor of char oxidation	J/molK
d	Diameter	m
$\bar{d}$	Mean diameter	m
d_p	Particle diameter	m
D_0	Diffusion constant	$s/K^{0.75}$
E_a	Activation energy	J/mol
E_r	Activation energy of char oxidation	J/mol
h	Convective heat transfer coefficient	W/m^2K
h_{react}	heat released in chemical reaction	kJ/kg
k	Kinetic rate	1/s
k_s	Heat conductivity of a solid substance	W/mK
k_∞	Heat conductivity of surrounding fluid	W/mK
L	Characteristic length	m
$m\text{-}\%$	Mass percent	%
m_a	Mass of ash	kg
m_p	Mass of particle	kg
m_v	Mass of volatiles	kg
m_w	Mass of water	kg
n	Spreading factor	-
Nu	Nusselt number	-
Pr	Prandtl number	-
R	Kinetic rate of char oxidation	1/s
R_u	Gas constant	J/molK
R_1	Kinetic rate of fast pyrolysis	1/s
R_2	Kinetic rate of slow pyrolysis	1/s
Re_d	Particle Reynolds number	-
p_{ox}	Partial pressure of oxidizer	Pa
t	Time	s
T	Temperature	K
T_{final}	Final temperature	K
$T_{initial}$	Initial temperature	K
T_p	Particle temperature	K

X_{daf}	Conversion of dry ash free basis	-
α_1	yield factor of fast pyrolysis	-
α_2	yield factor of slow pyrolysis	-
Δu	Slip velocity	m/s
Δt	Time step	s
ε_p	Particle emissivity	-
θ_R	Radiative temperature of surroundings	K
μ	Dynamic viscosity of fluid	kg/ms
ρ_P	Particle density	kg/m^3

1. INTRODUCTION

Coal-fired power production is the largest single electricity production technology in the world. Over 40 % of the world's electricity is produced nowadays by coal-firing units and the volume is increasing. [1, 2] Due to the limited resources of fossil fuels and global awareness of the climate change, use of coal and another fossil fuels in power generation is tried to be avoided while using alternative fuels, which have less or none carbon footprint, are under increasing investigation. After all, most of the world's energy is produced by combustion processes, and thus it is obvious that the importance of combustion in the energy production remains significant for a long time in the future. [3] Biomass has potential to replace fossil fuels in order to decrease the greenhouse gas emissions because biomass is considered as a carbon neutral fuel and it can be utilized in the coal fired plants with minimal modifications. [4]

Using biomass to replace coal in pulverized fuel combustion is in great interest due to the already existing technology and infrastructure. Nevertheless, biomass has many different properties compared to coal and different biomasses have also deviating properties [4]. Thus, it is important to determine the combustion and fouling properties of different biomasses already in the design phase using experimental data. Combustion properties can be later on used e.g. in numerical modelling or in the solid fuel combustion simulation in full-scale industrial boilers with computational fluid dynamics (CFD). CFD has nowadays become popular and it is considered as a fast and cost-effective tool in designing different processes [5]. Although, in CFD simulations the fuel properties are needed as initial values for the simulation and fuel reactivity is among these properties. The reactivity parameters are fuel dependent, and therefore they have to be determined experimentally for different fuels.

Reactivity of different biomasses has been investigated previously in many studies with numerous different measuring setups. Many different models for sub-processes of combustion have been used and reasonable accuracy has been obtained between the models and experiments. The obtained reactivity parameters for the same fuel may still vary a lot between the researches and they depend on how the combustion process is modeled. [6-12] An important factor is how the sub-processes are connected together, may they be active simultaneously or do they proceed one after another. The particle combustion modeling setup in determining the reactivity parameters should be the same as in the CFD software with which the parameters are planned to be used.

Ansys Fluent is a widely used CFD software today for modeling different combustion processes. However, Fluent includes only models developed for pulverized coal com-

bustion, and thus it is in great interest to see how they are capable of describing combustion of solid biomass particles. In this thesis particle combustion process was modeled with a similar setup which Fluent uses, and already existing and commonly used sub-models for pyrolysis and char oxidation were used. Fluent handles the combustion phases as consecutive processes, and therefore the modeling has to take into consideration that assumption as well. Fluent also uses several other simplifications and conditions for the sub-models which are not taken into account in most investigations of the reactivity parameters. However, modeling has to be conducted exactly as it is implemented in the CFD software with which the results are planned to be used in order to obtain suitable parameters for simulations.

The most time consuming part of this thesis was to achieve experimental data of combustion of two different biomass fuels. The pelletized biomasses were ground and particles of different sizes were tested separately. Both biomasses are widely used or planned to be used in co-firing biomass with coal. The experiments were conducted with the drop tube reactor in the laboratory of Tampere University of Technology and they contained pyrolysis measurements in two different temperatures and combustion experiments in two oxygen concentrations. This experimental data was then used to achieve the reactivity parameters for the fuels by using the model for solid fuel combustion. The model output was tuned to match the experimental results by changing the reactivity parameters. The results of this thesis work, i.e. the reactivity parameters, were used as initial values for the other thesis work which started meanwhile and of which goal was to implement the reactivity parameters in a CFD simulation of a full-scale boiler. M.Sc. Niko Niemelä started his thesis in the halfway of this thesis and much co-operation was included in these two theses.

At first in this thesis some challenges in energy production in the world are introduced. The dependence of fossil fuels and their effect on the climate change are presented, and also some suggestions to replace fossil fuels with biomass are expressed. In the third chapter properties of biomass fuels are explained from the view of combustion technology and also the pelletized biomass is introduced. Introduction to solid fuel combustion is expressed and the different phases of solid fuel combustion are classified in the fourth chapter. In the fifth chapter the modeling of solid fuel combustion is presented and the model used in this thesis is introduced. After this the equipment which is used in handling the fuel is presented. A setup considers shapes of the fuel particles identifying imaging based setup and the experimental apparatus for the combustion tests. The experimental data is presented in the seventh chapter. Finally, the modeling results and discussion on the results are presented in the eighth chapter.

2. BIOMASS REPLACING FOSSIL FUELS

Most of the world's energy is produced by combustion processes, and therefore the importance of combustion in energy production remaining significant for a long time in the future is obvious [3]. The energy in firing solutions is generally produced by combusting fossil fuels [1]. World's total primary energy supply by fuel from 1971 to 2013 is presented in Figure 2.1. The figure illustrates the fact that the energy consumption is increasing steadily and will increase presumably for a long time in the future. It can also be seen from the figure that the fossil fuels are the three largest fuel groups and in 2013 they represented over 81 % of the total primary energy supply of the world [1]. This illustrates the fact how dependent the world is on the fossil fuels. The fourth largest primary energy supply group seems to be biofuels and waste in Figure 2.1 with 10 % share. However, it must be noticed that the most of this is being traditional biomass in non-OECD countries in the building sector. Biofuels and waste contribute only approximately 5 % of the total primary energy supply. [13]
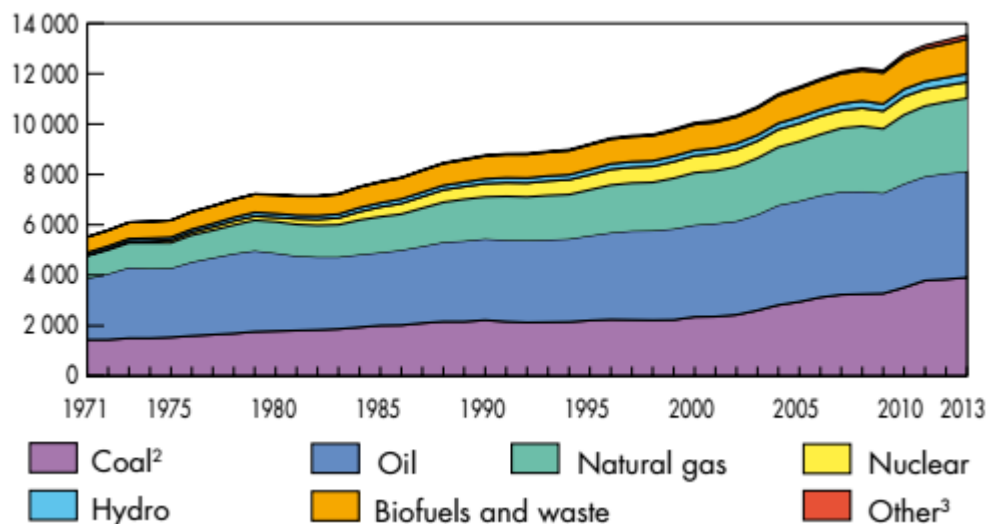
Figure 2.1. Total primary energy supply of the world by fuel [1].

Supplies of the fossil fuels are limited. Therefore, searching for other energy sources already before fossil fuels come to an end is beneficial. Even more recent concern is the climate change due to greenhouse gas (GHG) emissions, most because of fossil fuels. Greenhouse gases prevent the heat from the sun to radiate back to the space causing similar effect as a greenhouse has inside of it. This is noticed worldwide and actions towards it are required and yet planned. Carbon dioxide is the most common greenhouse gas and coal combustion is the largest single source of that with nearly 44% share worldwide in 2013. The next ones are obviously oil and natural gas, and these three

form 99.5% of the world's CO_2 emissions. [1] In Figure 2.2 the electricity generation of the world by fuel is presented.
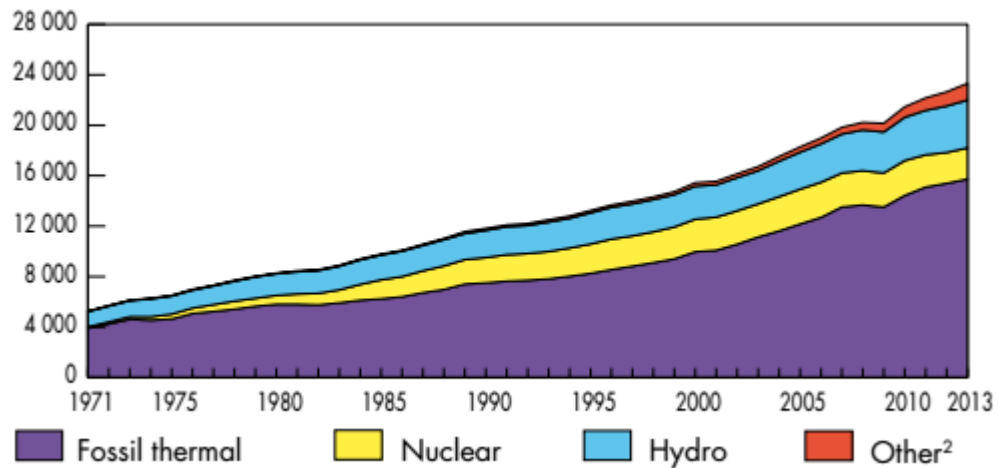
Figure 2.2. World electricity generation by fuel [1].

It can be clearly seen from Figure 2.2 that electricity is generated mainly with the three previously mentioned polluters (fossil thermal). They represented nearly 68 % of all electricity generation in 2013 and most of it, over 40% of the world's electricity, was generated by coal. In summary, coal is the largest single polluter with nearly 44% share of the global CO_2 emissions and the most of it, over 76%, is used in electricity generation. [1] In order to decrease CO_2 emissions, a great potential is in coal-fired power units.

This thesis was a part of a larger project of Tekes and Cleen ltd. in which the goals were to implement sustainable bioenergy solutions in the future bio-economy. Thus, adjustable power generation with biomass is needed in addition to wind and solar energy. Biomass can be used to replace coal and other fossil fuels in electricity generation and in other applications, and biomass in pulverized fuel combustion is introduced at first in this chapter. In the second sub-chapter summarizes advantages and dis-advantages of using biomass in power generation generally.

2.1   Biomass in pulverized fuel combustion

Most of the large scale coal fired power stations, well over 90 % of coal fired capacity, use pulverized coal combustion (PCC). In PCC coal is ground to a fine powder which is blown with a part of the combustion air into the boiler. In the large scale boiler there are several coal burners and typically combustion takes place at temperature levels around 1300 - 1700 ºC. There are different ways to locate burners inside the boiler and in horizontal firing wall-mounted burners may be positioned on one side or on opposite sides of the combustion chamber. Burners may also be located in the corners of the walls so

that flow field in the combustion chamber is highly rotating. This type of construction is called tangential firing. [14]

There is a huge capacity of existing coal fired power production worldwide. Therefore, the most obvious way to reduce the use of coal, and so on GHG emissions, would be replacing coal in pulverized combustion with suitable fuel having less carbon footprint. Biomass is a solid carbon neutral fuel and traditional biomass, e.g. fuelwood, has been the energy source for cooking and direct heating for a long time. Thus, using biomass in PCC boilers is an obvious option in order to replace coal and the GHG emissions. Mixing biomass and coal could be implemented by using direct or indirect co-firing. In the direct co-firing the pulverized biomass is fed directly into the boiler. The biomass may be mixed with coal before the pulverizing mills or separate mills could be used. After that the biomass coal mixture is blown to the boiler using the same burner. Separate mills, fuel lines and burners can also be used for biomass. Indirect co-firing refers to the technique in which biomass is at first gasified and the bio gas is fed into the boiler with coal. [15]

Biomass co-firing has been investigated widely. A comprehensive study of substituting coal with biomass in pulverized coal fired combined heat and power (CHP) facilities in Finland has been conducted by VTT in 2011. The results of the investigation showed that coal could be substituted by original biomass, e.g. sawdust, 5 % tops and up to 15 % with pelletized biomass without major investments on the fuel lines of the boiler. If the separate "wood-line" as a fuel line was used the share could be as high as 30 % and even 50 % of coal could be replaced with bio-oil or with gasified biomass. [16] International Energy Agency (IAE) has reported that more than 100 pulverized coal fired power plants worldwide have been used the co-firing coals with different biomasses [17].

Even though biomass coal co-firing has been investigated and tested worldwide the present co-firing is still limited. There are major differences between biomass and coal, and especially the size of pulverized biomass has been shown to be problematic in pulverized fuel firing. [18] Biomass fuel preparation is much more difficult than that of coal due to the fibrous structure of biomass. Therefore, the best way for fuel preparation is generally in separate systems in which biomass is prepared as a separate fuel. The size reduction of biomass is usually more energy requiring than that of coal and biomass particles cannot be reduced to the same particle size than coal particles. However, it is impractical to reduce the size of the biomass particles to the size of coal powder because of biomass has more volatiles, which are released typically in relatively short period of time, than coal. [4] Thus, biomass particles do not have to be ground into as fine powder as coal in order to achieve the same conversion rate of the fuel. In addition, the pulverizing mills can grind much less biomass than coal, for which they are originally developed. When biomass is fed to grinder designed for coal the net output of the mill reduces accordingly. Therefore, the plant must have extra grinding capacity in order to operate at the full thermal input with increasing share of biomass. [15] A sufficient particle

size has to be selected in order to maintain high enough conversion rate of biomass at a reasonable cost [9]. Pneumatic transportation of biomass is also much more erosive and abrasive than that of coal. [4]

Biomass particle size is the main issue in determining how biomass is injected into the boiler. If the biomass particles are injected at low burner levels they have a risk to fall into the bottom of the boiler without burning. However, this effect can be eliminated with the well-tuned fuel preparation system. On the other hand, if the biomass particles are injected from the highest burners into the boiler they may not have enough residence time to burnout completely before the heat surfaces in the flue gas channel. Therefore, the most common way to inject biomass into the boiler is to use the mid-level burners avoiding the burners in the corners, thus preventing the biomass particles from hitting the boiler walls. It is also a good practice to mix some biomass to coal for each burner because the flows from different burners do not mix well. Therefore, high biomass content of the burners can be distinguished clearly in the flue gas channel as fouling of the heat exchanger area. [4]

According to simulations the small biomass particles follow the flow direction of the gas phase well while the medium size particles drop at first but due to mass loss of releasing the volatiles the drag raises them upwards eventually. The very large particles drop into the bottom of the furnace before burnout. If the particles do not burnout completely in the combustion chamber, they hit the super heater pipes. This depends mostly on the particle size and residence time of the particles in the furnace. Increase of density and moisture can in some cases even raise the burnout rate due to increased residence time of the biomass particles of upper level burners. Particles larger than 4 mm will drop into the bottom of the furnace without burning in all firing levels. [19]

Direct co-firing biomass with coal represents a short-development-time and low-risk option for energy production in order to increase renewable power generation. Co-firing makes use of the old existing infrastructure with minimal modifications and investments on the plant. Costs of co-firing make it favorable technique compared to any other renewable energy production option. [4] E.g. the gasification of biomass leads to higher efficiency, but requires new plants and technique. Co-firing biomass with coal or even replacing coal completely with biomass in the existing power plants is much more cost-efficient and economical way to produce electricity with biomass. [20] Compared to carbon capture and storage (CCS) co-firing provides much more immediate reduction of GHC emissions. Even if the issues of CCS would have overcome, the electricity generation cost would still be significantly higher with CCS than biomass co-firing. This phenomenon is illustrated in Figure 2.3. [15]
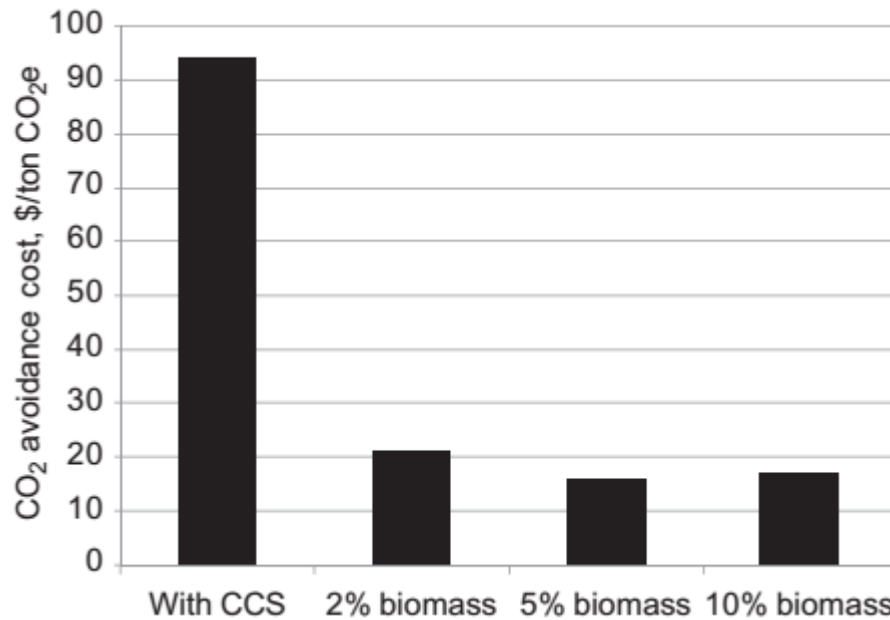
Figure 2.3. Costs of CO2 reduction by CCS and biomass coal co-firing [15].

However, the costs of CCS and biomass co-firing with coal are not totally comparable in Figure 2.3 due to the fact that CCS aims to remove carbon dioxide completely form the flue gas but with biomass coal co-firing only reduction of CO_2 emissions could be achieved. Further increase in the share of biomass would increase the cost of CO_2 reduction and with 100 % fuel switch the costs of biomass firing are significantly higher than those presented in Figure 2.3. Several large modifications are required to an old boiler, e.g. replacing the entire fuel firing and handling system, in order to adapt the boiler for completely different fuel. In addition to the cost of modifications, a long downtime of the boiler is required in order to get all the modifications done. Furthermore, the net output of the plant could reduce as much as 40 % with the switch from coal to biomass which lowers the plant efficiency accordingly. [15] After all, the costs of both techniques, i.e. CCS and 100 % biomass-firing, are notably higher than those of pure coal-firing or biomass coal co-firing, and thus the least expensive technique is dependent on many factors, e.g. location, fuel prices, fuel availability and existing infrastructure of the plant.

In practice, the possibilities to replace coal with biomass differ much for different power plants. The design values of a boiler affect the maximum portion which could be substituted with biomass without considerable decrease of performance, e.g. net output power, efficiency and power to heat ratio. Also the location of the power plant in its site has a great effect on technical alternatives to implement the receiving and handling of biomass, and how biomass can be brought to the plant area. Co-firing biomass with coal increases the operating expenses of the power plant due to possible decrease of availability and increase of maintenance costs. The cost-effectiveness of the co-firing investment depends on the remaining and annual operating time of the power plant. [16]

In addition to PCC power generation, biomass could be used in burner fired boilers replacing also other fossil fuels, e.g. natural gas and oil. Burner fired boilers are often used as peak, back-up and industrial power plants which require fast load control and start-ups. With pulverized biomass firing the boilers are almost as flexible as with oil or gas. Thus, biomass firing plays a significant role in the future bio-economy in control and back-up power generation. Moreover, the fuel flexibility of the boilers increases due to decreased dependence on the single fuel [21]. However, originally oil or gas-fired boilers require fuel milling system in order to use biomass powder as a fuel which obviously increases the investment cost of the application.

Designing new boilers or adapting the old ones to new fuels requires detailed information of the fuel characteristics. Ash melting and fouling properties are one of the key features but on the other hand the combustion features are important for the simulations of the combustion process. Reactivity of the fuel and the size of the fuel particles especially in the pulverized fuel combustion have a great effect on how complete the combustion process could be. Therefore, detailed information of the fuel reactivity is required in order to optimize the boiler efficiency and availability. [9]

2.2 Advantages and disadvantages of using biomass in energy production

Increasing the use of biomass can lower the GHG emissions into the atmosphere, but the emissions of biomass combustion in general tend to be lower and less noxious than those of coal combustion. Acid emissions, such as nitrogen and sulphur oxides, decrease with increased use of biomass due to the notably lower nitrogen and sulphur content of biomass. [22] Coal may contain relatively much sulphur and nitrogen, but generally the amounts of those in biomass are lower, especially with sulphur [15]. However, emissions in biomass combustion depend on many factors, e.g. the biomass source, fuel characteristics and combustion temperature. The emissions may vary widely with different biomasses. [22]

With low cost biomass residues in energy production the cost of electricity is often competitive with fossil fuel based power generation. [23] However, biomass is yet a low cost fuel only when available as a waste or byproduct of a higher-value product. [24] In addition to cost-effectiveness, utilization of biomass provides many benefits for the local society and people. First of all, the agricultural sector in Western Europe and in the US is producing surpluses of food. In such areas land has been set aside to reduce surpluses. Taking these areas into use by growing crops for energy production utilizes the otherwise empty land. [23] This also helps the stabilization of employment in rural areas and regional development [20]. Increasing the use of biomass can provide useful employment locally both at the bioenergy processing plant and in the agricultural or forest

sector. In addition, producing energy crops may lead to reduced use of fertilizers and pesticides [23].

Nevertheless, significant land take is required to produce a relatively low amount of electricity with biomass, approx. 240 ha of energy forest plantation in order to produce MW_e annually [22]. Furthermore, bulk density and calorific heating value are considerably lower than those of coal, oil and natural gas. This can limit the area within it is cost-effective to source biomass. [13] Thus, biomass must be produced near the power plant which may have a positive impact on energy security. Global crises do not affect the biomass fuel availability but on the other hand the weather may cause some uncertainties to fuel supply. Transport market is also dependent on oil, and thus shorter transportation distances decrease the dependency on the fossil fuels. [22]

Biomass is considered as GHG neutral fuel due to re-capturing of the released CO_2 in the combustion from the atmosphere by the regrowth of new biomass. However, using biomass in combustion replacing coal has no effect on the net GHG emissions without sustainable forest management, i.e. new biomass is replaced where it has been harvested. This sustainability of biomass for energy is the requirement for the zero net GHG emissions and biomass production should not cause e.g. deforestation in any case. [13] After all, the actual CO_2 emissions from biomass combustion are notably higher than those of coal per released energy (t/MJ) [25]. Obviously, there exists a lag between the CO_2 emissions through the combustion and the eventual CO_2 uptake as biomass. This process may take several years and the delay between the CO_2 release and absorption needs to be recognized by the developed world. The developing world is facing the same dilemma as it is consuming its resources of biomass for fuel but does not realize the replacement planting. [23]

Biomass is different to coal in many characteristics. First of all, biomass has relatively low heating values which could be explained by high moisture and oxygen content. The moisture content of biomass is one of the most significant disadvantages of biomass. [24] Freshly cut biomass has usually 40 - 60 m-% moisture and it has to be dried before injecting into the boiler. Biomass is also hygroscopic i.e. even if the biomass is dried it can absorb moisture from its surroundings and the atmosphere. [4] The volatile matter of biomass is also much higher than that of coal. Typically, the volatile matter of coal is 10 - 40 m-%, but some biomasses have over 80 m-% of volatiles according to proximate analysis. [26] Thus, a large part of the biomass combustion occurs in gaseous phase. Moreover, biomass contains typically less ash than average coal. The ash content for woody biomass is usually 1 - 3 m-% and for agro biomass 1 - 9 m-%, but for coal the ash content could be as high as 20 m-% [27]. Almost all the biomass ash exits the pulverized fuel combustion chamber as fly ash. However, biomass ash may cause some serious slagging and fouling in the combustion chamber and heating surfaces due to its high silica and alkali content. [15] More information of the biomass characteristics is represented in the third chapter.

Biomass has low bulk energy density (MJ/m^3) which is only approx. 10 % of that of the most fossil fuels due to low density and heating value of biomass, and thus it requires much more storing capacity than e.g. coal [15]. With torrefaction it is possible to affect the combusting and storing properties. The term torrefaction refers to mild pyrolysis of wood in the presence of little or none oxygen. Typical temperature range in torrefaction is between 200 ºC and 300 ºC in which the biomass undergoes some thermal degradation in order to maximize mass and energy yield of the solid product. [28] Due to torrefaction the energy density of biomass increases decreasing the needed storing capacity. With torrefied biomass the uptake of moisture is very limited due to loss of hydrogen bonds. [18] Increasing the share of torrefied wood in co-firing with coal does not change the combustion that much in furnace scale compared to pure coal firing, especially in co-firing [15]. According to simulations, as the share of torrefied wood in co-firing increases the flame stability seems to fade slowly due to larger particle size of the fuel. Nevertheless, the flame stability was maintained with the torrefied fraction of 50%. [29]

Increasing the use of biomass in coal fired power or heat generation requires still some public support in order to be compatible with coal [16]. According to Veringa [20] in Austria district heating by biomass has increased 6-fold and in Sweden 8-fold due to the actions of federal or local level. Electricity supply from biomass has been rising steadily since 2000, but it is concentrated mostly in OECD countries. [13] In European Union the share of renewable sources of the gross final energy consumption has doubled in ten years since 2004 from 8.4 % to 15.0 %. EU has also set ambitious goals for increasing the share of biomass in energy production up to 20 % by 2020. However, the share of renewables in the energy consumption varies a lot between the member states being at its highest in Sweden (49 %) and lowest in Luxemburg (11 %). [30]

3. FEATURES OF BIOMASS FUELS

In this chapter features of biomass affecting the thermal conversion process are presented. In the beginning of the chapter the definition biomass is shortly explained and the structure of woody biomass is presented. In the first sub-chapter different types of botanical biomasses are represented and their typical features are shown. Biomass has low energy density, and biomass is often pelletized in order to decrease transportation costs and achieve more homogeneous form of biomass. Some features and advantages of pelletizing are represented in the second sub-chapter. In the third sub-chapter the combustion properties and features related to biomass combustion behavior are represented.

The definition of biomass is very complex and finding universally acceptable definition for it is difficult. However, any material derived from plants or animals, that are either living or recently lived, is understood as biomass. Occasionally the waste, e.g. municipal waste, is considered as biomass as well. [15] For simplicity, the definition of biomass is defined in the scope of this thesis as botanical biomass. European committee for standardization has published standard for specification of biomass in which biomass is classified into four categories based on its origin. Three main categories are woody, herbaceous and fruit biomass while the fourth category includes blends and mixtures of biomasses. [31]

Botanical biomass is formed through a process called photosynthesis. Photosynthesis is a conversion of carbon dioxide CO_2 into carbohydrate and oxygen in the presence of sunlight, chlorophyll and water. One mole of oxygen is released for every mole of CO_2 absorbed into carbohydrate or glucose in biomass. Carbohydrates are the building blocks of biomass while chlorophyll serves as a catalyst in the photosynthesis process. [32] Typically less than 1 % of the available solar energy is converted into chemical energy through photosynthesis [23]. Biomass is a complicated mixture of organic materials and small amounts of minerals. The three major components of biomass are fiber or cell wall components, extractives and ash. [32] The cell structure of woody biomass is presented in Figure 3.1.
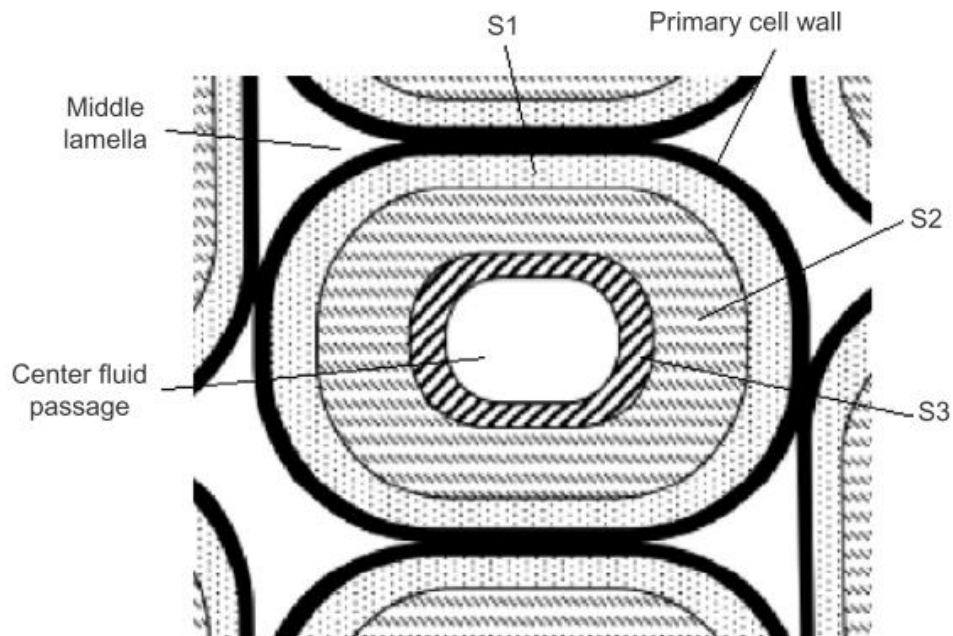
Figure 3.1. *Structure of a wood cell [32].*

Biomass cell wall provides strength to the plant making it able to stand and rise above the ground. Typically, the cell wall consists of carbohydrates and lignin. Carbohydrates are most commonly cellulose and hemicellulose, and they provide strength to the plant. A good example of this type of biomass is a woody plant which is mainly composed of cellulose and lignin. In Figure 3.1 layers S1, S2 and S3 form a so called secondary cell wall. Lignin serves as an adhesive keeping the cells packed together. The middle lamella in Figure 3.1 is mainly composed of lignin. [32] Thicknesses of these layers are between 0.1 μm and 5 μm [34]. The center fluid passage makes the biomass able to move water and extractives from roots to upper parts of a plant. Fluid carrying woody cells are known as fibers. For softwood the average fiber thickness is 33 μm and the length of the fiber is 3 - 8 mm. [32, 33]

Biomass is composed of cellulose, hemicellulose, lignin and other extractives. The amounts of these vary a lot between different biomasses. Cellulose is the most common organic compound on Earth and it is the main structural component of biomass cell walls. The amount of cellulose varies from 33 m-% to 90 m-% for different biomasses. Cellulose has a strong structure that is resistive to hydrolysis. Hemicellulose, on the other hand, has a structure with very little strength: it is random and amorphous. The composition and structure of hemicellulose varies among different biomasses. [32] The distribution of the structural components in the woody biomass cell walls and their layers are presented in Figure 3.2.
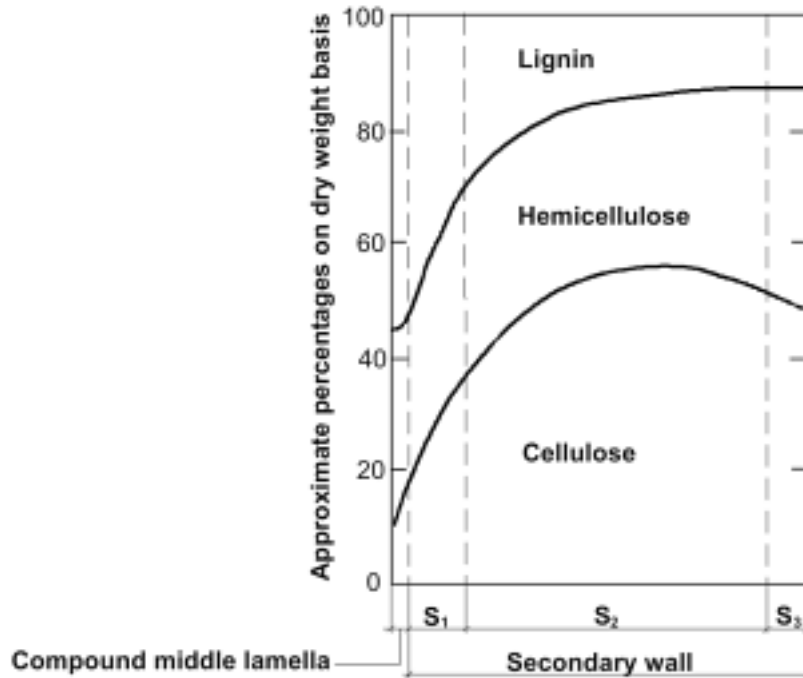
Figure 3.2. *Distribution of cellulose, hemicellulose and lignin within the cell wall layers of softwoods [34].*

The amount of lignin, hemicellulose and cellulose vary in the woody biomass cell wall which can be seen in Figure 3.2. The amount of cellulose is the highest in the middle of the cell wall which naturally gives strength to the fiber. The lignin content increases at the expense of cellulose towards the middle lamella. Lignin is an essential part of secondary cell wall of the plants tying the fibers together.

3.1 Different types of biomasses

Botanical biomass is classified under four sub categories: woody biomass, grasses, fruit biomass, and blends and mixtures of previously mentioned. Trees, bunches and shrubs are considered as woody biomass. [31] Woody forest residues are the most commonly used biomass type in co-firing in originally coal-fired power plants. [4] The growth of woody biomass is usually slow and it is composed of tightly bound fibers [23]. Herbaceous biomass considers plants growing seasonally and shriveling at the end of the growing season. Herbaceous biomasses also include grains growing on the plants. [31] They usually consist of more loosely bound fibers indicating a lower fraction of lignin. [32]

Also fruits can provide appropriate biomass for energy production. They are digestible for humans, but the lignocellulosic body of a fruit tree is not, and thus it can be used as a fuel. The third sub category of fruit biomass considers orchard and horticulture fruit. Also the by-products and residues from the fruit processing industry belong to this category. The fourth sub category is blends and mixtures of different biomasses from the

three other groups. Blends represent intentionally mixed biofuels while mixtures are unintentionally mixed biomasses. The classification is flexible, i.e. the producer or consumer can decide which classification corresponds to the produced or desired fuel best. [31]

Even though woody forest residues represent nowadays the most common fuel in energy production, energy crops represent the future fuel resource. Energy crops are grown exclusively for energy production and they have been investigated widely. For commercial energy farming several crops have been suggested and they cover both woody crops and herbaceous plants. The requirements for the ideal energy crop are low cost, high yield, low nutrient requirement and low energy input to produce. The requirements vary with local climate and soil conditions, and in some areas e.g. water consumption may also be an important factor. [23] Energy crops have usually a short growing period and they are lignocellulosic by nature. Woody herbaceous crops like miscanthus, willow, poplar and switchgrass are broadly used in energy production. [32]

3.2   Pelletized biomass

Biomass has low energy density in terms of mega joule per volume unit. Thus, transportation of biomass is unprofitable, especially compared to coal. In order to increase the energy density of biomass it is commonly compressed into pellets or briquettes with higher density. Due to pelletizing the heating value of biomass may increase by 50 % and the energy density could nearly double compared to raw wood. Thus, pelletizing could make transportation and handling of biomass more compatible with coal. However, if the pellets are stored for a long time they could absorb moisture and thus, loose their strength. In order to prevent the structural weakening of the pellets biomass could be torrefied before or during the pelletizing. This procedure could make the energy density of torrefied pellets three times higher than that of raw wood. [28]

The pellet production process can be divided into three main unit operations. They are drying, grinding and densification. [35] The dryer represents the most expensive plant component. In the dryer chipped biomass is dried to the water content of approx. 10 m-%. The dried biomass is then fed to a grinder which reduces the size of biomass suitable for pelletizing. [36] Typically the biomass is ground to size of 3 - 6 mm before densification. Densification may be conducted with or without external heating of biomass. Barely compressing of biomass into pellets requires some form of external binding agent to hold the pellets together and make the pellet structure strong. With external heat additional ingredients may not be needed due to softening of biomass lignin. Cooling the pellets after compressing them hardens the lignin which holds the particles together and provides a good mechanical strength for pellets. [28]

In central Europe pellets are mainly produced of barkless wood as by-product of industrial processes of forest industry like sawmills. Also newly felled wood is used as a raw

material for pellets. Recently, the interest has focused on pelletizing fast-growing types of trees such as poplars and willows which represent the multi-annual harvesting type of energy crops. Straw and other biomasses from the agriculture sector are also in interest in many areas. In addition, herbaceous energy crops, e.g. miscanthus, are expected to become more common in pelletized form in the future. Due to a large amount of different biomasses the fuel pellet production contains only one third of the forestry and agricultural fuel residues potential. In the 28 EU countries, the annual potential of producing pellets from biomass could be as high as 750 TWh. [37]

3.3 Properties of biomass

3.3.1 Composition

Based on the elementary analysis solid fuels are composed of carbon (C), hydrogen (H), oxygen (O), nitrogen (N), sulphur (S) and inorganic constituents, ash. However, all fuels do not contain all of these elements. [32] In Table 1 compositions of some typical solid fuels are demonstrated. The variation of the fuels in the table is caused by the fact that they contain several different types of fuels which fall into the same category.

Table 1. Typical compositions of some solid fuels [23, 38]

	Wood	Bark	Peat	Coal
Moisture (m-%)	30-45	40-65	40-55	8-12
Ash (m-%)	0.4-0.5	2-3	4-7	5-14
C[*)	48-52	51-66	50-57	56-73
H[*)	6-6.5	6-8.4	5-6.5	3.5-5.5
O[*)	38-42	24-40	30-40	3-18
N[*)	0.5-2.3	0.3-0.8	1-2.7	0.8-1.6
S[*)	0.05	0.05	<0.2	<1.7

*) m-% of dry basis

Biomass consists of multiple complex organic compounds, moisture and a small amount of ash. High moisture content is one of the most significant disadvantages of biomass in combustion processes [24]. Moisture content has a great impact on biomass burnout time [4]. Typical oxygen content of biomass is 35 m-% of the dry basis which could be ten times more than that of coal [24]. Nitrogen content of biomass is usually lower than that of coal but may vary alongside with ash content [4]. Obviously, coal also contains much larger share of carbon than e.g. wood. On the other hand, oxygen and hydrogen

contents of coal are much less than those of wood. The atomic ratio based classification of fuels helps to understand the heating values of different solid fuels. Biomass has much higher H:C and O:C ratios than fossil fuels. [32] This is illustrated in Figure 3.3 where different solid fuels are categorized by their atomic ratios on dry-ash-free (daf) basis. This type of presentation is called Van Krevelen diagram. In the figure an arrow indicating increasing heating value of a solid fuel is marked.
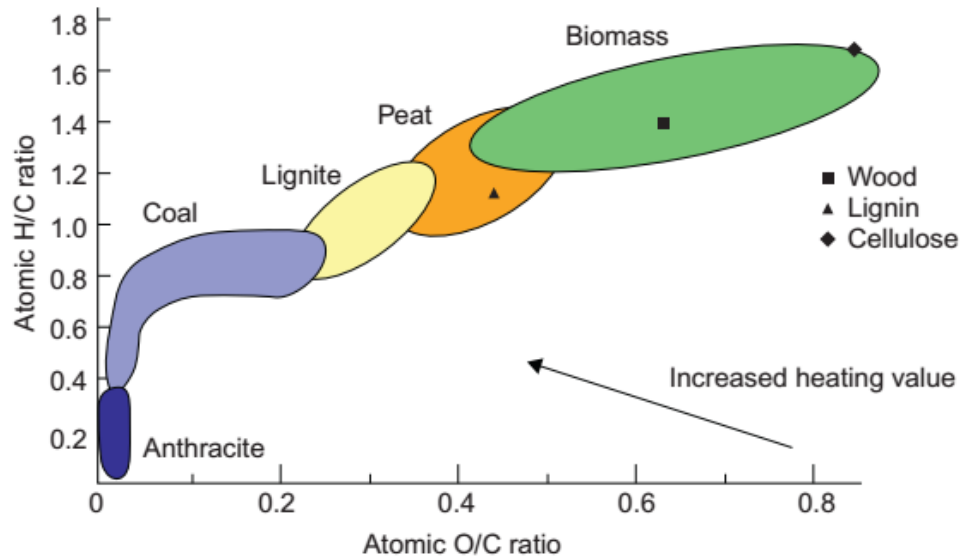
Figure 3.3. Van Krevelen diagram for solid fuels [32].

Biomass represents a wide area in Figure 3.3 due to various types of biomasses. In the figure also the value of lignin and average wood are marked. Both H:C and O:C ratios are relatively high for biomass, and therefore the heating value of wood and other biomasses is relatively low. Lignin has lower O:C ratio and therefore higher heating value. Cellulose again is located on the upper right corner of the area of biomass in the figure indicating lower heating value. Thus, biomasses containing larger fraction of cellulose and hemicellulose have lower heating value than lignin rich biomasses. In contrast, anthracite, being an extremely old coal, has very little oxygen and hydrogen contents giving it high heating value. Anthracite consists of mostly carbon which makes its CO_2 emissions very high. [32] One must remember that the actual carbon dioxide emissions per released energy are notably higher for biomass than for coal if the re-capture of CO_2 by the regrowth of fresh biomass is not taken into account [25].

Besides elementary analysis, proximate analysis is often used in characterization of solid fuels. In proximate analysis only moisture content (M), volatile matter (VM), fixed carbon (FC) and ash content are determined. This is a relatively easy and low-price process to determine the composition of a solid fuel. Volatile matter represents the condensable or non-condensable fraction of the fuel released in a process called pyrolysis. Amount of volatiles is much higher for biomass than for coal, and the typical volatile fraction varies from 60 m-% to over 80 m-% of dry basis with biomass. [32] For coal

the typical fraction of volatiles is around 30 m-% [26]. Fixed carbon represents the reactive matter that remains in the char after pyrolysis. The moisture and ash are excluded from fixed carbon [32].

Ash represents the part of the fuel which does not react in a thermal conversion process such as combustion. Ash is an inorganic part of the biomass containing typically different metals. Different biomasses contain varying amount of ash but generally biomass has less ash than coal. E.g. woody biomass has notably less ash than coal which can be seen in Table 1 but herbaceous biomasses could contain significantly higher ash content than wood. The ash content of biomass varies from less than 1 % to over 20 %. [4, 32] Ash deposit formation represents one of the most significant properties of the fuel impacting boiler design and its usability. Biomass contains typically much higher content of alkalis and chlorine than coal. [32] Alkali metals of biomass ash evaporate in the combustion temperature but condensate on lower temperature heat surfaces of the boiler. This causes slagging and fouling on the colder parts of a furnace and the heat exchanger piping, respectively. [27] Some herbaceous plants also have relatively high silica content which affects slagging by lowering the ash melting temperature. [39] In addition, all the biomass ash may not originate from biomass itself but from the biomass harvesting process. Biomass is often collected from the ground, e.g. in the forest or in the field, which could lead to higher amount of dirt and impurities increasing the silica content. [32]

Chlorine decreases the melting temperature of the ash and on the other hand makes the ash containing a mixture of partly melted alkali sulfates and chlorides extremely corroding. [27] Thus, fouling and corrosion of the combustor are typical issues associated with the biomass combustion [24]. The chlorine content of biomass could be reduced by torrefaction. Even 90 % of the chlorine can be removed from the solid of some hardwoods by 60 minutes of torrefaction. [40] Generally the ash deposit rates in co-firing are although lower than expected due to interactions between alkali from the biomass and sulphur from coal [4].

3.3.2 Thermodynamic properties of biomass fuels

Density is an important factor for any biomass conversion system. However, density can be determined in various different ways depending on how they are. Bulk density is based on the overall volume biomass stack occupies. Thus, the bulk volume includes the volume between biomass particles. [32] Bulk density is an important characteristic in relation to transportation and storing costs [24]. Biomass has considerably lower bulk density than coal being about one fifth that of coal [4].

Apparent density is based on the external volume of biomass particle which includes its pore volume. Thus, apparent volume excludes the pore volume of the biomass particle but not the intrinsic volume between the fibers packed together. Apparent density is the

most common density used in design calculations. It is relatively easy to measure and it represents the actual volume of the biomass particle. [32]

The fibrous structure of woody biomass makes the biomass grinding much harder and more energy demanding than e.g. grinding of coal as mentioned in the second chapter. The size and shape of biomass particles are very different than those of coal. Ground coal is typically fine powder and the coal particles are nearly spherical. Woody biomass on the other hand has much larger particle size and the shapes of the particles are typically more elongated than those of coal. Average particle aspect ratios are typically in range of three to seven depending on the grinding technique and biomass type. [4] If the grinding was able to separate the wood fibers completely the particles could be as long as 8 mm, as mentioned in the beginning of this chapter. Even though that is not the case, it is obvious that in grinding fibers disengage from the matrix structure more easily than they are cut in pieces, thus leading to elongated biomass particles. Torrefaction could lower the energy required for the fine grinding and required energy could be 20 % of that of untreated biomass [41].

A second important thermodynamic property required for thermodynamic calculations is specific heat. It illustrates the heat capacity of a substance. Density of woody biomass does not have much effect on the specific heat of wood species, but temperature and moisture affect strongly specific heat. Specific heat of dry wood (1.3 kJ/kg in 300 K) and that of char coal differ from each other, and correlations as a function of temperature for both exist in library. Specific heat of char coal can be assumed to be the same as that of graphite, i.e. 0.715 kJ/kg in 300 K. [42]

Heating value of a fuel describes how much energy is released in the complete combustion of it in presence of adequate amount of oxygen. Lower heating value (LHV) describes the situation in which all the water formed in combustion is in gaseous phase. Lower heating value of untreated wood is typically in the range of 17-19 MJ/kg while it is for coal between 25 MJ/kg and 30 MJ/kg. Biomass combustion releases much less heat than that of coal, which has been briefly mentioned in the second chapter. With torrefaction the lower heating value of wood can be increased to 18-23 MJ/kg due to the thermal degradation of hemicellulose. Therefore, torrefaction moves the woody biomass towards the lower left corner in Figure 3.3. [18]

4. SOLID FUEL COMBUSTION

Combustion or gasification of solid fuel can be divided into different phases. At first the particle is heated until the temperature reaches the drying temperature and the water in the particle starts to evaporate. After drying the particle undergoes pyrolysis or devolatilization, i.e. releasing the combustible gaseous compounds which burn outside the particle if oxygen is present. These volatiles are different types of hydrocarbons. After the volatiles have released the remaining char burns with a non-visible flame if oxygen is available. When all the combustible material has either released or burned the remaining ash is all that is left. These sequential phases of combustion may occur simultaneously if the particle is large enough. When burning e.g. a log of wood drying, pyrolysis and char oxidation may all occur in the same time under certain circumstances. [26] Phases of combustion of the wood log are illustrated in Figure 4.1.
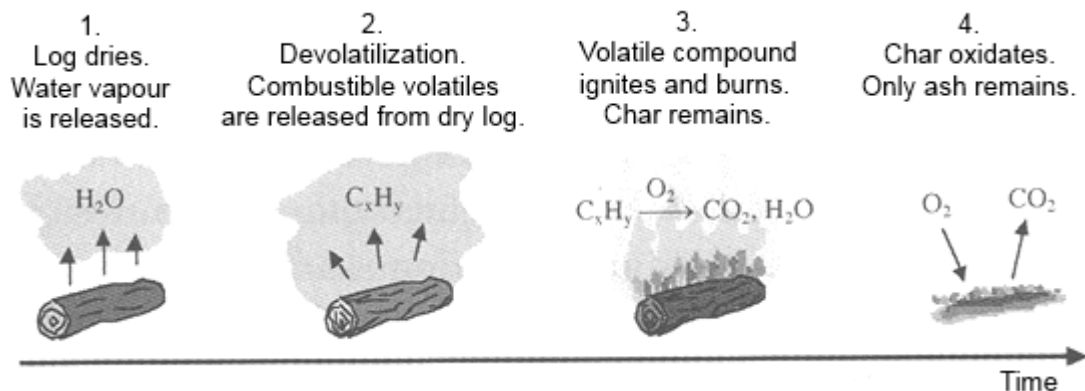
Figure 4.1. Combustion phases of a large wood log burning [3].

In general, biomass combustion differs significantly from that of coal as mentioned in the second chapter. Biomass has relatively low heating value and much higher amount of moisture than coal [4]. Therefore, the drying phase takes significantly longer with biomass than with coal which typically contains very little moisture. The volatile matter of biomass is also much higher than that of coal making the devolatilization phase of combustion more significant for biomass. In the combustion of volatile gases more than 70 % of the overall heat of the biomass combustion is released. However, the high volatile yield also increases ignition stability of biomass. [24] In addition, volatiles of biomass are released more rapidly than those of coal [4]. There is relatively little amount of char and ash left after devolatilization which makes the char oxidation a minor process in the whole biomass combustion.

Biomass particles can be well over 10 times bigger than average coal particles, and thus it is obvious that in a large particle the combustion phases are overlapping even though they could be locally successive processes. Intra-particle heat and mass transfer resistance generate notable temperature gradients inside the particle. [43] Due to the great temperature difference between the center and the surface of the particle, combustion phases do not take place uniformly inside the particle. [19] Ignition of the volatiles released in pyrolysis could also heat the particle and thus accelerate pyrolysis and char oxidation if they are occurring simultaneously [44]. The temperature difference between the particle surface and center could be several hundreds of degrees [4]. Large particle size also generates more resistance to the moisture and volatile matter exiting the particle. Thus, both intra-particle heat and mass transfer are affecting the biomass conversion process. [45]

As mentioned earlier the shapes of biomass particles are highly non-uniform and elongated due to the fibrous structure of biomass. The particle shape affects the heat transfer and conversion of the particle. Spherical particles react much slower compared to cylindrical ones and the differences increase with increasing particle size. The conversion time of a spherical particle could be twice as long as that of a highly elongated one for the particle size more than 10 mm. The effect of particle shape on conversion rate should be more significant for large particles than for smaller ones, but even the particles with sphere-equivalent diameter of 300 μm experience a great difference in conversion rate based on the particle shape. [43] Due to the generation of complex temperature patterns inside the biomass particle, combustion may not proceed uniformly on all particle surfaces. Biomass combustion rates are not controlled by just chemical kinetics but by particle geometry and size as well. Thus, the burning rate of biomass is essentially fuel independent and mass loss is highly sensitive to the initial particle size. [4]

4.1   Devolatilization

When a solid fuel is subjected to heating it starts to decompose, giving a mixture of volatile species and heavier compounds called tars. This phenomenon is called pyrolysis or devolatilization and it occurs when there is either total absence of oxidizer or a limited supply. In pyrolysis the large and complex hydrocarbons of biomass degrade into smaller molecules of gas, liquid and char. The liquid tar, often referred as bio-oil, is usually released in gaseous phase but condensates on a cool surface and it is the main product in many pyrolysis applications. The solid matter after pyrolysis is proceeded completely is called char or bio-char, and it consists of mainly carbon. [46]

Pyrolysis is often considered slightly endothermic i.e. it requires heat in order to proceed. Typically, in combustion processes heat required for pyrolysis is provided by combustion itself but in pyrolysis or gasification applications external heat could be needed to be brought outside the process. [46] Pyrolysis enthalpy depends on raw mate-

rial but for wood it typically is 100 - 200 kJ/kg [47]. For cellulose the value of 538 kJ/kg has been presented in literature [48]. Pyrolysis heat of biomass is dependent on the char yield and pyrolysis could be slightly exothermic in the process in which wood is heated slowly in order to maximize the char yield [26].

Primary decomposition of biomass produces volatiles i.e. non-condensable gases and condensable vapor. The non-condensable products are called the primary gases. The vapors consisting heavier hydrocarbons condense on cool surfaces and they form the liquid yield of pyrolysis. However, liquid products may experience the secondary cracking process forming additional non-condensable gases which are called the secondary gases. The product yield of pyrolysis depends on the physical and chemical characteristics of biomass but also the heating rate, maximum temperature and residence time in high temperature zone affect strongly to pyrolysis products and their yields. [46] Figure 4.2 illustrates the release of volatile gases during pyrolysis of wood. Different gaseous pyrolysis products are released in different temperature ranges.
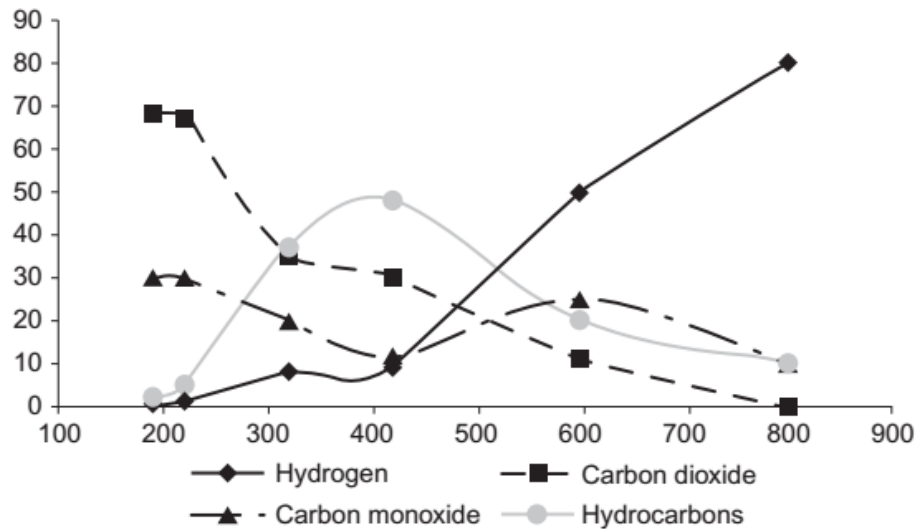
Figure 4.2. Release of different gases during pyrolysis of wood [46].

The composition of biomass has a significant effect on the pyrolysis products. Especially hydrogen-to-carbon ratio of biomass has a significant impact on pyrolysis yield. Most of the biomasses used in co-firing and in other thermal processes are lignocellulosic biomasses which are composed of cellulose, hemicellulose and lignin. All of these components have different temperature ranges of decomposition and their degradation rates are very divergent. In Figure 4.3 degradation rates of cellulose, hemicellulose and lignin as a function of temperature are presented. Cellulose and hemicellulose are the main sources of volatiles in pyrolysis of lignocellulosic biomass. Cellulose is a primary source of condensable vapor and hemicellulose yields more non-condensable gases while lignin degrades more slowly, and therefore affects the char yield of biomass pyrolysis. [46]
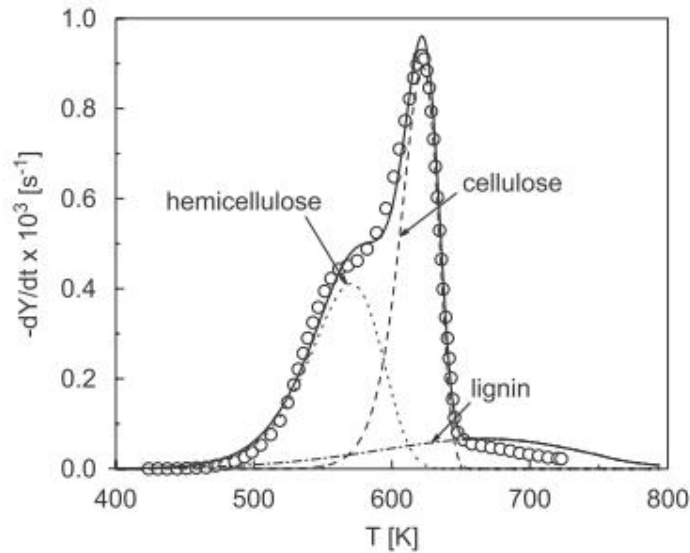
Figure 4.3. *Decomposition temperature ranges and degradation rates of cellulose, hemicellulose and lignin [49].*

Temperature affects the composition of volatiles in pyrolysis. Lignin requires higher temperature in order to degrade which can be observed in Figure 4.3. In addition, high heating rate and high final temperature maximize the gas production during pyrolysis, i.e. lighter hydro-carbons are released. The primary pyrolysis stage takes place in the temperature range of 200 - 600 ºC and most of the vapor is produced in this stage. The secondary cracking of volatiles into char and non-condensable gases takes place after that, in the final stage of pyrolysis. [46]

The volatile yield is strongly dependent on the maximum temperature in which pyrolysis takes place but also on heating rate. Generally, the higher temperature level the more volatiles are released during the pyrolysis. Without secondary reactions the maximum temperature level and the residence time in peak temperature have more effect on the total release of volatiles than heating rate. [50] Temperature has a significant effect on the pyrolysis yield and the composition of tars and gaseous products. The amount of gas products increases at the expense of tars when temperature increases. [51] However, the fast pyrolysis due to high heating rate produces more volatile compound and less char than the slow pyrolysis in the same temperature [52].

The effect of heating rate on biomass pyrolysis is much more significant than it is for coal which may be caused by the normally high cellulose content of biomass. Heating rate has a significant effect on decomposition of cellulose. High heating rate also decreases the time of volatiles for secondary reactions inside the biomass particle, and thus lowers the amount of char and tar. However, it is possible to obtain the maximum heating rate affecting the char yield for a certain biomass. Further increase of heating rate would not affect the char yield due to an additional increase of temperature. [53]

The particle size and shape have an effect on the pyrolysis yield due to their influence on heating rate. Condensable gases experience much less resistance escaping the particle due to small particle size, which also decreases the internal temperature gradient of the particle. [46] Aspherical particles also have larger surface area and smaller thickness leading to higher heating rates, and faster heat and mass transfer inside the particle. The volatile yield may also be dependent on shapes of the particles and near-spherical particles yield less volatiles. [43] Ignition of volatiles accelerates the combustion process [44].

Heat transfer inside the biomass particle plays a significant role in biomass pyrolysis. Biomass particles are usually relatively large, thus creating large temperature gradient inside the particle. According to simulations the temperature difference is particularly high during the maximum pyrolysis. [19] The temperature difference between the particle surface and center could be several hundreds of degrees [4]. Mass transfer affects pyrolysis as well, either existing externally or internally within the particle. The internal resistance occurs when the tars and gases travel inside the particle while the external mass transfer may limit the access of tars through layer surrounding the particle. This has been observed if the pressure outside the particle was raised. Increasing the external pressure decreases the tar yield and on the other hand increases the gaseous product and the char yield. Increased pressure outside the particle increases the residence time of tars in the particle and thus gives more time for secondary reactions to occur. For coals mass transfer may have some effect on pyrolysis product distribution and yields of pyrolysis products, and may affect also the pyrolysis kinetics. However, mass transfer is not a major factor in describing the coal pyrolysis. [54] The modeling results for biomass suggest both intra-particle heat and mass transfer should be taken into account in describing the biomass pyrolysis in details [45].

4.2   Char oxidation

After the volatile compound is released from the solid fuel particle the char residue, which is mainly composed of carbon, remains. Char oxidation or gasification differs greatly from pyrolysis. In pyrolysis the reaction occurs due to heat transfer from surroundings to the particle surface. However, char oxidation is mainly limited by diffusion of the oxidizing molecules to the surface of the particle in which they react heterogeneously with char. Thus, the term surface reaction is also used instead of char oxidation. High temperature of the particle accelerates the surface reaction. Unlike pyrolysis, char oxidation is highly exothermic process. The char oxidation reaction rate of small particles is constrained by chemical kinetics while diffusion of the oxidant through the boundary layer limits the rate of large particles. The time required for char oxidation is directly proportional to the char density. The main reactions of char oxidation are:

$$C(s) + O_2 \rightarrow CO_2 \qquad \Delta h = -32.8 MJ/kg \qquad \text{(R1)}$$

$$C(s) + 0.5 O_2 \rightarrow CO \qquad \Delta h = -9.25 MJ/kg \qquad \text{(R2)}$$
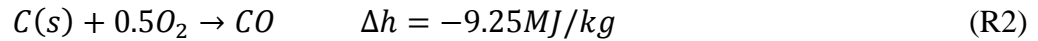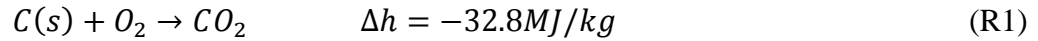
where $C(s)$ represents the char in solid form and Δh is reaction enthalpy. The negative reaction enthalpy is due to the exothermic reactions. [26] Compared to pyrolysis which is endothermic, char oxidation releases much more heat than pyrolysis consumes.

Typically, three regimes for char oxidation are defined. Regime I corresponds the situation in which the chemistry of the combustion is relatively slow and combustion takes place inside the particle. In regime I temperature is low and the combustion is fully controlled by chemistry. Particle diameter remains constant while density lowers and the conversion time is the same for all particle sizes. On the contrary, regime III represents the situation of fast chemistry and the combustion is controlled fully by the diffusion of an oxidizer from surroundings to the particle surface. In this situation combustion occurs in a thin layer on the particle surface and the particle density remains constant while the diameter is decreasing. Regime II is a hybrid of regimes I and II when combustion takes place partially inside the particle. [26] Biomass chars burn under strongly diffusive conditions due to high char reactivity and relatively large particle size [19].
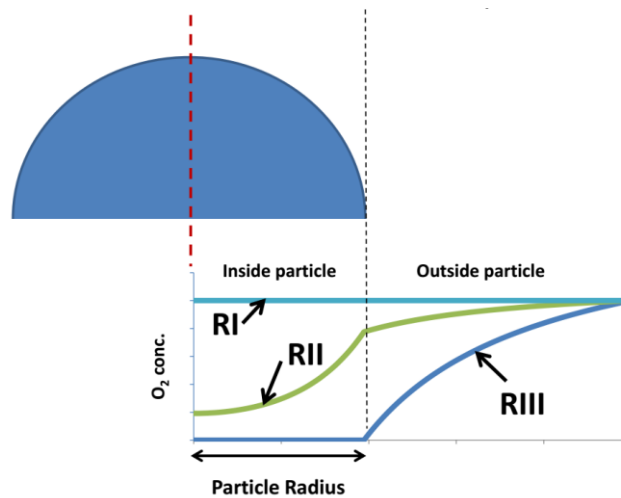
Figure 4.4. *Oxygen concentration inside and outside a solid fuel particle in different regimes [55].*

Due to the high amount of volatiles biomass char has generally notably lower density than that of coal which influences the rate of combustion [4]. Reactivity of biomass chars after rapid devolatilization is noted to be much higher than the ones produced by milder conditions. Furthermore, higher temperature level produces more reactive char. Pyrolysis in high temperature and high heating rate produces open structures in the particle and thus enhances the oxygen diffusion inside the particle. [56] Chars produced by rapid pyrolysis are much more porous and less dense than those produced by slow pyrolysis. The apparent density of char particles from slow pyrolysis could be three times as high as the ones from rapid pyrolysis. [53]

Particle size affects the char yield proportionally i.e. increase in particle size increases the char yield. Increasing the particle size from 0.5 - 0.7 mm to 0.7 - 1 mm increases the char yield approx. 20 % in 800 ºC. Thus, smaller particle size is noted to increase the char reactivity due to higher heating rate. [53] Chars of raw biomass have also been observed to be much more reactive than those of torrefied biomass. Combustion of tor-refied palm kernel sheet char in 9% oxygen gives almost the same conversion as the char from raw material in 4 % oxygen with the same residence time [57].

In combustion processes char is eventually oxidized to carbon dioxide. However, inside the flame of an industrial burner there is typically very little oxygen present due to burn-ing of the volatile compound around the particle. Thus, there is a limited supply of oxy-gen present in the boundary layer where char oxidation takes place which favors for-mation of CO. According to measurements CO_2/CO ratio has a strong temperature de-pendency as well. Higher temperature seems to favor production of CO at the expense of CO_2. CO_2/CO production rate has a significant effect on the particle temperature and thus, on reaction rate due to substantially higher reaction enthalpy (see equations *R1* and *R2*). [58] The temperature dependency of production ratio of CO_2/CO is presented in Figure 4.4.
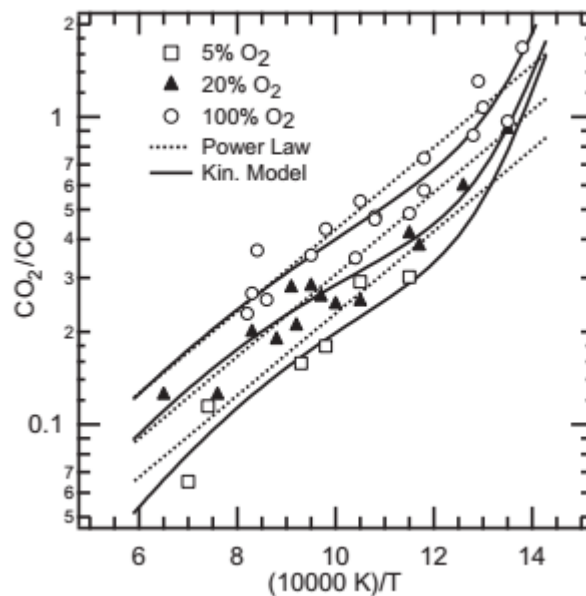
Figure 4.5. *Experimental data of CO_2/CO production ratio with predictions of models [58].*

Char oxidation is typically relatively slow process compared to devolatilization. Even though during devolatilization 85 - 95 m-% could be released from the biomass particle in combustion processes, the largest part of the history of biomass combustion involves char oxidation. [4]

5. MODELING OF SOLID FUEL COMBUSTION

Great potential of using computational fluid dynamics (CFD) in designing of different energy producing solutions has been realized widely. Power station boilers and furnaces have been the largest industrial applications of the CFD models. [59] CFD could be used in designing completely new processes and furnaces or adapting the old ones for new fuels, e.g. biomass. The modeling results of predicting and improving boiler efficiency have been promising and CFD modeling has established itself as an important tool for the development of technologies. Several commercial CFD codes are available for simulating pulverized coal boilers. [29, 59, 60] The commercial CFD-code Ansys Fluent is nowadays widely used in simulation of different flow and combustion cases. TUT has a license for Fluent which has many combustion sub-models already programmed, and therefore using these tools would be straightforward and cost-efficient. However, Fluent uses many simplifications in modeling solid fuel combustion which is originally developed for pulverized coal combustion. The most significant scope of this thesis was to determine how the solid fuel combustion model of Fluent is able to perform the simulation of biomass combustion which differs quite a lot from that of pulverized coal firing.

The rate of solid fuel combustion depends on chemical, structural and physical properties of the fuel. Heat and mass transfer as well as chemical kinetics are essentially affecting the combustion. [26] In a case of small particle size internal temperature gradients of the particle are small enough to be neglected which is often the case for the pulverized coal particles. On the other hand, biomass particles are often larger, and therefore develop relatively large internal temperature gradients inside the particle. The temperature difference between the particle surface and center could be several hundreds of degrees which affects strongly to proceeding of the combustion phases inside the particle as mentioned in the previous chapter.

The ratio of internal conduction resistance to external heat transfer resistance is called Biot number Bi. It describes the importance of internal heat transfer to external heat transfer, and thus small Biot number leads to small internal heat transfer. The particle Biot number is presented in Equation 1. For plates, cylinders and spheres $Bi < 0.1$ ensures that the temperature at the center of the solid does not differ more than 5 % from the temperature at the particle surface. [61]

$$Bi = \frac{\bar{h}L}{k_s} \qquad\qquad (1)$$

In Equation 1 the term $\bar{h}$ represents the average heat transfer coefficient, k_s is the heat conductivity of the particle and L is some appropriate characteristic length of the solid body, e.g. the radius of a sphere. [61] Particles can generally be divided into two categories by their Biot number: thermally thin and thermally thick ones. Traditionally Biot number >1 has been used for the limit for thermally thick particles. Calculations show that limiting size for thermally thin biomass particles is about 250 µm. The transition from thermally thin to thermally thick particles takes place in a pulverized fuel furnace for spherical particles with diameter 200 - 250 µm and for cylindrical particles with diameter 150 - 200 µm. This depends highly on the exact heat transfer conditions and fuel properties. [44] Generally biomass particles are larger than 250 µm, and thus the assumption of thermally thin particles may not be realistic [19].

The energy balance for a solid fuel particle is presented in Equation 2. The term on the left side represents the thermal energy stored to the particle. The first term on the right side represents the convective heat transfer between the particle and surrounding gas. The second term represents the radiative heat transfer and the last term on the right side represents the heat released or bound through the chemical reaction of the particle. [62]

$$m_p c_p \frac{dT_p}{dt} = hA_p(T_\infty - T_p) + \varepsilon_p A_p(\theta_R^4 - T_p^4) - h_{react} \frac{dm}{dt} \tag{2}$$

In Equation 2 the term m_p is particle mass, c_p specific heat, T_p particle temperature, t time, h convective heat transfer coefficient, A_p particle surface area, T_∞ temperature of surrounding fluid, ε_p emissivity of the particle, θ_R radiative temperature of surrounding and h_{react} heat released in a chemical reaction. The convective heat transfer coefficient can be determined from Ranz-Marshall correlation for Nusselt number Nu which is presented in Equation 3. [62]

$$Nu = \frac{hd_p}{k_\infty} = 2.0 + 0.6Re_d^{0.5} Pr^{0.33} \tag{3}$$

In Equation 3 the term d_p represents the particle diameter, k_∞ heat conductivity of the surrounding fluid, Re_d particle Reynolds number and Pr Prandtl number of the surrounding fluid. [62] The particle Reynolds number can be received from the equation

$$Re_d = \frac{\rho_p d_p \Delta u}{\mu}, \tag{4}$$

where the term ρ_p is particle density, d_p particle diameter, μ molecular viscosity of the fluid, and Δu slip velocity between the particle and the fluid phase. [62]

Fluent uses an assumption of consecutive combustion phases which cannot overlap and must proceed one after another. The first phase of particle combustion is the inert heating phase in which the particle literally heats without any reactions until the user defined vaporization temperature is reached. When the particle temperature reaches the

vaporization temperature the devolatilization model becomes active. However, the vaporization temperature has no physical significance and is just a modeling parameter. Devolatilization model is active while the particle temperature is above vaporization temperature until the particle mass exceeds the mass of the non-volatiles in the particle. After the volatile content of the particle is completely evolved, the particle surface combustion model starts. It stays active until the combustible fraction is consumed. The remaining ash experience inert heating or cooling. [62]

Different models are developed to describe the conversion rate, especially that of pyrolysis. They are not necessarily able to describe the physical and chemical phenomena correctly but only correlate the experimental data. [3] Reaction rate coefficients (k) are highly dependent on temperature and this temperature dependence could be described with Arrhenius equation which is presented in Equation 5 [63]. It is the most commonly used equation for reaction rate of solid fuel oxidation for its simplicity [26].

$$k = Ae^{-\frac{E}{RT}} \tag{5}$$

The term A is called activation energy and E frequency factor in Equation 5. In the equation the term R is gas constant and T is temperature. In theory activation energy describes the energy barrier required to overcome for the reaction to proceed. Frequency factor on the other hand describes the maximum speed of the reaction. [63]

Most of the particle combustion models in CFD software solutions are developed for pulverized coal combustion. For the pulverized coal combustion assumptions of isothermal particles and consecutive combustion phases may be valid due to small particle size [64]. However, biomass combustion differs from that of coal by many ways as mentioned in the previous chapter. More sophisticated models are also developed to take into account the overlapping combustion phases, e.g. the layer model which takes radial intra-particle species and temperature gradients into account. In the layer model the particle is discretized into layers and the model allows parallel progress of the thermal conversion sub-processes by assuming that the processes move towards to the particle center. Devolatilization moves towards to the particle center while the particle surface begins to oxide. These kinds of models do not exist as original models in commercial CFD software solutions and they have to be created as in-house codes. [65]

The main goal of this thesis was to discover how well the biomass particle combustion can be modeled with the existing tools of the commercial CFD software Ansys Fluent. In the next sub-chapters devolatilization and char oxidation modeling used in this thesis are described more detailed. In the third sub-chapter the modeling assumptions and conditions are explained.

5.1   Devolatilization modeling

Knowledge of the kinetics of pyrolysis is essential in order to optimize the process pa-
rameters. The simplest way to model the pyrolysis is to use constant rate devolatiliza-
tion which assumes that the volatiles are released with constant rate during the whole
pyrolysis process [62]. The model is however incapable of describing the temperature
relation of pyrolysis, and therefore a common model for devolatilization is the one stage
global single reaction model [26]. It assumes that the whole devolatilization process
could be described with a single Arrhenius type equation. The single kinetic rate model
is expressed in Equation 6:

$$-\frac{dm_p}{dt} = k\big(m_p - \big(1 - f_{v,0}\big)\big(1 - f_{w,0}\big)m_{p,0}\big),\tag{6}$$

where m_p is the particle mass (kg), $f_{v,0}$ mass fraction of volatiles initially present in the
particle, $f_{w,0}$ initial mass fraction of water in the particle, $m_{p,0}$ the particle initial mass
(kg) and k kinetic rate, which can be determined with Equation 5. [62]

The terms activation energy and frequency factor are used for a single substance or re-
action. Thus, using those terms could be appropriate because single rate reaction of py-
rolysis is modeling large amount of reactions together. Pre-exponential and exponential
factor should be more suitable in this situation, but however the term activation energy
is commonly used in describing pyrolysis. [49]

Models based on single rate reaction (see Equation 6) have asymptotic yields of volatile
matter. In high temperature levels significant differences in pyrolysis yields may occur
as mentioned in the previous chapter. The temperature dependency of pyrolysis can be
taken into account by many ways. However, simple models with minimum number of
parameters are preferred due to increasing required calculation capacity with increasing
complexity of the models. Complex models may also have several parameters and reac-
tions to describe the devolatilization process and determining all of these is impractical
and time consuming. Final yields predicting models should contain certain competing
mechanisms in order to be relatively simple but still accurate. The model of two com-
peting reactions was presented by Kobayashi in 1970's. [66] Kobayashi two-competing
rates model is also adapted to Fluent and it is described in Equation 7 [62].

$$\frac{m_v(t)}{(1-f_{w,0})m_{p,0}-m_a} = \int_0^t (\alpha_1 R_1 + \alpha_2 R_2) exp(-\int_0^t (R_1 + R_2)dt)dt \tag{7}$$

In Equation 7 the term on the left represents the conversion rate of dry ash free basis
(X_{daf}) in which $m_v(t)$ is the volatile yield up to time t and m_a is the mass of ash in the
particle. R_1 and R_2 on the left represent the kinetic rates of pyrolysis in high and low
temperatures, respectively. They can be determined with Equation 5. [62] α_1 and α_2 are

the yield factors, and they represent mass stoichiometric coefficients of fast and slow pyrolysis, respectively. [66]

The two-competing rates devolatilization model assumes that there are two alternative pyrolysis reactions which are competing from the same solid compound. The first one is slow pyrolysis occurring in relatively low temperatures and being slow, i.e. the pre-exponential factor and activation energy are low. The second reaction takes place at high temperatures and it is very fast, i.e. pre-exponential factor and activation energy are high. Thus, in low temperatures only the first reaction is active which reduces the model to the single rate reaction model. The yield factor α_1 for the first reaction repre-sents the asymptotic volatile yield in low temperature levels. However, due to high pre-exponential factor and activation energy the second reaction becomes dominant at high temperatures resulting in higher volatile yields. The volatile yield in specific conditions is determined through the integrated effect of these two reactions. [66] In Figure 5.1 both the single rate reaction and two-competing reactions models are presented. For the competing reactions in the figure k_1 and k_2 correspond to R_1 and R_2 in Equation 7.

Figure 5.1. Basic principle of single reaction and two-competing reactions models [66].

It should be noted that two-competing rates model serves as a tool for correlating exper-imental data. Thus, the parameters for reactions do not have much physical significance. This model has been used successfully in modeling pyrolysis of coal. [66] Biomass has high amount of volatiles, more than 80 m-% of dry-ash free basis, and therefore model-ing the devolatilization has a dominating role in the overall conversion process [64]. Thus, the use of Kobayashi devolatilization model could be efficient for biomass pyrol-ysis. There exist also more advanced models for devolatilization, e.g. chemical percola-tion devolatilization model in Fluent, but they require more detailed knowledge of ref-erence components of the biomass of interest. [62] Typically, the proximate and ulti-mate analyses are the only available tools for fuel characterization, and therefore knowledge of the reference components is not available.

The particle diameter evolution during the pyrolysis stage can be determined with Equation 8 which is used by Fluent. The particle diameter is assumed to depend linearly on the conversion during the pyrolysis. Swelling factor describes how large the particle diameter is at the end of the pyrolysis compared to the initial diameter. Therefore, the swelling factor of 1 means that the particle diameter remains constant and the value 2 for swelling factor leads to doubling of the diameter when all the volatiles have been released. [62]

$$\frac{d_p}{d_{p,0}} = 1 + (C_{sw} - 1)\frac{(1-f_{w,0})m_{p,0}-m_p}{f_{v,0}(1-f_{w,0})m_{p,0}} \tag{8}$$

The assumption of the linear change of diameter in respect of conversion is rather coarse and more sophisticated models are used in literature to describe the particle evolution during the combustion [12]. Especially the models being able to describe the periodic swelling during the pyrolysis could be useful. The particle swelling phenomena and bubble formation inside the particle may cause an enlargement of the particle but at high temperatures the final sizes of biomass particles are noted to decrease slightly. Even though the biomass particles are generally highly elongated, the char particles are assumed to have more spherical shapes after pyrolysis. [56]

Reactivity parameters for pyrolysis presented in literature may vary greatly even though they could be determined for the exactly same fuel. This can be explained by exponential relationship of the parameters in Equation 5 and if the different parameters were drawn in the same picture in which the axes were pre-exponential factor and activation energy, they would form almost straight line. [47] Thus, high activation energy correlates with high pre-exponential factor and the conversion curves with the different sets of reactivity parameters are very similar.

5.2   Char oxidation modeling

Char oxidation is controlled by both chemical kinetics and oxygen diffusion to the particle surface [68]. Therefore, it is essential to be able to predict the effect of both processes on reaction rate. Equation 9 represents the external diffusion rate coefficient D_0 and Equation 10 describes the chemical kinetics rate R of char oxidation which is the modeled with the Arrhenius equation. Their joint effect on char oxidation conversion can be modeled with Equation 11. [62]

$$D_0 = C_1 \frac{\left(\frac{T_p+T_\infty}{2}\right)^{0.75}}{d_p} \tag{9}$$

$$R = C_2 e^{-\left(\frac{E_r}{RT_p}\right)} \tag{10}$$

$$\frac{dm_p}{dt} = -A_p p_{ox} \frac{D_0 R}{D_0 + R} \tag{11}$$

In Equations 9 and 10 the term C_1 represents diffusion constant, C_2 pre-exponential factor and E_r activation energy of char oxidation. In Equation 11 p_{ox} represents the partial pressure of the oxidizer. [62] The value for diffusion constant $C_1 = 5e^{-12}s/K^{0.75}$ may be obtained from literature [68]. This value is the default value of Fluent for char oxidation as well.

The particle diameter evolution during char oxidation could be modeled with the shrinking particle model in which the particle density is assumed to remain constant while the particle diameter decreases (regime 3 in the chapter 4.2). It represents the combustion and gasification of the large particle well if the temperature is high and the particle porosity is small. [26] However, biomass char is highly porous, and therefore using the shrinking particle model could be misleading. Another option is to use constant particle diameter during the char oxidation while the particle density decreases. This type of approach is used by e.g. Fluent. [62] The char particles can be modeled as spheres due to the fact that after pyrolysis even the most elongated particles are nearly spherical [56].

5.3   The model of combustion process in drop tube reactor

The reactivity parameters for the specific biomass fuels were obtained in this thesis from experimental data by using a Matlab based model that uses the same procedure in modelling particle combustion as the commercial CFD code Ansys Fluent does. Thus, the reactivity parameters should be valid for both the fuel and model. However, Discrete Phase Model (DPM) of Fluent uses several simplifications in modeling the solid fuel combustion. First of all, Fluent uses an assumption of thermally thin particles in simulations meaning that the particles are modeled as isothermal and the internal temperature gradient of the particle is not taken into account. The particle geometry is not taken into account in heat transfer of DPM and particles are modeled as spheres. [62] This could be a poor choice in modeling most biomass fuels and may lead to substantial error in predicting biomass combustion process [43]. Another major simplification of DPM is that it assumes the sub-processes of combustion, i.e. devolatilization and char oxidation, to proceed as one after another [62].

The combustion process in the DTR was modeled with the model programmed in Matlab. The particle falling velocity was used in determining the residence time of the particle in the reactor and particle slip velocity was used in calculating the convective heat transfer from Equation 3. The particle temperature could be solved from the particle energy equation (Equation 2). However, Fluent uses its own approximate solution for discretizing the energy equation using an assumption of small temperature differ-

ence between time steps due to the small time step size. The particle temperature can be solved from Equation 12:

$$T_p(i) = \alpha_p + \left(T_p(i-1) - \alpha_p\right)e^{-\beta_p \Delta t} \tag{12}$$

where

$$\alpha_p = \frac{hA_pT_\infty + \frac{dm_p}{dt}h_{fg} + A_p\varepsilon_p\sigma\theta_R^4}{hA_p + \varepsilon_pA_p\sigma T_p^3(i-1)} \tag{13}$$

and

$$\beta_p = \frac{A_p\left(h + \varepsilon_p\sigma T_p^3(i-1)\right)}{m_pc_p}. \tag{14}$$

In Equations 12 - 14 the term i is the index of a time step and Δt represents the size of the time step. α_p or β_p do not have any physical importance and they are only simplifying the equation 12. [62] The approximate solution of energy equation is introduced in Ansys Fluent Theory Guide 15.0 [62] only in touch with inert heating and devolatilization, but in this thesis it is assumed to represent the heat transfer for char oxidation as well.

Equations 12 - 14 were used in determining the particle temperature in preheating, pyrolysis and char oxidation. A major simplification was made by assuming the pyrolysis and char oxidation processes being sequential, occurring one after another. However, this assumption made the modeling of the reactions relatively simple due to the fact that only one reaction may be active at a time. The devolatilization law of Fluent is active when the particle temperature reaches the devolatilization vaporization temperature and remains in effect until the mass of the particle falls below the mass of the non-volatiles in the particle. [62] The vaporization temperature was set to 400 K in modeling. Equations for pyrolysis were discretized as follows:

Single rate pyrolysis model

$$k(i) = A\,exp\left(-\frac{E}{R_uT_p(i-1)}\right) \tag{15}$$

$$m_p(i) = m_p(i-1) + k(i)\left(m_p(i-1) - \left(1 - f_{v,0}\right)m_{p,0}\right)\Delta t \tag{16}$$

Kobayashi pyrolysis model

$$R_1(i) = A_1\,exp\left(-\frac{E_1}{R_uT_p(i-1)}\right) \tag{17}$$

$$R_2(i) = A_2\,exp\left(-\frac{E_2}{R_uT_p(i-1)}\right) \tag{18}$$

$$\sigma(i) = \sigma(i-1) + \big(R_1(i) + R_2(i)\big)\Delta t \qquad (19)$$

$$X_{daf,pyr}(i) = X_{daf,pyr}(i-1) + \ldots$$

$$\Big(\big(\alpha_1 R_1(i) + \alpha_2 R_2(i)\big) exp\big(-\sigma(i)\big)\Big)\Delta t, \qquad (20)$$

where $X_{daf,pyr}$ in Equation 20 represents the dry-ash-free conversion rate of pyrolysis. The two-competing rates Kobayashi model (Equation 7) is discretized in a way that integrals are replaced with cumulative sums i.e. the value of ith time step is summed to the value of previous time step (Equations 17 - 20). In each equation of reaction rate the particle temperature of the previous time step (*i-1*) is used. As mentioned before, if the simulation time was low the error caused by this method would be low as well.

Fluent requires the volatile yield determined beforehand and it cannot be exceeded [62]. However, it disables the biggest advantage of the Kobayashi pyrolysis model that the pyrolysis yield could be temperature dependent. Due to the connection of the combustion sub-models Fluent uses several switching limits to ensure finishing of reactions in all conditions. This had to be solved by an expert of Ansys product support because Ansys Fluent Theory guide did not have any mentions of closing or switching conditions of the sub-models. The expert from the Ansys product support had to dig very deep into the source code of Fluent in order to solve the hardcoded limiting values and there were not many people able to perform such actions. Therefore, the solving process of the Ansys product support took considerable amount of time, usually several weeks at a time.

First of all, Fluent uses one percent limiting value for volatiles as a switching condition from pyrolysis to char oxidation, i.e. if 99 % of the volatile matter was released all the volatiles left in the particle are released at the next time step. This boundary value is presented in Equation 21 and it prevents the conversion of pyrolysis to asymptotically approach the beforehand determined volatile matter $f_{v,0}$ by starting char oxidation sooner. Thus, this limiting value creates a step in a conversion curve before switching the char oxidation active.

$$m_p(i) < m_{p0} - 0.99 \cdot f_{v,0} \cdot m_{p0} \qquad (21)$$

This is an effective switching condition for the single kinetic rate model to prevent a lag before char oxidation but however, it is not enough for Kobayashi model. For two-competing rate model another limiting condition was used as well. It can be seen in Equations 7 and 20 that if the exponential term was very small the pyrolysis rate would be low as well, thus effectively stopping the devolatilization reaction. The switching limit for devolatilization in Fluent is that when the exponential term in Equation 20 is smaller than 0.1 all the remaining volatiles are released at the same time step. The term is decreasing due to negative integral term in the exponent, and therefore Fluent inter-

rupts the devolatilization model if the sum in discretized form is big enough (Equations 19 - 20). The limiting value of Kobayashi pyrolysis model is presented in Equation 22. The integral part of the equation is replaced with the sum expression as it has been done in Equation 20. However, this has no physical significance and is just a tool to finish pyrolysis in all conditions.

$$ex\,p\left(-\sigma(i-1) - \left(R_1(i) + R_2(i)\right)\right) < 0.1 \tag{22}$$

The char oxidation process was discretized by following equations:

$$D_0(i) = C_1 \frac{\left(\frac{\left(T_p(i-1) + T_\infty(i)\right)}{2}\right)^{0.75}}{d_p(i)} \tag{23}$$

$$R(i) = C_2\,exp\left(-\frac{E_r}{R_u T_p(i-1)}\right) \tag{24}$$

$$m_p(i) = m_p(i-1) - A_p p_{ox} \frac{D_0(i)R(i)}{D_0(i) + R(i)} \tag{25}$$

Once again the particle temperature at ith time step is replaced with the value of the previous time step. In this thesis all the char was expected to form carbon monoxide in its oxidation due to the high temperature in the reactor which favors the formation of carbon monoxide against carbon dioxide as mentioned in the fourth chapter.

The particle combustion model based on equations 12 - 25 represent the mass loss behavior of only one particle size. The code for the particle combustion model is presented in Appendix A. However, even if the fuel batch used in experiments was sieved extremely carefully it never would have contained only one particle size but some size distribution. Thus, the size distribution of the imaged particles was discretized into ten equally sized fractions and the mass mean diameter was calculated for each fractions. Then the model was run for each mass mean diameters consecutively and the ten model outputs were averaged in order to get the average conversion curve. In Equations 12 - 25 the term i represents a time step number, i.e. the current simulation time. However, in the modeling a place step was used instead of time step because it was considered easier to use. The time step was obtained by dividing the current place step with the particle velocity at that distance.

Optimization of the reactivity parameters was conducted by minimizing the least square error of the model output and the experimental data. The used optimizing tool was fminsearch function of Matlab which is very effective tool for finding local minimums. However, in the space of six independent variables with Kobayashi pyrolysis model the minimizing procedure was more challenging due to a large amount of local minimums. The function fminsearch found effectively a local minimum but after a new minimizing loop found another one. Thus, the minimizing had to be constructed in a loop structure

in which the results of the previous minimization were used as the initial values for the next optimization. However, not even this procedure was enough, and therefore the initial values had to be changed occasionally in order to prevent the optimization getting stuck on local minimums. This was conducted by changing the value of the swelling factor to 1 at every fourth loop and then returning the value back to the value which it used to be. The optimization code is shown in Appendix B.

Optimization routine for Kobayashi parameters had to be controlled due to a large number of optimizable variables. In the space of six independent variables it is possible to find numerous of minimums which however lead to unrealistic reactivity parameters. Therefore, the optimizable variables had to be limited, so that e.g. yield factors in Equation 7 had to be smaller than one and bigger than some boundary value decided by eye. This is highly unscientific approach which, however was needed to obtain realistic results. Optimization routine for the single rate devolatilization model and char oxidation model was much more straightforward due to decreased number of optimizable variables. However, the minimization was still constructed in a loop in order to speed up the minimization routine.

6. TEST EQUIPMENT

The test equipment of this thesis included fuel handling equipment which was used to reduce the particle size of the pelletized fuel, imaging setup used in determining the particle dimensions and the main study instrument, drop tube reactor. The main test equipment is introduced more accurately in this chapter. Also the drop tube reactor with its sub-systems is represented more closely at the end of this chapter.

6.1 Fuel handling

The fuel samples were dried for at least 24 hours in 105 $^{\circ}$C temperature to remove moisture from the fuel and prevent any biological degradation of the sample. After this, the pelletized fuel was milled with Retsch Ultra-centrifugal mill ZM 200 which is presented in Figure 6.1. The centrifugal mill of Tampere University of Technology (TUT), referred as the Retsch mill, is based on both impact and shearing action. First the particle has an impact with a wedge-shaped blade and then it is sheared between the blade and a ring sieve.

Figure 6.1. The Retsch mill ZM 200 used by TUT [69].

The grinding was conducted with the ring sieve with an opening of 750 μm and a rotor blade comprising of eight wedge-shaped blades. The minimum radial velocity of 6000 rpm was used in the tests. Ground fuels were then sieved with the Retsch vibrational sieve. Multiple different sizes of sieves were available for the vibrating sieve of TUT.

6.2 Imaging setup

The next step was to analyze the particle shapes and determine the size distribution of the sieved fractions, which was conducted by imaging the particles. First off the particles were scattered on a light diffuser plate illuminated from below with several led-lights. The particle imaging setup is presented in Figure 6.2. The particles were dropped on the plate in a way that they were mostly separated. The particle projections were then pictured with a CCD high speed camera AVT Marlin 145-B2 with a 1380 x 1090 resolution and with a black and white CCD-cell. The images were analyzed with the computer software developed by D.Sc. Markus Honkanen in TUT which based on his dissertation [70]. The program identified the outlines of separate and staggered particles, created an ellipse fit for them and tabulated the results in a xls file. The dimensions of the ellipse could be used to describe the shape and sphericity of the particles.
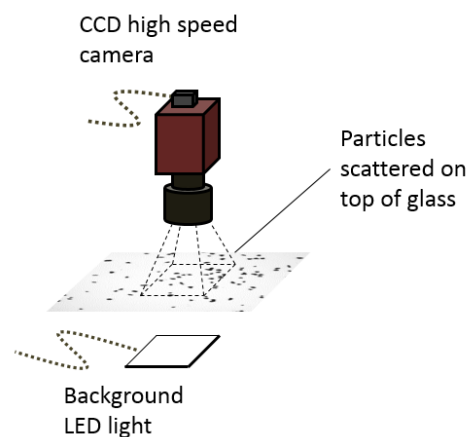
Figure 6.2. The basic principle of imaging setup [12].

Another program developed by D.Sc. Henrik Tolvanen as a part of his dissertation was used to determine sphere-equivalent diameters of the imaged particles [71]. The program analyzes the results of ellipse dimensions of the first mentioned program. The maximum and minimum ellipse diameter ratio is called an aspect ratio and it was used to separate close to spherical from elongated particles. The aspect ratio threshold was set to value of 1.5 meaning that particles which had the aspect ratio below 1.5 were considered as spheres and their diameter was calculated as an average of the maximum and minimum ellipse diameters. Particles having the aspect ratio equal or over 1.5 were considered as cylinders. The cylinder thickness was calculated by dividing the projection area with the maximum ellipse diameter. The ellipse fit seemed to exaggerate the minimum diameter of highly elongated particles and thus, this procedure was needed to obtain the thickness of cylinder. Sphere-equivalent diameters of the particles were calculated as diameters of the spheres with the equal volume to the cylinder volume.

The sphere-equivalent diameters were greater than the nominal ones of the sieves due to the fact that cylindrical particles may have penetrated the sieve upright, and therefore

particles were classified by their smallest dimensions [45]. Particles were pictured both before feeding them into the reactor and after the heat treatment in order to determine the particle size evolution needed for the modeling of the combustion process. The software used to determine sphere-equivalent diameters of the particles also formed a size distribution of imaged particles and discretized it. The discretization was conducted by dividing the entire size distribution into 10 equal-sized fractions and calculating the mass mean diameter for all of them. The discretized size distribution was essential in order to model the combustion process because the conversion curves of all ten fractions were modeled as mentioned in the previous chapter.

6.3   Drop tube reactor

A drop tube furnace is the most common version of the entrained flow reactor type in combustion experiments. In the drop tube furnace, the solid fuel particles are injected along the axis of the heated reactor tube into the flowing preheated gas stream. The particle residence time in the reactor can be adjusted by changing the positions of water cooled injector and the collector, and the gas velocity. Drop tube furnaces may be designed for complete collection of char, tar and volatiles. Particle weight loss from one drop height can be determined by ash tracer or gravimetrically by comparing the total fuel fed with the residue collected. Drop tube furnaces have number of advantages such as high heating rate (~10^4 K/s) and high temperature levels up to 1900 K. The furnace can also handle most of the particle sizes and shapes, and the particle residence time can be controlled reasonably well. In addition, the particle velocities can be accurately measured and calculated. A major disadvantage has been determining the particle temperature in the reactor during the pyrolysis. In the most experiments the particle temperature has been modeled. However, the optical windows could be used in determining particle temperatures and velocities. Another disadvantage of the method has been that the volatiles remain hot in gaseous phase during the experiment which enables secondary reactions to occur. In many cases also the particle heat capacity and emissivity have been assumed in the temperature calculations. [54]

Combustion experiments were conducted with a drop tube reactor (DTR) in the laboratory of Tampere University of Technology. The DTR consists of a heated tube, water cooled injector, and particle feeder and collector. The basic principle of the DTR is presented in Figure 6.3. The reactor tube is made of stainless steel with an inner diameter of 26.7 mm and with temperature resistance up to 1300 ºC. The reactor tube is heated with eight separately adjustable heating elements comprising 2-7 Ω/m resistance wire sets. The heating elements are insulated with 7 cm thick layer of kaowool. The temperature profile of the reactor wall is measured with eight thermocouples and the wall temperature profile can be tuned by changing the voltages of different heating elements which all are heating some specific zone of the reactor. The length of the heated reactor pipe is 65 cm which is followed by 2.5 cm long unheated zone. There is an optical win-

dow in the reactor wall for measurements of particle falling velocity and temperature. It consists of horizontal pipe attached to the reactor tube and the distance of the window center point is 53.5 cm from the start of the heating zone.
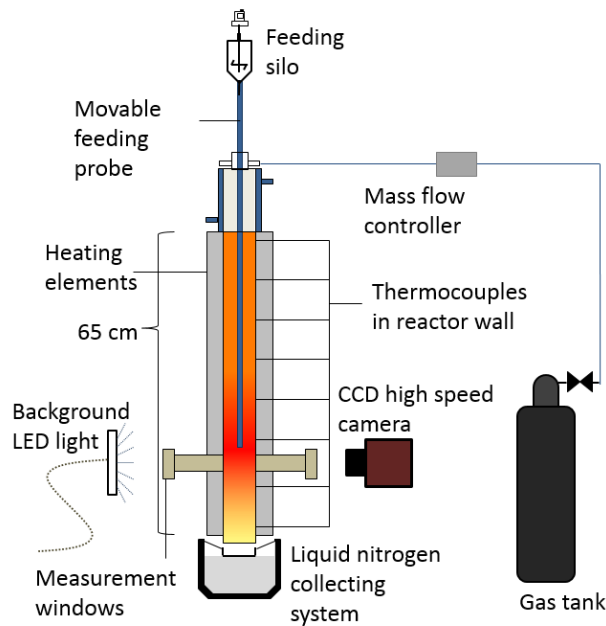

Figure 6.3. *Principle of drop tube reactor used for experiments [12].*

Particles are fed into the reactor with a feeding silo which consists of a container and a screw feeder in the bottom of the silo. Several different screw feeders were available and the best one for injecting the specific fuel as single particles was validated before the experiments by imaging the particles dropping inside the reactor. One experiment with the reactor lasted approx. 10 minutes while the amount of the fuel injected into the reactor was approx. 0.03 g. This amount of fuel was found to be enough to determine the mass loss accurately enough but still keeping the fuel stream in the reactor so low that it did not affect the gas velocity and temperature profiles or the gas composition in the reactor. The screw was rotated by an electric motor above the reactor and the motor running direction could be changed. The particle feeding system was also equipped with a vibrating device in order to prevent the particles getting stuck on the walls of the silo and help feeding single particles into the reactor. However, only the smallest particles could be fed into the reactor with the feeding silo. A feeding hose was used and the feeding process was completely manual when the bigger particles were injected into the DTR.

Particles were collected in the collecting vessel below the reactor floating in the liquid nitrogen. The boiling point of nitrogen is 77.4 K (-195.75 ºC) which ensured stopping of the reactions immediately after particles left the reactor [72]. During the experiments the container filled with liquid nitrogen was attached to the bottom of the reactor and it was filled between the experiments. In order to prevent melting of the container a water-

cooled collar was placed between the hot reactor bottom and the nitrogen container. Both the feeding silo and the particle collecting vessel were weighed with a scale before and after the experiments. The particle collection vessel was weighed also next day to ensure that the moisture condensed on the cool vessel had evaporated. Precision of the scale was four decimals and if the weight was less than 100 g the accuracy was 0.0001 g. With a weight more than 100 g the accuracy was 0.0005 g.

The mass flow controller was used to adjust the gas mass flow to the reactor. There were separate mass flow controllers for both nitrogen and oxygen. The gas heat expansion was taken into account in order to achieve the same final velocity profiles with different reactor temperatures. When temperature was 600 ^{o}C the mass flow controller was 100 % open for nitrogen representing 0.002 Nm^3/min flow rate which corresponds to 3.8937E^{-5} kg/s mass flow rate. For the 900 ^{o}C temperature level the nitrogen mass flow controller was 75.9 % open corresponding 2.9582E^{-5} kg/s mass flow. [61] With these mass flows the fuel stream in the reactor was around 1 m-‰ of the gas mass flow. Thus, the effect of the particles interacting the gas stream could be assumed to be negligible. Before entering the reactor gas went through a laminarization cell which consists of adjacent tubes inside the reactor. The laminarization cell was used to remove turbulence from the gas flow which could be caused by the gas entering vertically into the upper part of the reactor.

In determining the gas temperature profile thermocouple measurements were used. A thermocouple was injected into the reactor from the particle feeding probe when the reactor was heated to the target temperature. Temperatures were measured with the thermocouple at the reactor centerline from the end of the injector to the end of the reactor which covered the whole distance that particles traveled inside the reactor. The thermocouple was moved 1 - 4 cm at a time and the temperature was let to stabilize. However, the thermocouple did not have radiation shield, and therefore the wall temperature affected significantly to thermocouple measurements due to thermal radiation.

The same CCD high speed camera introduced in touch with the particle imaging setup in the previous sub-chapter was used taking pictures from the optical window while the particles were falling in the reactor. Camera was placed in front of the optical window and a background led-light was located on the opposite side of the reactor. The led-light was pulsating with the frequency of 700 Hz. The camera took pictures of the particle shadows at consecutive led-light pulses. Thus, pictures of particles were doubled which is illustrated in Figure 6.4. Particle velocity could be determined by measuring the distance of two particle shadows because the interval of the two light pulses was known (1/700 s). The pixel based scale of the camera was determined before the experiments. The pictures of the particles fed into the reactor were analyzed with a computer software programmed by M.Sc. Antti Aho as his bachelor thesis work [73]. The software identified particles, linked the shadows of the same particle together and calculated the falling velocity of the particles. Due to a large amount of pictures of the particles the falling

velocity was quite accurately determined. The particle velocity determining software gathered velocities of the different particles and also the particle sizes into the same table.

Figure 6.4. Double exposed picture of particles falling in the reactor.

From the optical window the two-color pyrometer could have been used to obtain the particle surface temperatures in the reactor. However, the particle temperature had to be notably higher than the surrounding gas temperature and therefore, only the char oxidation temperatures could have been achieved with the pyrometer. Thus, the temperature measurements would have affected only to char oxidation results. In the previous experiments with the DTR particle surface temperatures were relatively close to those which were modeled [74]. The particle temperature measurements would not have provided any additional value for the thesis, and thus they were left out.

7. EXPERIMENTS

The experimental part of this thesis work was divided into two different categories: Fuel pre-handling and the main experiments in the drop tube reactor. The experimental part was originally planned to contain the fuel milling, determination of the particle shapes and sizes, and the combustion experiments with drop tube reactor. However, Valmet Oy was developing a mill used in biomass grinding in the boiler applications with their industrial partner. Determination of characteristics of the pulverized biomass of the mill was essential in order to improve the mill efficiency and to obtain more appropriate particle size. Thus, the analysis of the grinding results of the mill used by Valmet, and the comparison between the grinding results of the mill used by Valmet and the Retsch Mill used by Tampere University of Technology are presented in the first sub-chapter.

The pre-ground biomass was chosen for the experiments and the characteristics of two biomasses are represented in the second sub-chapter. The second part of the thesis consisted the experiments with DTR. The profiles of the wall and gas temperatures in the DTR were fitted and partly modeled, and they are presented in the third sub-chapter. Finally, in the fourth sub-chapter the pyrolysis experiments in pure nitrogen and the combustion tests in the mixture of nitrogen and oxygen are presented.

7.1   Comparison between the milling techniques

Valmet Oy provided the pellet samples for the study. They provided both pellets and already ground fuel for the experiments. The pre-ground pellets were processed with the mill Valmet is using its solutions. The reason for both forms of the fuels was to examine the effect of the grinding technique on particle sizes and shapes. A great interest of Valmet was to compare their milling technique against the mill used by TUT and to see how it affects particle sizes and shapes, and therefore even particle reactivity. This is a reason why they delivered fuels in two forms. The objective was to receive rough shape information of the fuel, and therefore both the already milled fuel and the pellets milled in TUT were divided into two size groups: under and over sieving size of 500 μm. The proportions of the size under 500 μm were 78.8 m-% and 75.3 m-% for the Valmet and Retsch mill, respectively. Thus, there was no remarkable difference between the grinding techniques in this rough size distribution. Determining the differences between the milling techniques required closer analysis and the imaging setup was used in order to examine the grinding results more detailed.

The first set of particles scattered on the light diffuser plate were the ones with the sieving size of less than 500 μm. Figure 7.1 shows the cumulative sums of number and vol-

ume fractions of the particles of the Retsch and Valmet grinding. In particle number fractions the differences were not so notable, the grinding technique used by TUT had slightly less small particles. After weighting the particle number with the volume of each fraction, the differences became notable. According to Figure 7.1 the Valmet mill seemed to produce clearly smaller particles than the Retsch mill.
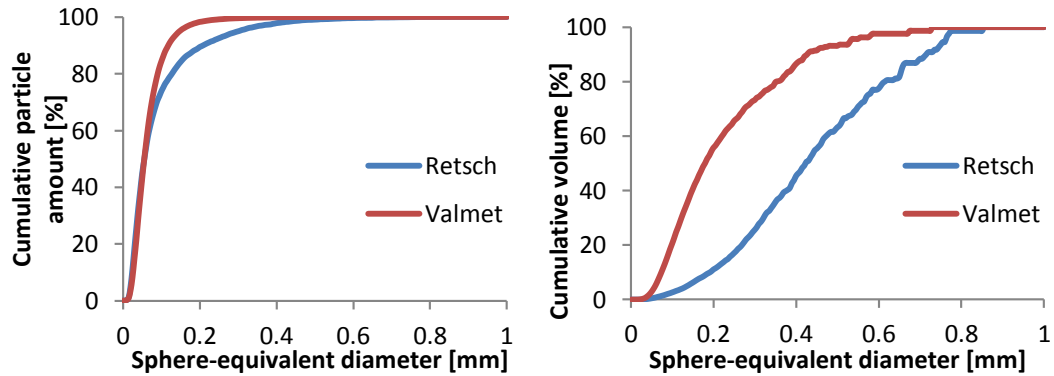

Figure 7.1. *Number and volume fractions of particles of sieving size under 500 μm.*

In Figure 7.1 the bigger particles have bigger volume and thus, large particles lead to higher steps in the cumulative volume curve. Images of the particles of both grinding techniques are presented in Figure 7.2. It can be seen in Figure 7.2 that both mills produced also bigger particles, but the relative amount of small and nearly spherical particles was notably higher with the grinding technique used by Valmet.

a)   b)
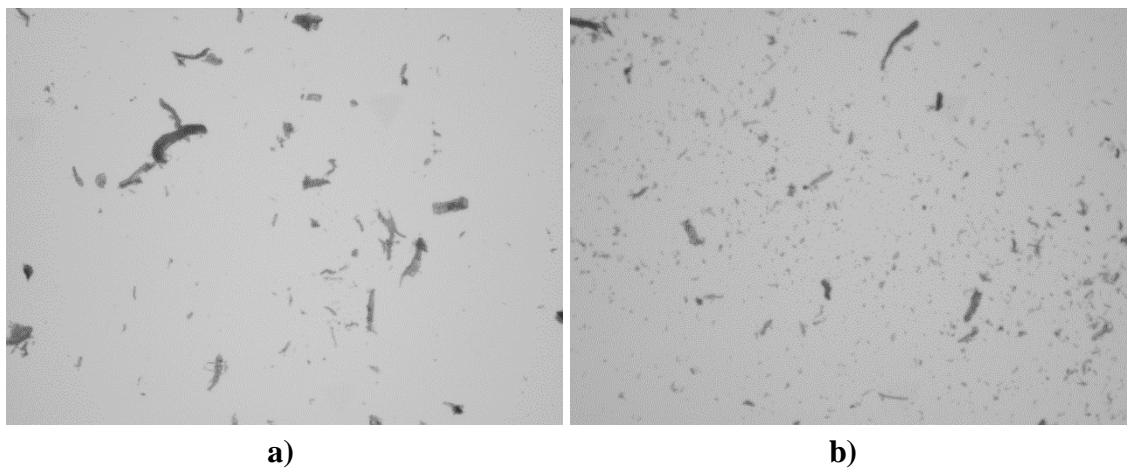
Figure 7.2. *Particle projections of sieving size under 500 μm **a)** Retsch **b)** Valmet grinding.*

The image of the identified particles of the Valmet mill is presented in Figure 7.3. The outlines of the identified particles are marked with green color. Only a part of the smallest particles could be identified due to a wide particle size distribution. The software had to be tuned to recognize both larger and smaller particles without cutting the bigger particles in parts. The presented results are not accurate rather suggestive because all images of certain size have been analyzed with the same tuning of the program, and therefore the smallest particles of both grinding techniques were partly unidentified.
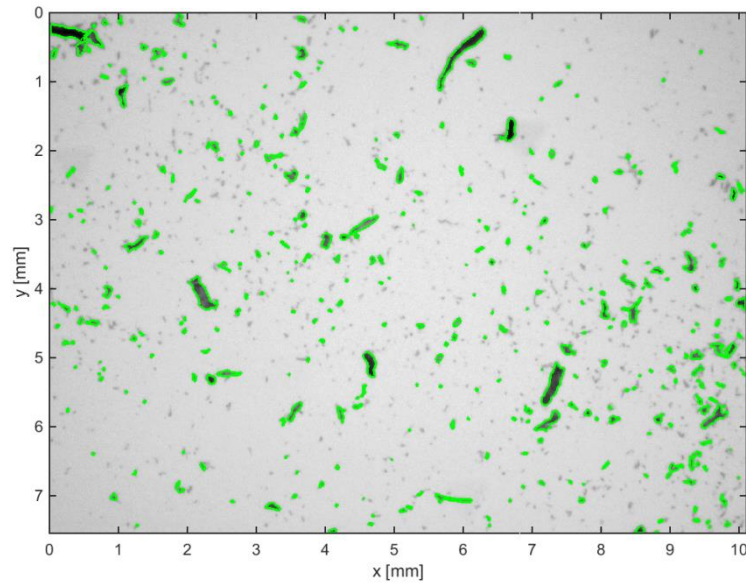
Figure 7.3. Identified particles of sieving size 0 - 500 μm of Valmet mill.

In order to eliminate the effect of the smallest particle size on particle analysis, the batch was sieved and pictured again. The volume fraction of sieving size of 112-500 μm is presented in Figure 7.4. Even though the finest particle fraction was sieved off, grinding technique used by Valmet produced more relatively small particle size.
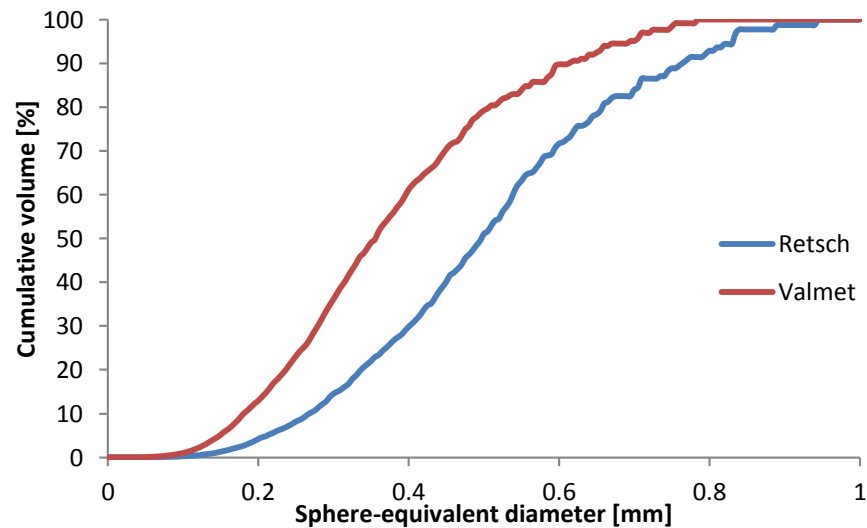
Figure 7.4. Volume fractions of sieving size of 112 - 500 μm.

The differences in the smallest size group can be partly explained by the fact that the minimum radial velocity was used in the Retsch mill. If the number of revolutions of the mill had been increased, the proportion of the smaller particle size would have increased as well. On the other hand, this would have affected the fraction of the bigger particles.

The number and volume fractions of the bigger particle size of the Retsch and Valmet mills are presented in Figure 7.5. There is no big difference in volume fractions in the

figure. Again the biggest particles distinguish clearly in Figure 7.5. Nevertheless, the grinding technique used by Valmet seems to have larger amount of smaller particles once again.
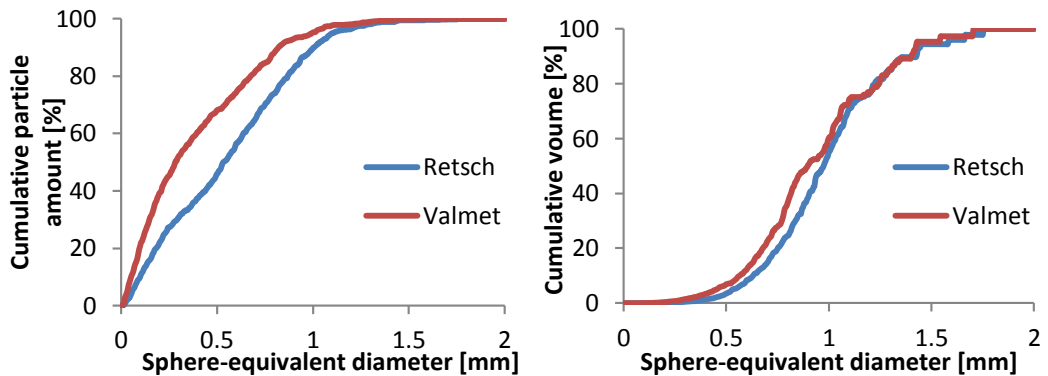
Figure 7.5. *Number and volume fractions of particles of sieving size over 500 μm.*

There seems to be a large amount of small particles on the light diffuser plate even though the sieving size was over 500 µm. The small particles did not affect to the size distribution due to their little volume which can be also observed in Figure 7.5, but it was in interest to find out where they originated from. It is possible that small particles were tied up to the larger ones. However, the difference between the grinding techniques in small particle size with sieving size over 500 µm was notable (Figure 7.5). Images of the particle projections are presented in Figure 7.6 and the difference in the milling techniques can be clearly seen in the figure. Particles of the Valmet mill were more non-uniform than those of the Retsch mill.

a)   *b)*
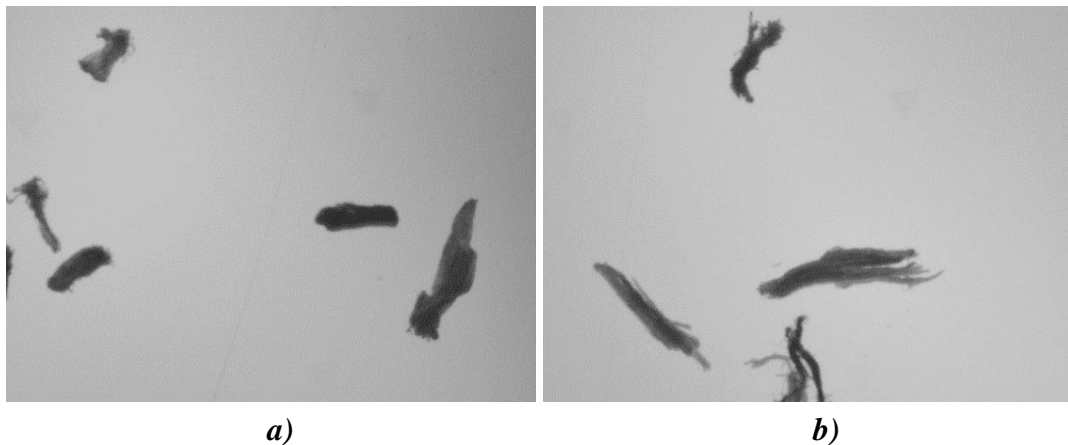
Figure 7.6. *Particle projections of sieving size over 500 μm **a)** Retsch and **b)** Valmet grinding.*

The particle identification software was originally developed to identify staggered particles and particles with uniform shapes which resulted in the program identifying multiple staggered particles from a single non-uniform one. A great example of the failure of the particle software identifying large non-uniform particles is presented in Figure 7.7.

These non-uniform particles are also able to tie more small particles, thus leading to a situation where more small particles end up on the light table.
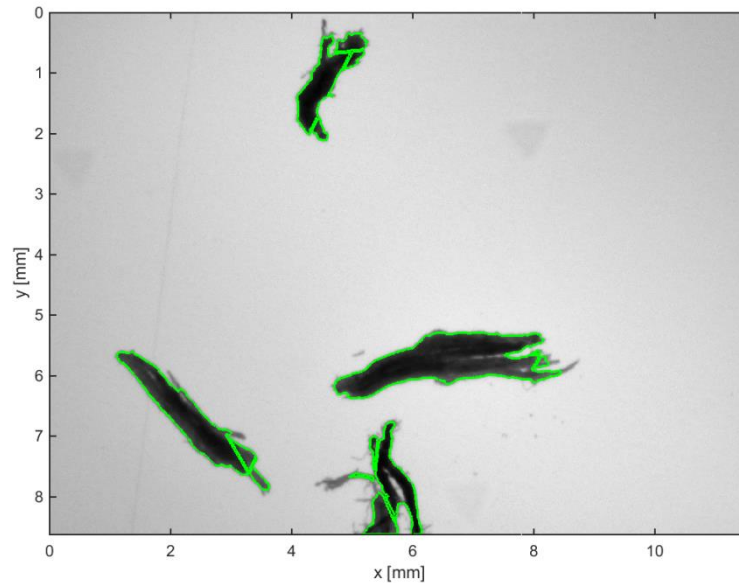
Figure 7.7. *Identified particle outlines of particles of Valmet mill with sieving size over 500 μm.*

The original goal of this study was to examine if the grinding technique affects the reactivity of the fuel particles. The non-uniform particles have much more surface area and porous structure might affect both pyrolysis and char oxidation. The grinding technique most likely affects the reactivity of the solid fuel particles. For this reason, the fuel ground with the Valmet mill was decided to use in the further experiments for determining the reactivity parameters of the fuels.

Aspect ratios of the particles of different milling techniques are presented in Table 2. In the group of smaller particles there were very little differences and if the smallest, almost spherical particles were sieved off there was no difference at all in aspect ratios. With the larger particles the Valmet mill produced little more elongated particles than the Retsch mill but generally the differences in aspect ratios were minimal. The already milled fuel was chosen for the experiments later on for this reason too.

Table 2. *Aspect ratios of particles of grinding techniques.*

Sieving size	Valmet	Retsch
<500 μm	1.9	2.1
112 - 500 μm	2.6	2.6
>500 μm	3.1	2.9

The particle aspect ratio is calculated by taking average of aspect ratios of all the identified particles and thus, it is not determined mass based. Although the particle analysis software could not identify the big particles perfectly it still describes well the shapes of those. However, knowing the limitations of the program it was possible to react critically to the results.

7.2 Biomasses for the experiments with drop tube reactor

For the combustion experiments two different biomasses were chosen. The first one was domestic biomass referred as biomass B1. The other one was more exotic biomass from abroad and it is referred as biomass B2 in the text. Two completely different biomasses were chosen for the tests because both of them are used or planned to be used widely in pulverized fuel combustion. They also provide some extra contrast for this thesis. Both biomasses were available in both pelletized and already ground form, and the ground form was chosen for the experiments.

Differences between the fuels were observed already in the sieving procedure. The smallest size fraction of biomass B1 was so dusty that it accumulated on the walls of the ring sieve. The sieving was conducted several times in order to prevent the dust ending up in the larger size fractions. On the other hand, the smallest size fraction of biomass B2 was so sticky that it accumulated on the bottom of the thickest sieves occluding them and preventing small particles to penetrate the sieve. Thus, the sieving was conducted several times with the biomass B2 as well. In order to obtain the real particle size distribution, the already milled fuels were sieved with sieving size intervals of 200 μm up to 1000 μm and the proportions were weighed. The proportions of the weighed fractions are presented in Figure 7.8.
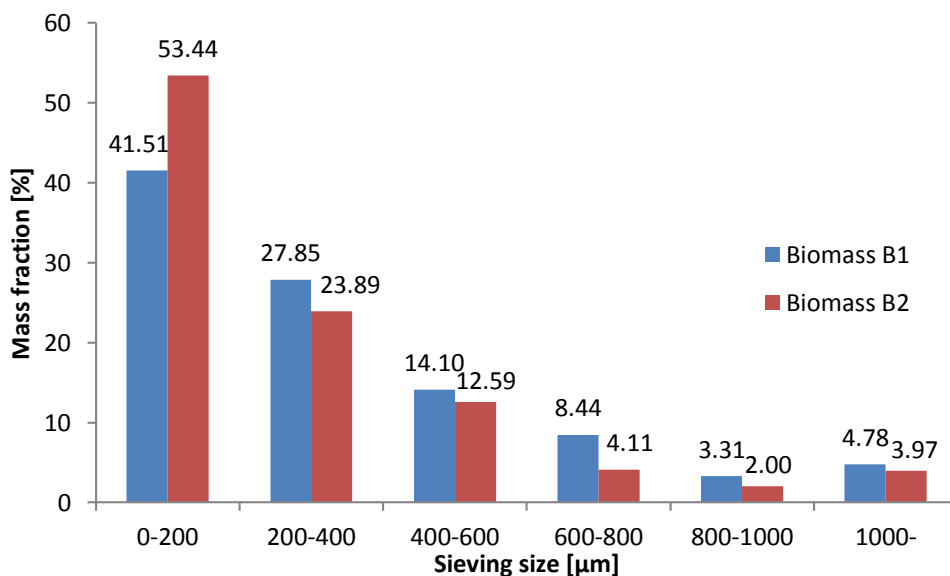
Figure 7.8. *Mass fractions of sieved biomass fuels B1 and B2.*

Biomass B2 contained notably more fine particles (sieving size 0 - 200 μm) than bio-mass B1. However, in larger particles the differences were not so obvious. The relative-ly high amount of proportion over 1 mm particles of both fuels can be explained by the fact that it consists larger size distribution than the other ones. The next sieve size from 1000 μm would have been 3150 μm and all the bigger particles would have penetrated it easily.

A CFD software Ansys Fluent uses a Rosin-Rammler expression in representation of the particle size distribution. The Rosin-Rammler distribution function is based on the assumption of an exponential relationship between the particle diameter d and the mass fraction of particles with a diameter greater than d, Y_d. The Rosin-Rammler function is presented in Equation 26. [62]

$$Y_d = e^{-(d/\bar{d})^n} \tag{26}$$

Fluent refers the quantity $\bar{d}$ as the mean diameter and n as the spread diameter [62]. Equation 26 represents a cumulative sum function of the measured particle mass frac-tions as a function of a particle size. Next, the least square error between the Rosin-Rammler function and the cumulative sum of the measured mass fractions was formed, and minimizing the least square error gives the best Rosin-Rammler fit for the cumula-tive mass fractions. The Rosin-Rammler fit for the particle size distribution and the measured cumulative mass fractions are presented in Figure 7.9.
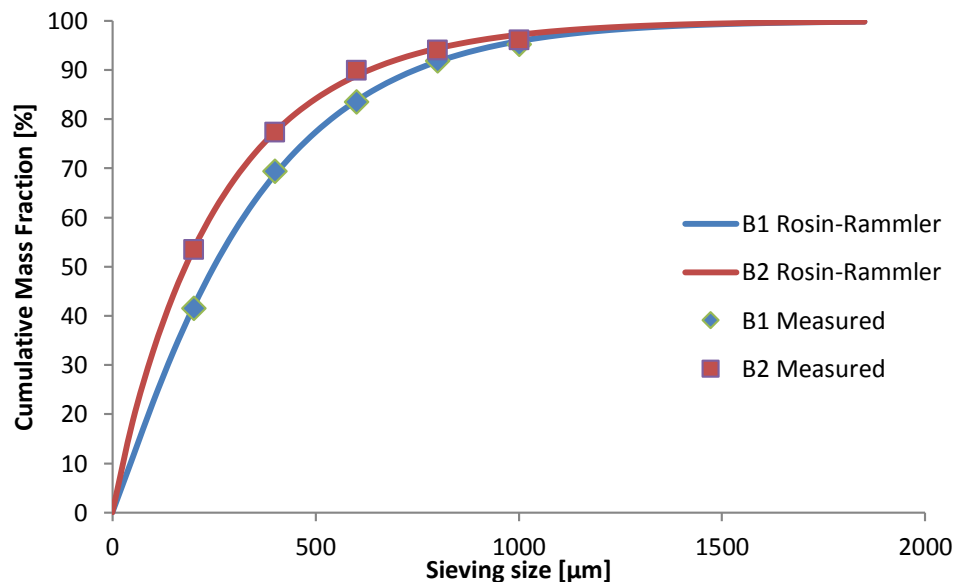
Figure 7.9. *Cumulative mass fractions of measured mass fractions and Rosin-Rammler fits for biomass fuels B1 and B2.*

The Rosin-Rammler expression describes well the measured particle size distributions which can be observed in Figure 7.9. The standard deviation of the absolute values of differences between the Rosin-Rammler expression and the measurements was 0.9 for

the biomass B1 and 0.5 for B2. The maximum deviation between the expression and the measurements is under 3 %. The values for parameters in Equation 26 are presented in Table 3.

Table 3. Parameters of biomass B1 and B2 for Rosin-Rammler formula.

	Biomass Fuel B1	Biomass fuel B2	B1 corrected with aspect ratio
$\bar{d}$ *(μm)*	349	264	542
n	1.10	0.95	1.10

The mean diameter has very little to do with the real particle mass mean diameter and in this context it refers only to the parameter of Equation 26. However, the sieving size describes only the smallest dimension of the particle. Thus, elongated particles may pass the sieve upright. Using the aspect ratios from Table 2, it is possible to estimate the sphere-equivalent diameters of the biomass B1 from the sieving sizes, and thus form the needed diameters in sphere-equivalent form, as described in the previous chapter. The sieving size is multiplied by the average of the aspect ratios of the larger and smaller particle sizes. Due to the linear behavior of the sieving size and the sphere-equivalent diameter, spread diameter remains constant for both cases which can be observed in the last column of Table 3. The mass fractions as a function of the sphere-equivalent diameters and the Rosin-Rammler fit are presented in Figure 7.10.

Figure 7.10. Aspect ratio corrected size fractions of B1 and Rosin-Rammler fit.

The results for the combustion parameters are strongly dependent on how the particle sizes and shapes are taken into consideration. The assumption of sphere-equivalent par-

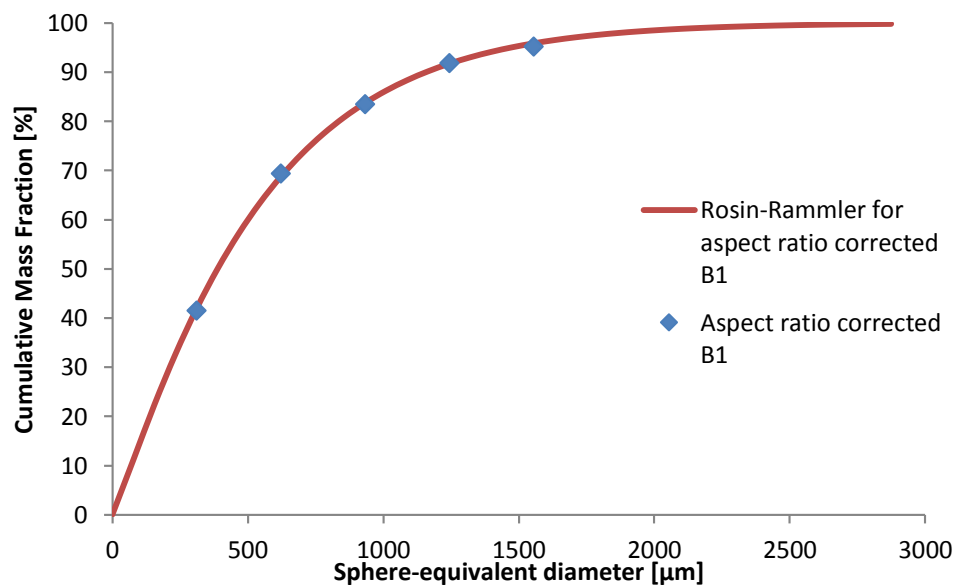ticles underrates the reactive surface area of the elongated particles, e.g. two spherical particles have 26 % larger surface area than a single spherical particle with the same volume. However, the basic models used by Fluent use the surface area only in heat exchanging models, not in pyrolysis models. The surface reaction models, i.e. char oxidation models, use the particle surface area [62], but it has noticed that at the end of pyrolysis even the most elongated particles are almost spherical. If the combustion parameters are tuned with the systematic assumption of spherical particles, the parameters represent their conversion correctly.

The goal of this thesis was to determine the reactivity parameters for the fuel injected to the industrial scale boiler and therefore the whole size distribution of the ground fuel had to be represented. For the pyrolysis and combustion experiments three different size categories were chosen, namely sieving sizes of 112 - 125 μm, 500 - 600 μm and 800 - 1000 μm, in order to represent the fuel size distribution as well as possible. The selected sieving sizes are referred in the text as *a*, *b* and *c*, respectively. The first sieving interval of 112-125 um was selected because the previous combustion tests had been conducted for this particle size [12, 74]. This made the results comparable with each other. The sieving process was conducted several times in order to prevent the smallest size fraction from remaining in the sieved batches.

All the six batches were pictured and the images were analyzed with the particle identification program. Pictures of the particles of different size fractions and fuels are represented in Figure 7.11. For the larger particles the camera was adjusted further from the light diffuser plate and the pictures were taken diligently in order to get the larger particles into the same picture completely. It was extremely hard to drop the smallest size fraction of biomass B2 as single particles and they ended up dropping as clusters which can be seen in Figure 7.11.

Figure 7.11. *Pictures of particle projections on the light diffuser plate: On the left biomass B1a, B1b and B1c, and on the right B2a, B2b and B2c, respectively.*

In Figure 7.11 the differences between the fuels can be seen clearly. The main shapes of the B1 particles look similar in all size fractions. Each of the size fractions of B1 is comprised of elongated particles, only in the smallest size fraction the non-uniform end of the particles is not so clear. However, the larger particles are stragglier. Biomass B2 consists clearly of two different fractions. The particles of the smallest size fraction B2a, which represents approx. half of the mass of biomass B2 according to Figure 7.8, are dusty and sticky, and thus they tend to form clusters. The larger particles on the other hand are highly elongated and thin, and they are often highly curved. It is quite clear that the small and large size fractions of B2 are not composed of the same substance.

The pictures of B2b and B2c also show that the small particles ended up on the light plate even though the batches of the particles were sieved for several times.

After the particles scattered on the light diffuser plate were pictured, the images were analyzed with the particle sizes and shapes identifying software. Thus, the size fractions of the sieved batches could be obtained and they are presented in Figure 7.12. The particles of different batches contained relatively large size fractions even though they were carefully sieved. The size fractions of biomass B1 seem to be consistent: the larger sieving size induced the size fraction consisting larger particles. However, the same influence of sieving size on the particle size was not observed with biomass B2. Obviously the smaller sieving size lead to smaller sphere-equivalent particle diameter, but especially with larger particles the differences were not as notable as they were with biomass B1. The reason for this effect was partly the highly elongated shape of the bigger particles. Thus, the particles of the size groups of 500-600 μm and 800-1000 μm were quite similar. The largest size fraction (B2c) only contained more elongated and slightly thicker particles than B2b.
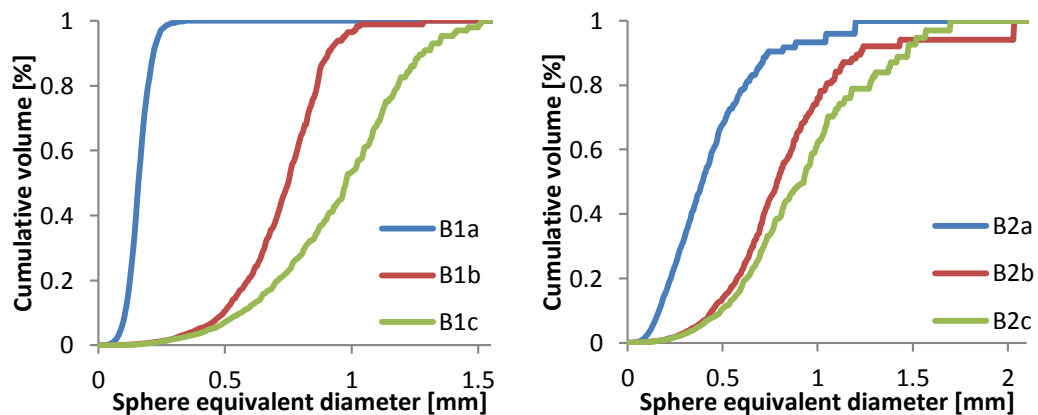
Figure 7.12. Volume fractions of different size groups of biomass B1 and B2.

As mentioned before, the particle shapes and sizes identifying software had major difficulties in handling non-uniform particle sizes, and therefore uncertainties in particle identification exist with particles of B1b and B1c. However, long and highly curved particles of the biomass B2 were not ideal particles for the software either because the software identified several particles, which it handled as staggered particles, from a single curved one. Thus, the results of particle sizes of the biomass B2 are highly uncertain. In addition, images in which the particle outlines limited an area consisting empty space were also considered as extremely large particles by the software. Thus, particles had to be scattered on the light diffuser plate in a way that they did not restrict any large areas.

In Table 4 particle shapes and sizes of all the size fractions of biomasses B1 and B2 are presented along with the particle amount of each size group. In the measurements of particle shapes the amount of pictured particles was tried to keep high in order to en-

hance the accuracy of the results. In comparison between biomasses B1 and B2, larger particles are of the same size. However, the particles of B2a are more than twice as large as the particles of B1a. In addition, the particles of B2a seem to have aspect ratio of 2.1 even though according to Figure 7.9 B2a particles are relatively spherical. The particles of B2a were in clusters on the light diffuser plate, and thus the particle shapes and sizes identifying software was incapable to analyze shapes of these particles.

Table 4. Particle shapes and sizes from the analysis.

Fuel	Number of identified particles	Mean diameter [µm]	Mass mean diameter [µm]	Aspect ratio
B1a (112-125 µm)	8795	107.4	162.1	2.54
B1b (500-600 µm)	2474	215.3	750.9	2.38
B1c (800-1000 µm)	2332	279.1	981.9	2.79
B2a (112-125 µm)	5718	119.1	398.6	2.10
B2b (500-600 µm)	3467	139.3	790.9	2.54
B2c (800-1000 µm)	4084	123.8	931.0	2.44

Combustion characteristics of the fuels were partly guessed. Specific heat of virgin wood (1500 J/kgK) was used for the biomass B1 [15, 75]. Specific heat of 1400 J/kgK was used for biomass B2 based on an investigation of a similar fuel [76]. The proximate analysis for both of the fuels was conducted by Valmet and the results of them are presented in Table 5. The differences between the fuels can be seen clearly in the table. Biomass B1 has much higher volatile matter and much less ash than biomass B2. The composition of oxidizing matter is quite similar and the biggest differences are in the amounts of ash and oxygen. However, high ash and chlorine content make biomass B2 much more challenging in the combustion applications as described in the third chapter. Also the ash deformation temperature of the biomass B2 is nearly 500 ℃ lower than that of B1 making the biomass B2 more fouling and slagging fuel.

Table 5. Fuel composition and properties for biomass B1 and B2.

	Biomass B1	Biomass B2
Volatile matter (m-%)	84.1	73.2
C (m-%)	49.4	48.5
H (m-%)	6.2	5.8
N (m-%)	<0.1	1.14
O, calculated (m-%)	43.1	36.4
Ash 815°C (m-%)	0.83	8.0
Cl (m-%)	<0.005	0.53
Ash deformation temperature (^{o}C)	1440	990
Specific heat (J/kgK)	1500	1400

Another quantity affecting strongly the solid fuel combustion process is the particle density as mentioned in the third chapter. The particle intrinsic density can be determined with a mercury porosimeter. The mercury porosimeter can identify pores of a solid sample between 500 μm and 0.0035 μm. The mercury porosimeter determines the particle porosity by applying several pressure levels to a sample immersed in mercury. The sample is in a vessel immersed with mercury and at first the vessel is evacuated into vacuum in order to remove air, other gases and residual moisture. After this the system pressure is increased gradually and the mercury intrusion into the sample is determined by measuring the decrease on the mercury in the porosimeter. As the pressure increases mercury intrudes the smaller and smaller pores finally filling the spaces between the fibers. The maximum pressure of the porosimeter could be as high as 400 MPa. By taking into account the fluid (mercury) properties and the system pressure the pore size can be calculated. With mercury porosimetry e.g. the skeletal and apparent density, the pore size distribution and the total pore volume could be determined. [77]

Biomass B2 clearly consisted of two different fractions, and therefore both fractions were tested separately. Smaller and larger fractions of B2 were tried to separate as well as possible in order to obtain realistic results for both of them. The sieving size of 200 μm was used to separate the smallest and largest size fractions from each other. The mercury porosimeter results for B1 and for two fractions B2 are presented in Figure 7.13. The mercury porosimeter of Tampere University of Technology was broken but similar apparatus was found in Åbo Akademi and the samples were send to Turku.
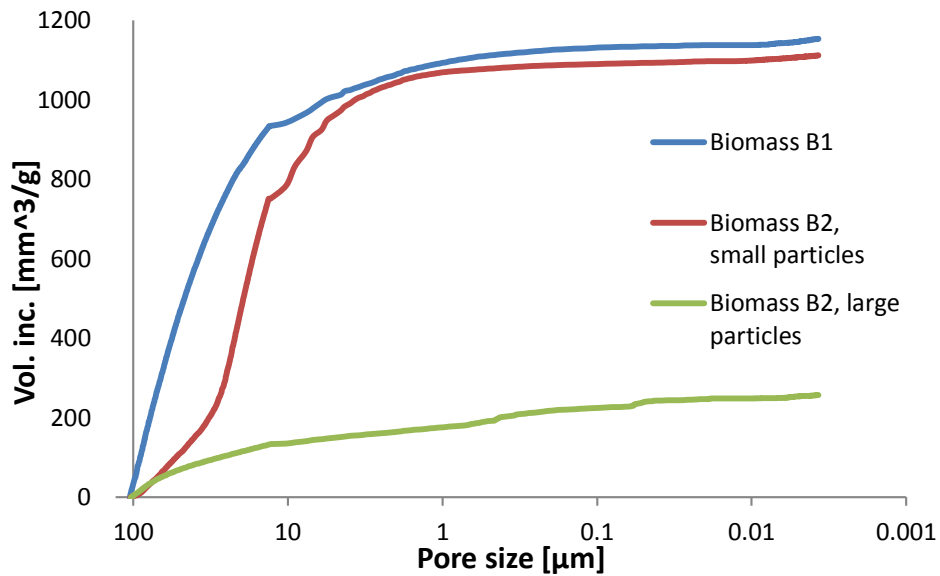
Figure 7.13. *Mercury porosimeter results for biomasses.*

In Figure 7.13 a clear stabilizing can be observed in the pore size of approx. 15 μm indicating that the mercury starts to intrude into the pore system. Thus, using this pore size would be justified in determining intrinsic density of the particles. The camera resolution seems to be that size as well. However, the particle shapes identifying software was not capable of recognizing particles with that accuracy. The smallest pores the software was able to identify appeared to be approx. 50 μm, and thus this pore size was used in determining the apparent density used in simulations. In Table 6 the bulk and apparent density of biomasses are presented. In the table also the calculated porosities of the fuels are presented.

Table 6. *Determined densities and porosities of biomasses.*

Fuel	Bulk density (kg/m^3)	Apparent density (kg/m^3)	Porosity
Biomass B1	527.7	699.795	0.5189
Biomass B2, small fraction	565.9	603.611	0.3955
Biomass B2, large fraction	1212.2	1324.871	0.7522

The differences in the fuel densities can be seen clearly in Table 6. Also differences between the smallest and largest size fraction of the biomass B2 are clear. The density of the large particles of biomass B2 is more than twice as large as that of the small particles. Tiny particles cannot retain any large pores, and thus the porosity of the small particles of the B2 is notably lower than that of the larger particles. If the difference in

particle densities is that notable, it is highly possible that other combustion properties such as specific heat differ as well. However, the specific heat of 1400 J/kgK was used in simulations for both size fractions of B2 due to lack of better knowledge.

7.3 DTR temperature and particle velocity profiles

In modeling of the conversion process of the particles, the wall and gas temperatures were required in order to model the heat transfer phenomenon. The wall temperature profiles of the drop tube reactor were obtained from the eight thermocouple measurements in the reactor wall. In order to present the results in simplified form and in the same picture the wall and gas temperature profiles were averaged. More accurate method would have been using the unique profiles from the different drop heights but this would have led to a group of curves and an illustrative presentation of the results would have been difficult.

The gas temperature profile inside the reactor was achieved by measuring the temperature in the reactor centerline with thermocouple. However, the thermocouple was lacking a radiation shield, and thus the radiative heat transfer between the thermocouple and reactor wall should have been excluded. In the previous experiments the thermocouple temperature measurements were corrected by calculating heat transfer and conduction effects of the thermocouple [74]. Another option was to calculate the gas temperature profile by using CFD.

The other thesis worker, M.Sc. Niko Niemelä, was modeling the fluid flow and particle combustion in the DTR with Ansys Fluent meanwhile the experiments were conducted. At first he conducted simulations in which the thermocouple was modeled in the DTR. Due to the laminar flow in the reactor the modeling setup consisted laminar flow field modeling and energy calculation. In order to take into account the thermal radiation between the wall and the thermocouple, the radiation model "discrete ordinates" was included in simulations as well. The wall temperature was obtained from the DTR measurements. According to simulations, thermocouple readings correlated highly with the wall temperature, and thus using them directly would have caused significant error in the calculations. [78]

In Figure 7.14 the results of the CFD simulation of the DTR are presented. The simulated gas temperature rising speed after the injection probe was much slower than the thermocouple measurements which can be seen in Figure 7.14. However, the modeled thermocouple temperatures predicted quite accurately the measured readings of the thermoelement, and thus the simulated gas temperature profile was assumed to be accurate enough as well. In the figure the simulated drop height is 48 cm. The differences between modeled and measured thermocouple readings in Figure 7.14 at the positions of 52 - 56 cm resulted from the fact that in the simulation the reactor optical window was not yet modeled. [78].
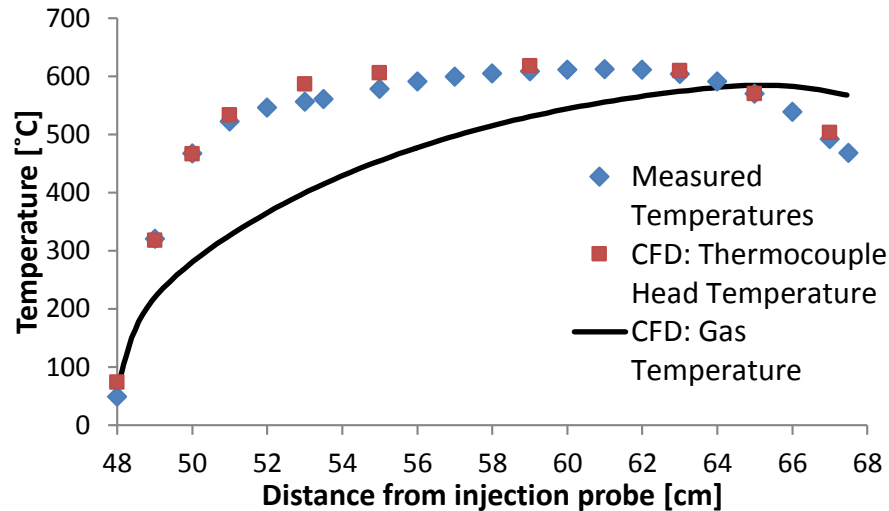
Figure 7.14. *Simulated gas and thermocouple end measurement with thermocouple measurements from CFD simulation [78].*

Because the CFD simulations provided quite accurate results, the gas temperature profile was decided to model with Fluent. The grid for Fluent simulations was got from Niko Niemelä with many useful advices concerning CFD modeling. Nitrogen and oxygen are both symmetrical gas molecules, and thus absorb and emit negligible radiation in temperatures of the drop tube reactor [79]. Therefore, the thermal radiation from the walls does not affect the gas temperature and the radiation model was not included in the simulations.

According to the simulations the drop height affects strongly the gas temperature profile due to pre-heating of the gas between the hot reactor wall and the cooled injection probe. The longer the distance gas had to heat the more rapid temperature rising speed of the gas in the reactor centerline was after the injection probe. Gas pre-heating affects also the vortex occurring immediately after the injection probe. Thus, if the gas is not pre-heated at all no vortex was observed in the simulations. The vortex appeared in the simulations after the probe end and there is experimental data also indicating its existence. E.g. the particle velocity rose rapidly after the probe and lowered after a while. The simulated velocity contours in the direction of the main flow field are presented in Figure 7.15.
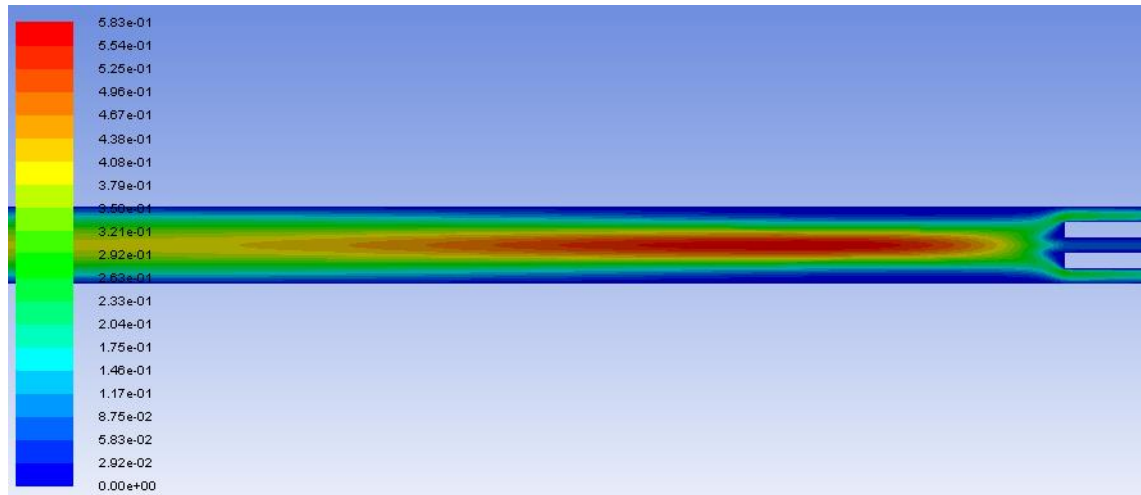
Figure 7.15. Velocity contours from CFD simulations of DTR.

The optical window of the DTR was not yet modeled in the simulation Figure 7.15. According to the simulations in which the window was modeled, the window affected to heat transfer of the thermocouple and created a vortex after the window transferring cooler fluid from the non-heated window pipe to the center of the reactor [78]. However, this phenomenon was not taken into account in determining the gas temperature profile in this thesis. The gas temperature profile was obtained as an average of the temperature profiles of the CFD simulations in the reactor centerline at two different drop-heights. The selected drop-heights were 17.5 cm and 47.5 cm and the simulated gas temperature profiles in 600 °C and 900 °C are presented in Figure 7.16.
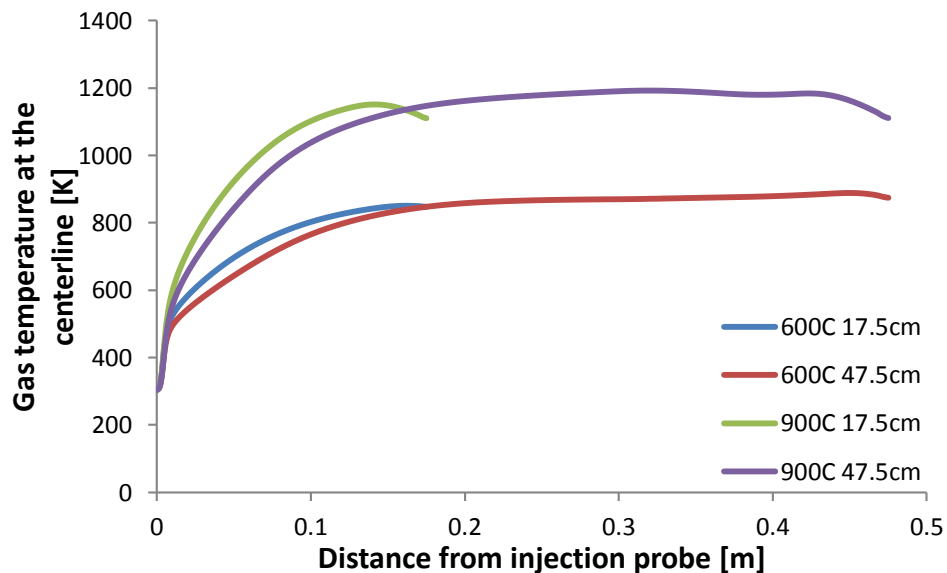
Figure 7.16. CFD simulations of gas temperature profiles in the reactor centerline.

The difference between the temperature profiles from the different drop-heights can be seen in Figure 7.16. As mentioned earlier, the lower drop height the more time gas has to pre-heat between the feeding probe and the reactor wall, thus leading to higher gas

temperature rising speed after the probe. The gas and wall temperature profiles used in modeling particle combustion were represented with an analytical equation, which is described in Equation 27.

$$T(s) = T_{initial} + \left(1 - e^{-\frac{s}{\tau}}\right) * \left(T_{final} - T_{initial}\right) \tag{27}$$

In Equation 27 the terms $T_{initial}$ and T_{final} represent the initial and final temperatures of the gas and wall, respectively. In the equation $s$ represents a place step and τ is the factor which may tuned in order to get the equation representing the temperature rising speed correctly. The value for τ was obtained by minimizing the least square sum function of the difference of the measured temperature profile and Equation 27 by changing the value of τ. The same method was used for the wall temperature profiles in different temperatures. In Figure 7.17 the temperature profiles for both gas and wall temperatures are presented. The parameters for Equation 27 for different temperature levels are presented in Table 7.

Table 7. *Parameters for Equation 27 for gas and wall temperatures.*

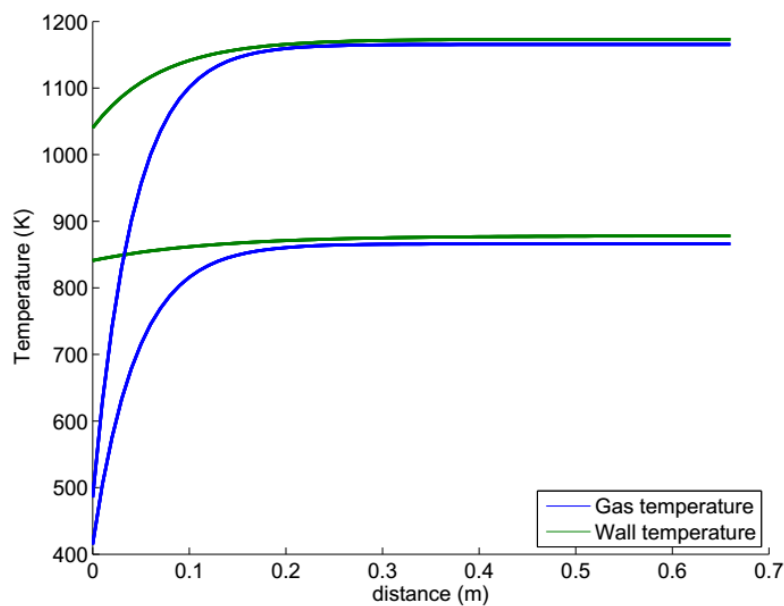| Temperature	$T_{initial,wall}$	$T_{final,wall}$	τ_{wall}	$T_{initial,gas}$	$T_{final,gas}$	τ_{gas}
600 ºC	838 K	878 K	0.123	304 K	866 K	0.046
900 ºC	1020 K	1173 K	0.070	304 K	1165 K	0.042

Figure 7.17. *Gas and wall temperature profiles used in simulations.*

In Figure 7.17 the upper set of curves represent the temperature profiles in 900 ºC of the gas and wall, respectively. The lower curves are the temperature profiles in 600 ºC. The

increase of wall temperature in 900 °C was relatively slow as well. A little drop of temperature in the end of the reactor due to unheated 2.5 cm of the reactor end is not modeled because the temperature drop moved along when the drop height was changed and the averaging eliminated its effect. However, it was assumed to have a very little effect on the particle temperature history, and therefore it was neglected.

The optical window in the reactor and the particle imaging setup was used to determine the particle velocity profile. The particle identification software was used to identify the particles in the double exposed images and determine the particle falling velocity. The particle velocity from a single drop-height was determined by averaging all the measurements of the specific drop-height. However, only the experiments in pure nitrogen could have been used in determining the particle velocity. When the reactor atmosphere contained oxygen the volatile compound was burning in a layer outside the particle and the particles were shown in images as bright spots. Thus, the particle identification software was not able to identify the particles and determining the particle velocities was impossible in combustion tests. The same velocity profile was used for all the measurements. The picture of particles of biomass B1a falling inside the DTR was presented in the previous chapter (Figure 6.4). The particle velocity was modeled with an analytical equation which is presented in Equation 28. Even though the particle velocity determining software tabulated the particle sizes in addition to the particle falling velocity, only the average velocity of the measurements was used.

$$v_p(s) = v_0 + \gamma \frac{s}{\beta} e^{-\frac{s}{\beta}} - (v_0 - v_{fin})\left(1 - e^{-\frac{s}{\delta}}\right) \tag{28}$$

In Equation 28 the term $v_p(s)$ is the particle velocity at the place s, and γ, β and δ are the model parameters. Values for the parameters were obtained by minimizing the least square sum of the difference between Equation 28 and the measured velocities. The number of images of the particles of the smallest size group of both biomasses was rather high, and therefore determining the particle velocity was relatively accurate for them. However, the number of pictures of the larger particles in some specific drop heights was so low that great inaccuracy occurred in the results. In addition, the amount of smaller particles was always higher in all size groups, and thus the smaller particles were over-emphasized. The measured particle velocities and a fitted curve for the particles of B1a are presented in Figure 7.18. In the figure also the standard deviations of the measurements are presented.
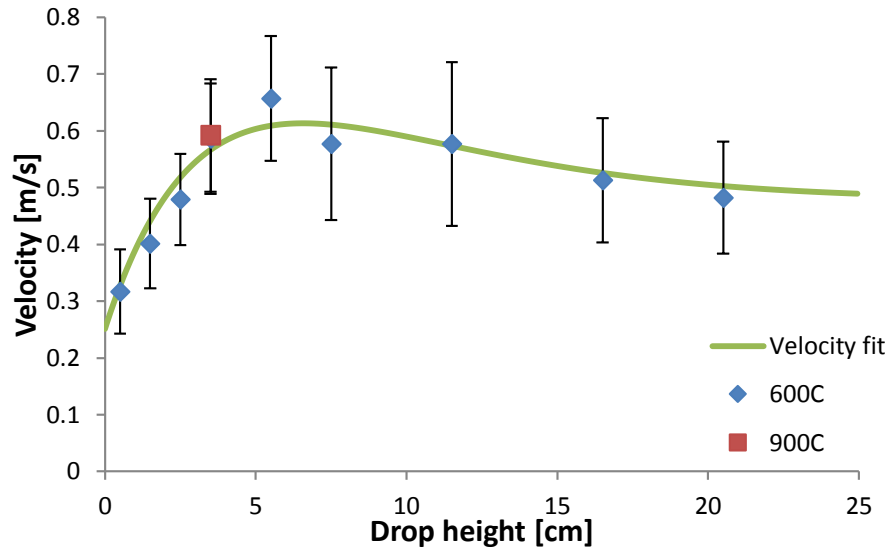
Figure 7.18. Velocity fit and measured particle velocities of particles of B1a.

The particle falling velocity increases rapidly and has its maximum at approx. 6 cm drop height. After that it settles on a lower level. This supports the observation of a vortex after the injection probe according to the CFD simulations (Figure 7.15). According to the simulations of the gas velocity profile and the measurements of the particle velocities, the slip velocity remained nearly constant for smaller particles. For the smallest size fraction of biomass B2 the velocity profile was quite similar, as presented in Figure 7.19. The peak velocity of the B2a particles was higher but on the other hand the final velocity was smaller than those of B1a. This can be explained by the fact that the fine fraction of B2 had lower density, and therefore it imitated the gas velocity profile better.
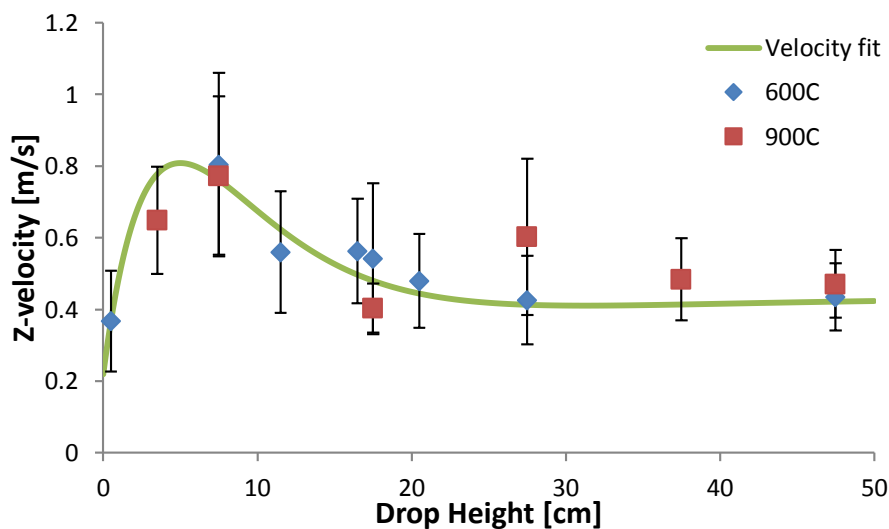
Figure 7.19. Velocity fit and measured particle velocities of particles of B2a.

It is worth of noting that B1b was the only one of the larger particles which the parameters could be achieved for by fitting them directly to measurements. The velocity profile for B1b particles with particle velocity measurements is shown in Figure 7.20. Howev-

er, it was decided by eye that the velocity profile fits for the particles of B2b as well. Initially the particle velocity profile obtained for B1b was used also for the B1c, i.e. the largest particles of the biomass B1. However, it is highly unrealistic to assume that larger particles would have the same velocity profile than the smaller ones, and thus the CFD simulations were used to obtain more accurate results. Fluent uses shape factor in calculating the drag force of non-spherical particles [62]. The shape factor was tuned to represent the particle residence time in the reactor for the particle size groups of B1a and B1b by Niko Niemelä. Then the same shape factor was used to obtain the particle average velocity profile of B1c and the parameters for Equation 28 were optimized by using the velocity profile of the CFD simulations. [78] The velocity profile of B1c is presented in Figure 7.21 with the measurements of particle velocities.

Figure 7.20. *Velocity fit and measured particle velocities of particles of B1b.*
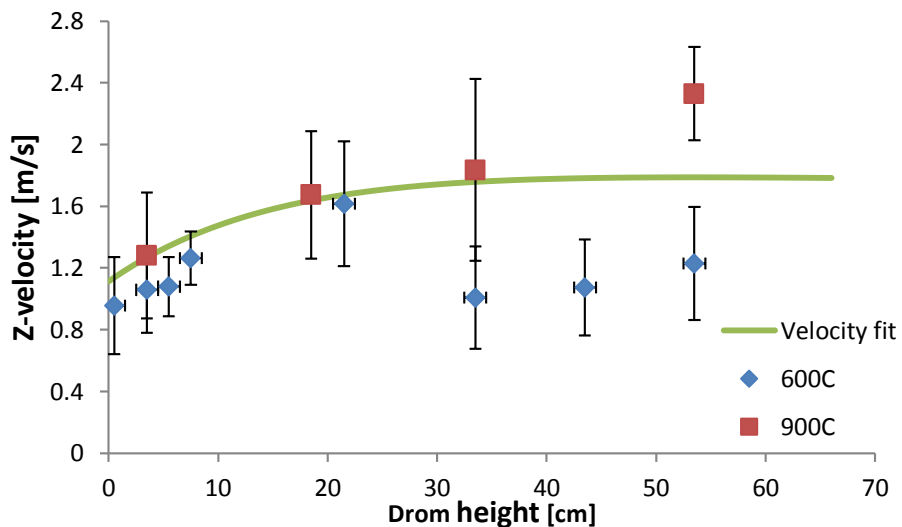
Figure 7.21. *Velocity fit and measured particle velocities of particles of B1c.*

As shown in Figure 7.20 the velocity fit was able to describe the particle velocities of the small particles very well due to a large amount of pictures taken. On the contrary,

the amount of pictures of the biggest particles of both biomass B1 and B2 was much lower, and thus there was relatively large dispersion in velocity measurements which can be seen e.g. in Figure 7.21. The reason for slightly higher particle velocity in 900 ºC could be that due to a higher conversion rate the size of the smaller particles was already decreased such that they were ignored in particle velocity determination. Actually the particle velocity should be lower in higher temperatures due to higher mass loss of the particles. The fitted velocity curves for the larger particles of biomass B2 are presented in Figure 7.22 and Figure 7.23. The parameters for velocity profiles of all size groups of both biomasses are presented in Table 8. In the table the slip velocities used in determining the particle convective heat transfer with Equations 4 and 5 are presented as well.
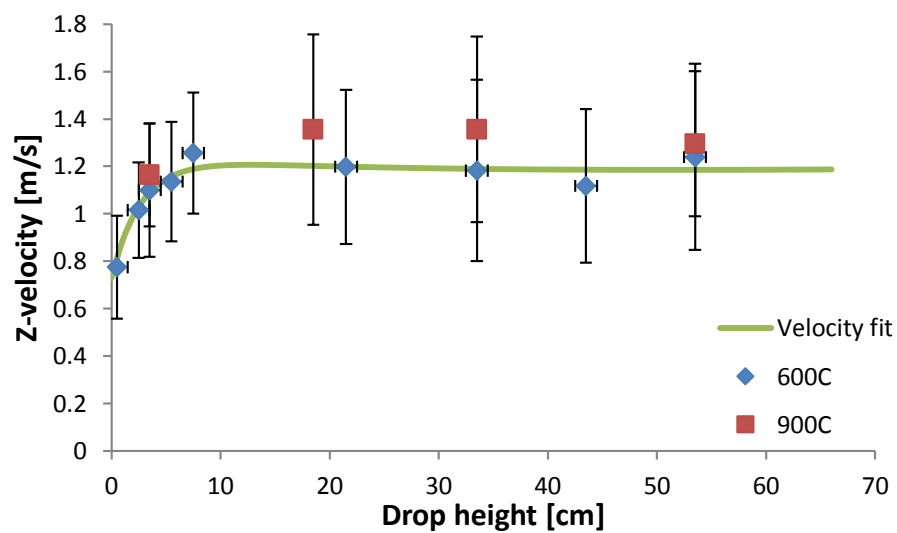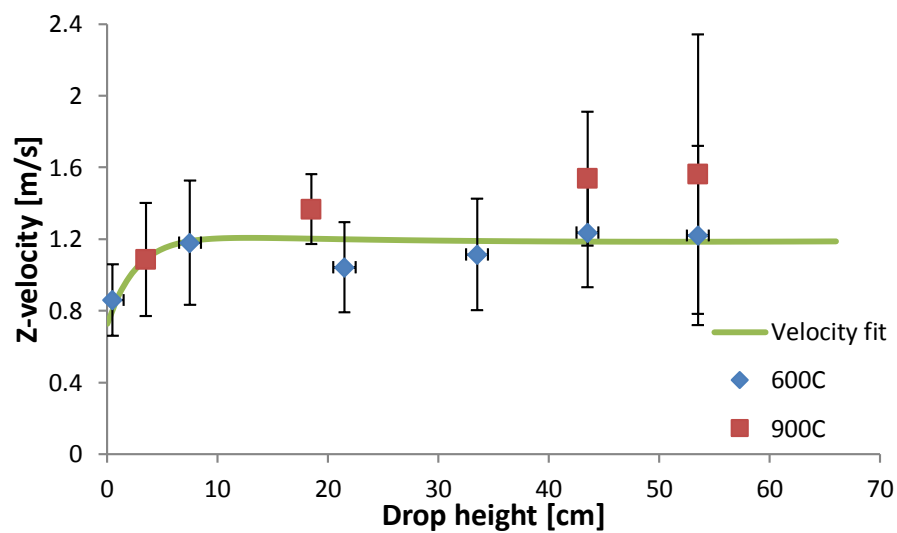

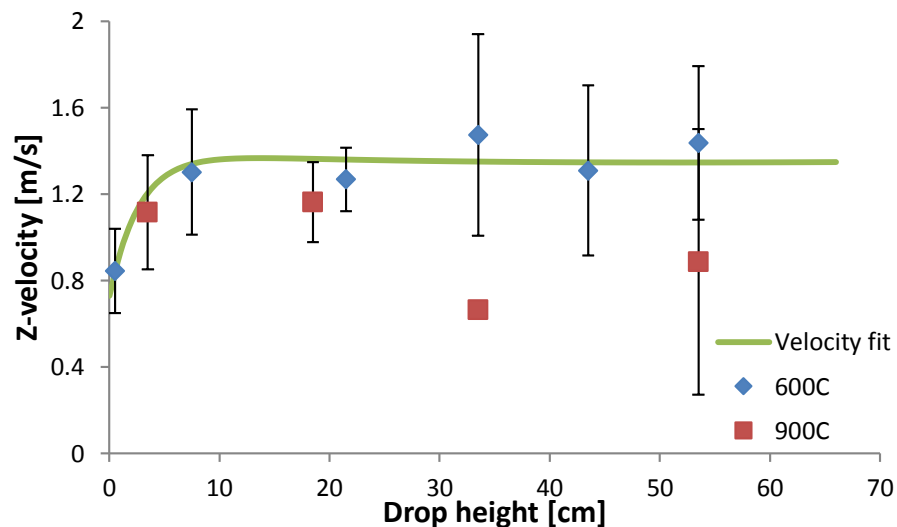*Figure 7.22. Velocity fit and measured particle velocities of particles of B2b.*

Figure 7.23. Velocity fit and measured particle velocities of particles of B2.

Table 8. *Parameters of Equation 28 for biomass B1 and B2.*

	V_0	V_{fin}	γ	β	δ	V_{slip} (m/s)
B1a	0.251	0.482	-0.777	0.055	0.155	0.15
B1b	0.729	1.240	0.150	0.514	0.027	0.85
B1c	1.112	1.752	-0.434	0.216	0.216	1.45
B2a	0.219	0.435	-1.166	0.042	0.026	0.15
B2b	0.729	1.240	0.150	0.514	0.027	0.85
B2c	0.729	1.400	0.150	0.514	0.027	1.05

It should be mentioned that the larger particles are accelerated slowly by the flow field, and thus the assumption of the constant slip velocity could be incorrect. Particles of B2c seemed to have higher velocity but the same velocity profile shape than the particles of B2b. Thus, the velocity profile obtained for B1b was corrected by increasing the value of V_{fin} in Equation 28 so that it described the particle velocities of B1c as well. The other parameters were left as they were for smaller particles, as shown in Table 8.

7.4 Experiments with drop tube reactor

The main part of the thesis was the experimental section with the drop tube reactor and it formed the basis for the whole study. The experiments lasted for four months which was half of the whole time originally planned to spend for this thesis. Biomass B1 was the first fuel arrived, and therefore experiments were started with it. The first experiments were conducted in nitrogen in 600 ºC temperature and by comparing the images of the particles dropping inside the reactor, the proper screw feeder was validated. The goal was to inject enough fuel into the reactor to keep the error caused by scaling minimal, but however keep the particles mostly separated while dropping inside the reactor. The screw feeder had to be quite thin in order to inject single particles of the dusty biomass B1a into the reactor.

Pyrolysis experiments were conducted in two temperatures, namely 600 ºC and 900 ºC. The combustion experiments were conducted at the higher temperature level (900 ºC) in order to simulate the temperature level in the actual combustion chamber better. This also speeded the measurement procedure significantly because the already heated reactor could be used for pyrolysis tests in 900 ºC and for both combustion tests. The results of the experiments for the small, medium and large size fractions of B1 are presented in Figure 7.24, Figure 7.25 and Figure 7.26, respectively. One point in the figures repre-

sents an average of measurements from a single drop height that consisted of 2 - 4 separate measurements. Standard deviations of the measurements are also shown in the figures. The reason for a large amount of experiments for B1 in lower temperature in the figures was that in the beginning of the experiments the screw feeder and the whole experimental procedure had to be validated due to lack of experience with the DTR.

Figure 7.24. Measurements in DTR with B1a.
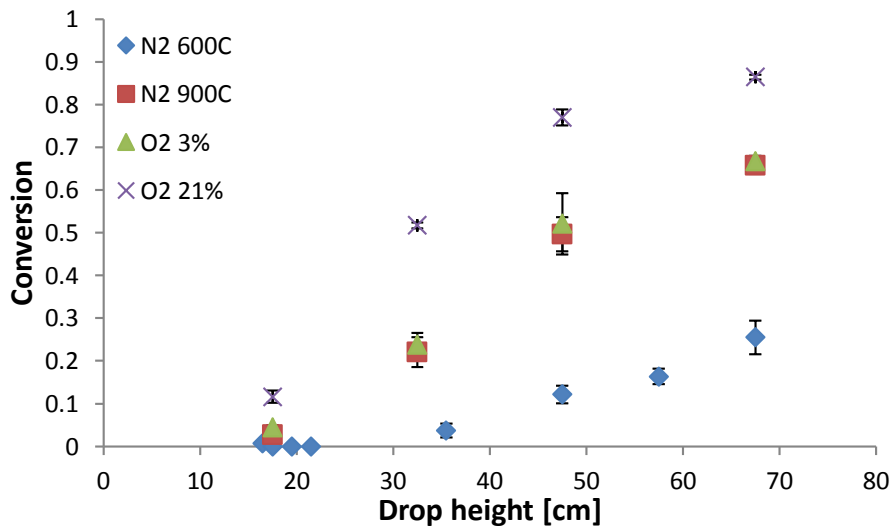
Figure 7.25. Measurements in DTR with B1b.
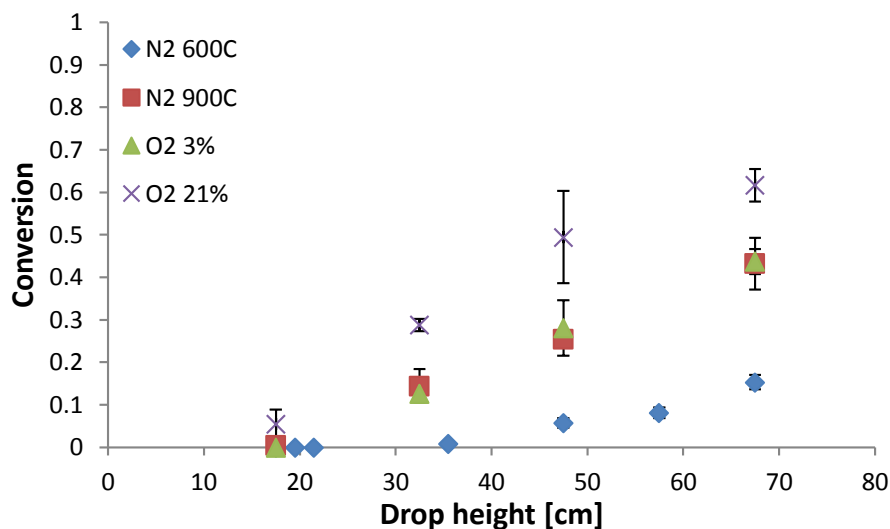
Figure 7.26. *Measurements in DTR with B1c.*

In the figures it can be clearly seen the effect of temperature on the conversion curve. Raising the temperature by 300 ºC multiples the rising speed of the conversion curve. In the figures the effect of oxygen concentration on the conversion behavior can be observed clearly as well. With 3 % of oxygen the conversion curve changes slightly compared to the pyrolysis experiments with the smallest size fraction B1a (Figure 7.24) but has no effect on the conversion curve of larger particles. The model assumption of consecutive combustion phases seems to be rather valid in low oxygen concentration for the bigger particles as well. Surprisingly, the smallest size fraction seems to be the one with the most notable differences between pyrolysis and 3 % oxygen experiments. However, only a part of the conversion curve of the larger particles could be presented because the length of the DTR was not enough for full conversion of the particles.

When the oxygen concentration was increased the shape of the whole conversion curve changed completely from the very beginning. This behavior can be observed also in Figure 7.24 but in Figure 7.25 and Figure 7.26 the effect of increased oxygen concentration is more emphasized. Thus, the model assumption of consecutive combustion phases is clearly not valid for the higher oxygen concentrations.

The particles of B1a were pictured not only before the heat treatment in the drop tube reactor but after the experiments as well. The swelling factor described in the fifth chapter was validated based on the images of the particles. According to analysis of the pictures taken before and after the heat treatment, the swelling factor of 0.9 for the biomass B1 was obtained. The picture of the particles after the pyrolysis experiment in 900 ºC and with the drop-height of 17.5 cm is presented in Figure 7.27.

Figure 7.27. *Particles of B1a after pyrolysis experiment in 900 ºC, drop-height 17.5 cm.*

In Figure 7.27 the particles after the pyrolysis are nearly spherical. The difference is especially large if Figure 7.27 is compared to Figure 7.11. The shapes of highly elongated particles in Figure 7.11 seem to become more uniform and spherical but the minimum particle diameter increases, and thus the particle sphere equivalent diameter remains nearly constant. All the fuel batches after the experiments were not pictured due to lack of time but according to the images of two different drop-heights there seems to occur some periodic swelling during pyrolysis. However, a major inaccuracy may have occurred in the measurements of the particle diameter due to a low number of the pictures of the particles after the experiments. The swelling factor of the large particles of the biomass B1 was not obtained because the full pyrolysis conversion could not be achieved and there was not enough time to analyze all the particle sizes and shapes of all the experiments.

The biomass B2 had to be shipped from Asia, and therefore it arrived considerably later than the domestic biomass B1. The screw feeder used for B1 was found to be incapable for feeding the biomass B2 into the reactor, and therefore it had to be changed. The smallest size fraction of B2 was so sticky that it formed a layer on the surface of the thin screw feeder, and thus it had to be replaced with coarser one. However, with the coarser blade injecting single particles was more challenging, and therefore B2a dropped through the reactor as clusters of different sizes. The experimental results and standard deviations of the measurements of B2a, B2b and B2c are presented in Figure 7.28, Figure 7.29 and Figure 7.30, respectively.
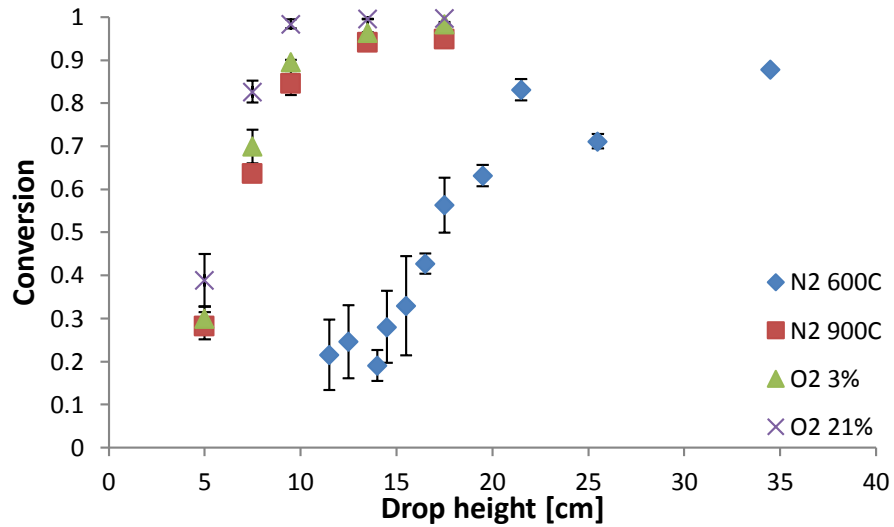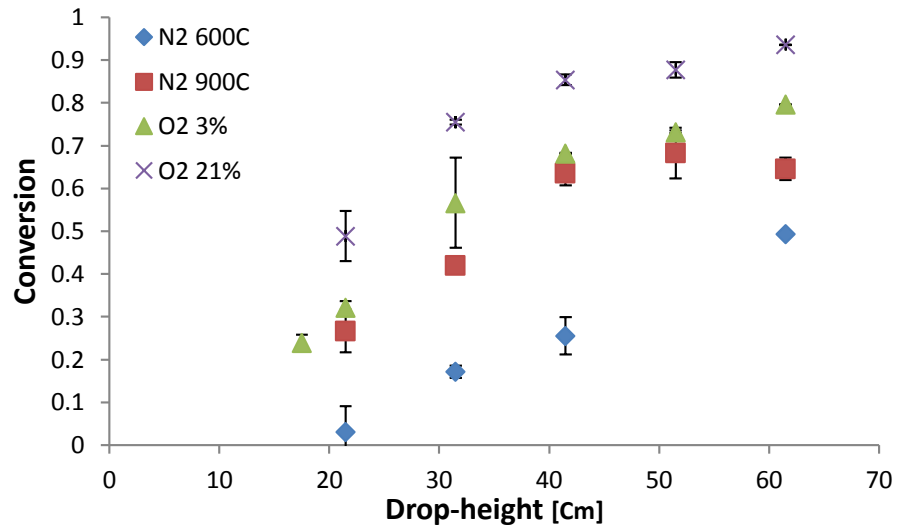
Figure 7.28. Measurements in DTR with B2a.
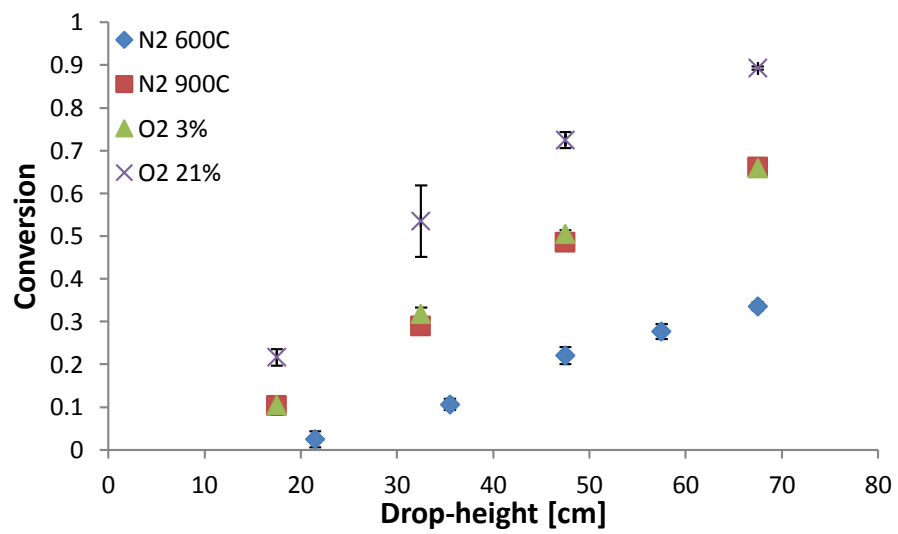
Figure 7.29. Measurements in DTR with B2b.
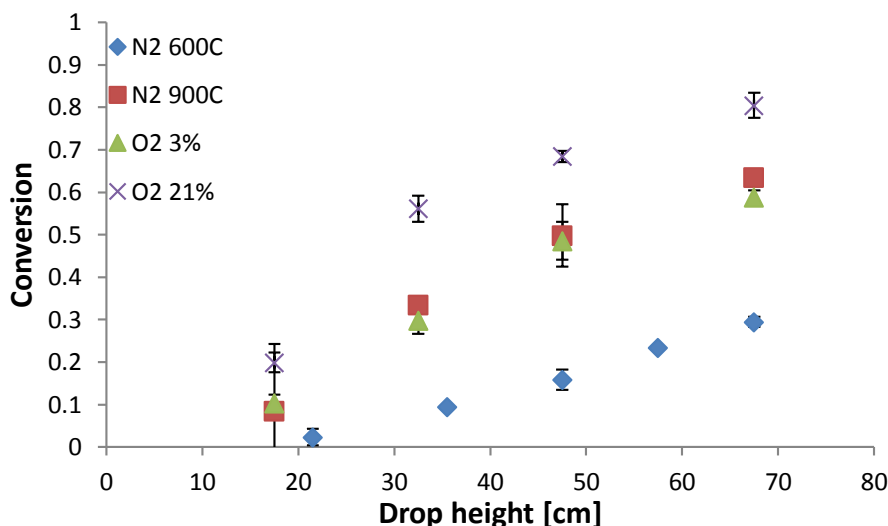
Figure 7.30. *Measurement in DTR with B2c.*

The smallest size fraction of B2 seems to be much less reactive than that of B1. At the same drop-height B1a had devolatilized completely but the conversion curve of B2a was just in the beginning. However, the mass mean diameter of B2a was several times larger than that of B1a, which can be seen in Figure 7.8 and Table 4. Thus, it is obvious that B2a has longer conversion time. Almost the full length of the reactor had to be used in order to obtain full pyrolysis conversion of B2a. According to Figure 7.28 the biomass B2 seems to have much less volatiles than B1. In Table 5 the difference was only 10 % in the amount of volatiles but it seems to be much more in high temperature pyrolysis. Even more interesting fact is that according to the proximate analysis the amount of volatiles is 73 % but in high temperature experiments with B2a the maximum pyrolysis conversion level was 68 %. The amount of volatiles was supposed to be higher in the DTR experiments than in proximate analysis due to higher heating rate. Thus, the combustion properties of B2a seem to differ from the average properties of the biomass B2 shown in Table 5.

On the contrary, the larger size fractions of biomass B2 seemed to be much more reactive than those of B1. Conversion of B2b and B2c was able to reach much higher conversion level than B1b and B1c. This could be caused by different fuel properties but most likely the particle shapes have a considerable effect on the conversion behavior as well. Highly elongated particles offer significantly more surface area, and thus the heat transfer to the particle is considerably higher than it is for less elongated particles of the biomass B1. In addition, the pyrolysis conversion curve seems to proceed much higher level than 73 % which is the amount of volatiles in Table 5 and it is clear that the amount of volatiles is higher for the larger size fraction of the biomass B2 than the average volatile yield. The effect of 3 % oxygen level on conversion curves of the larger particles is negligible for the biomass B2 as well as for the biomass B1 even though the elongated particle shape offers much more surface area for overlapping of the different

combustion phases. However, without experiments from higher drop-height it is impossible to say anything further of the shape of the conversion curve.

The swelling factor for the biomass B2 could not be obtained. The larger particles of B2 did not achieve the full pyrolysis conversion, and thus they were not imaged. The particles of B2a were partly imaged but according to the pictures the mass mean particle diameter increased considerably. The misleading swelling occurred probably due to the fact that different sizes of particles and particle clusters of B2a were dropped through the reactor. Thus, the largest particle clusters were over-emphasized in the images while the smallest particles may have been diminished. Due to the volume averaging the swelling coefficient was too high. Therefore, the swelling factor of the biomass B2 was agreed to be 0.9.

8. MODELING RESULTS AND DISCUSSION

The main goal of this thesis was to investigate if the already existing combustion sub-models in a CFD software Ansys Fluent are capable of representing the conversion process of solid biomass correctly by determining the reactivity parameters of the fuels. However, the whole solid fuel combustion modeling was originally developed to describe pulverized coal combustion and pulverized biomass combustion differs notably from that, as described in the previous chapters. At first the modeling results for the two biomasses are presented. After that there is a discussion on the results and some improvement suggestions.

8.1 Modeling results

The model output was fitted to match the experimental data as well as possible. Optimization tool used in this thesis was *fminsearch* function of Matlab, which was able to find effectively local minimums. However, the global minimums were in interest, and thus the optimization was constructed in a loop structure as described in the fifth chapter. The devolatilization parameters were optimized at first based on the experiments in pure nitrogen. After this, the char oxidation parameters were optimized. This procedure based on the assumption that pyrolysis and char oxidation are individual processes which do not affect each other. Based on the model assumption of consecutive combustion processes the phases of combustion were assumed to be individual as well.

The optimization routine had to be constrained in order to prevent the optimization routine to find unrealistic parameters with Kobayashi two-competing rate devolatilization model due to a large amount of optimizable variables. The optimization constraints were fuel specific for the most part, and they were set and validated mostly by eye. Thus, the model outputs were tried to keep as realistic as possible. However, even the constraints were not enough to steer the optimization routine towards the optimal solution and the initial values of the optimization affected the result as well. The total effect of constraints and the proper initial values was tuned individually for each fuel and for each size fraction in order to find applicable results. The same phenomenon was not observed with the single kinetic rate model and the optimization was much more straightforward with it. In optimization of the devolatilization parameters the model output in 900 ºC was weighed fourfold since that temperature is closer to the condition of the flame of an industrial burner. Both the pre-exponential factor and activation energy were constrained in order to keep the reactivity parameters realistic by comparing them to the ones in literature. [7-12]

The optimized model output of the single rate and Kobayashi models in N_2 atmosphere and the pyrolysis measurements in both 600 ºC and 900 ºC for B1a are presented in Figure 8.1. In the figure ten conversion curves representing the discretized particle size distribution are plotted along with the average conversion curves drawn in bold. In 600 ºC there are much less measurements in Figure 8.1 than in Figure 7.24 because the experimental data used in optimization was validated from a larger group in a way that the experiments covered the whole pyrolysis. According to the pyrolysis measurements in 900 ºC the volatile yield was determined as 95 % of dry basis. The amount of ash was set to 0.83 % according to proximate analysis (Table 5).
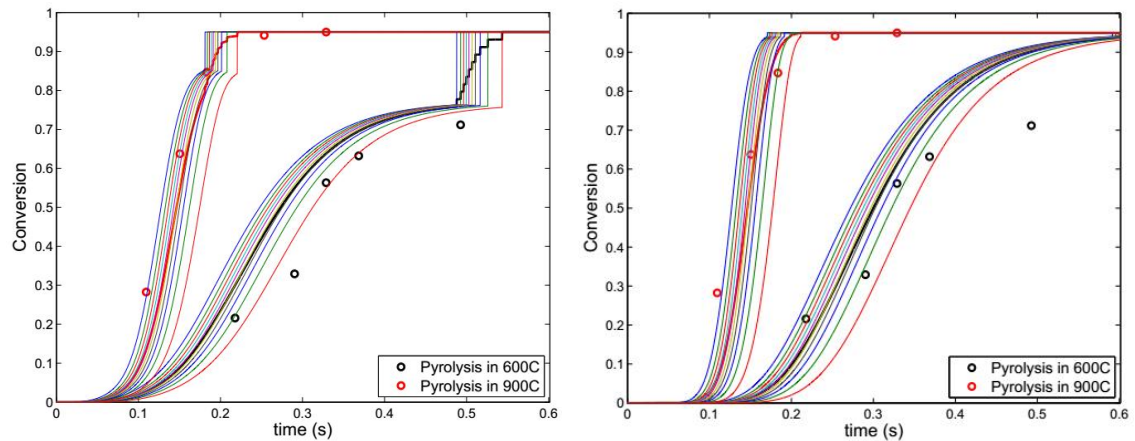
Figure 8.1. *Pyrolysis model results of B1a. On the left Kobayashi pyrolysis model and on the right single rate pyrolysis model.*

In Figure 8.1 differences between the different pyrolysis models can be seen clearly. It is clear that single reaction rate model predicts the same final volatile yield regardless of temperature if sufficient reaction time is given. However, the two-competing rates Kobayashi model has the same final pyrolysis conversion level due to the switching condition described in the fifth chapter. The single particle conversion curves of Kobayashi model include a clear stepping at the end of the conversion curve in 600 ºC near to the last experiment since the optimization was limited there. The model output in 900 ºC also contains large steps at the end of the single particle conversion curves but the step size decreases with decreasing particle size due to more aggressive temperature rising speed of the smaller particles. Thus, in higher temperatures the step size decreases even further.

Both models were able to describe the pyrolysis behavior reasonably well. The largest deviation between the measurements and model output occurred in the beginning of the conversion curve with both models. The lag before the first measurement can be tried to reduce e.g. by lowering the volatilization temperature or specific heat of the fuel. However, decreasing the devolatilization starting temperature from 400 K may not be wise because in the CFD simulations the fuel can start to react already in the channel before the burner. Decreasing specific heat of the fuel brings the single particle conversion

curves in Figure 8.1 closer to each other but the average conversion curves do not differ that much from those presented in after the optimization procedure. The minimized square sum remains the same even if the specific heat was decreased to 1300 J/kgK.

The Kobayashi model may have more realistic conversion curve shapes in the beginning of the pyrolysis due to two different sets of reactivity parameters for slow and fast pyrolysis. However, the pre-defined amount of volatiles eliminates the effect of temperature dependency of the pyrolysis yield by creating unrealistic steps at the end of the conversion curves in Figure 8.1. On the other hand, the single rate model describes the beginning of the conversion curve in 600 °C reasonably well and only the last measurement cannot be described with the model. Because the pyrolysis curves of different models were individual, the char oxidation parameters were tuned for both pyrolysis models separately as well. The model output for combined pyrolysis and char oxidation are presented for Kobayashi model and single reaction rate pyrolysis model in Figure 8.2.
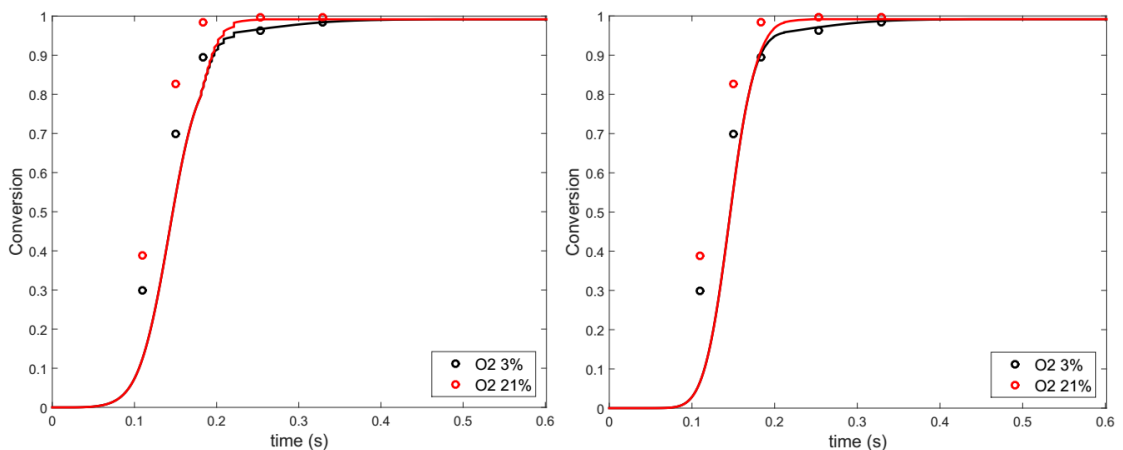
Figure 8.2. *Model results for combined pyrolysis and char oxidation of B1a. On the left Kobayashi pyrolysis model and on the right single rate pyrolysis model.*

Both models are able to describe char oxidation in the lower oxygen concentration moderately well. The difference is greatest between the first measurement and the model output at 5 cm of drop height. However, the difference was nearly as great in Figure 8.1 as well. In Figure 7.24 the measurements in 3 % oxygen and in pure nitrogen were close to each other.

Char oxidation in the higher oxygen concentration was not described as well as in the lower concentration. It is obvious that if the combustion phases are assumed to be consecutive and once 95 % of dry mass has evaporated in pyrolysis, char oxidation cannot change the shape of the total conversion curve dramatically. Thus, the conversion curves in 3 % and 21 % oxygen differ only after approx. 90 % of conversion level in Figure 8.2. However, as seen in Figure 7.24 the shape of the conversion curve starts to change already in the beginning of the curve when the oxygen concentration is 21 %.

Therefore, it is impossible to describe particle combustion with the assumption of consecutive combustion phases in high oxygen concentration. The problem was tried to solve by lowering the volatile yield and thus, enabling char oxidation to change the shape of conversion curve more. However, this procedure did not enhance the behavior in higher oxygen concentration and made the conversion behavior in pure nitrogen and in 3 % oxygen even worse.

The same kinetic parameters could not be used to describe the conversion process of the larger particles. The Kobayashi parameters optimized for the smaller particles predicted too aggressive mass loss speed of B1b and B1c due to increased particle size which affects the intra-particle heat and mass transfer. With the parameters optimized for B1a the single rate model does similarly with larger particles in 900 $^{\circ}$C but predicts too slow mass loss speed in 600 $^{\circ}$C. However, the Kobayashi model with parameters optimized for B1a could be used for larger particle sizes too if specific heat capacity of the particles was increased in order to restrict the particle heating and slow down the pyrolysis. However, this could lead to lower temperature after pyrolysis and thus, lower the char oxidation reactivity in the model. Therefore, individual reactivity parameters were optimized for B2b and B2c.

Model output and the measurements for particles of B1b are shown in Figure 8.3. Both models are able to predict the conversion behavior reasonably well in both temperature levels. Even though the single particle conversion curves differ from each other, the average conversion curves of both models are very similar in Figure 8.3. Kobayashi model provided slightly smaller sum of square error but in practice there is no difference between the pyrolysis model outputs for B1b.

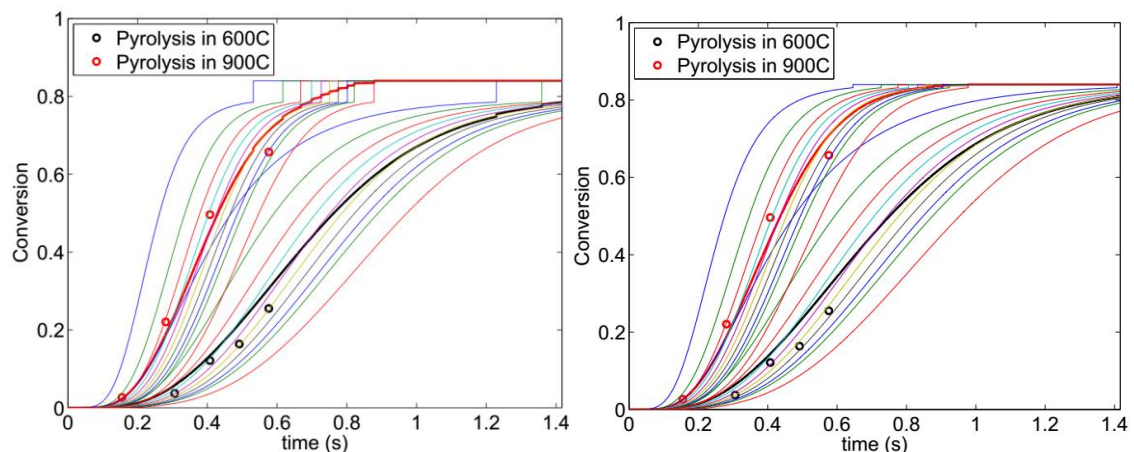*Figure 8.3. Pyrolysis model results for B1b. On the left Kobayashi pyrolysis model and on the right single rate pyrolysis model.*

Originally the same velocity profile was used for both B1b and B1c. However, according to CFD simulations of the particle combustion in the DTR the larger particles should have had notably higher final velocity, as mentioned in the sixth chapter. Thus,

the velocity profile for B1c was obtained from CFD. The reactivity parameters were optimized for B1c as well and the model outputs are presented in Figure 8.4.
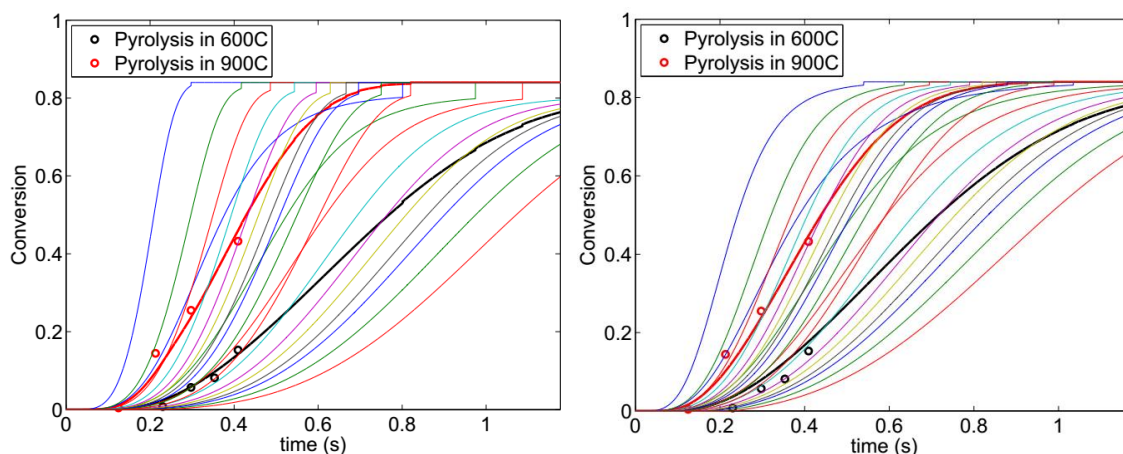
Figure 8.4. Pyrolysis model results for B1c. On the left Kobayashi pyrolysis model and on the right single rate pyrolysis model.

Both models seem to describe also the pyrolysis of the largest particles of biomass B1 well in Figure 8.5 and only little differences can be observed in the figure. According to Figure 8.3 and Figure 8.4 both B1b and B1c seem to achieve the full pyrolysis in the same time, e.g. both samples seem to reach full pyrolysis conversion in 900 ºC after approx. one second. However, B2c had traveled much further in that time due to the larger particle size, and thus higher final velocity. Varying the swelling factor made very little difference in the results. However, a slight decrease in square sum of pyrolysis was noticed due to increase in the swelling factor. Larger swelling factor makes the particle diameter to increase as a function of conversion which increases the particle heat transfer at the end of the conversion curve. The difference was still negligible, and thus the swelling factor was set to 0.9 which was the initial value for it in simulations.

It is worth of mentioning that B1a is the only sample of the biomass B1 the char oxidation parameters could be achieved for. The same char oxidation parameters may be used for larger particle as well. However, char oxidation of the larger particles is not probably the same due to larger amount of oxidizing matter (volatile matter of larger particles was 84 % and that of smaller particles was 95 %). Moreover, diffusion term in Equation 25 determines mostly the char oxidation rate of the larger particles. This causes very slow char oxidation in lower oxygen levels which leads to perhaps surrealistically long conversion times of the bigger particles. However, the largest fraction of the biomass conversion time includes char oxidation as mentioned in the fourth chapter.

The model output with the optimized kinetic parameters for the smallest size fraction of the biomass B2 is presented in Figure 8.5. The final conversion level of pyrolysis is notably lower than that of biomass B1 which could be seen clearly in the Figure 7.28.

The pyrolysis volatile yield was chosen according to measurements as the highest conversion level achieved (68 m-%).

Figure 8.5. *Pyrolysis model results for B2a. On the left Kobayashi pyrolysis model and on the right single rate pyrolysis model.*

There was more dispersion in the measurements of B2a than e.g. in those of B1a due to the fact that B2a dropped as different sizes of clusters and the cluster size in the different measurements was not constant. Thus, there is more uncertainty in the results. However, both models were able to describe the pyrolysis behavior of B2a relatively well and the average conversion curve is very similar with both models. Only the single particle size conversion curves of the models differ from each other. The ending of the conversion curves of the single particle size affects the start of char oxidation, and thus the char oxidation of both models in Figure 8.6 is different.
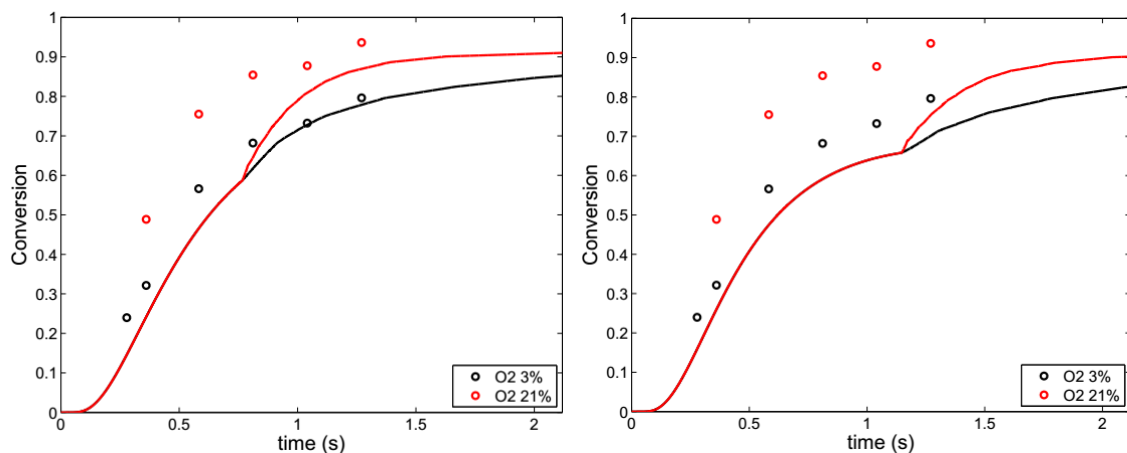
Figure 8.6. *Model results for combined pyrolysis and char oxidation for B2a. On the left Kobayashi pyrolysis model and on the right single rate pyrolysis model.*

Both models are able to describe the char oxidation process rather poorly. However, because the single particle pyrolysis curves of Kobayashi model achieve the final conversion level notably earlier than those of the single-rate model, the char oxidation starts sooner as well. Thus, char oxidation can be described better with Kobayashi than with

the single-rate model. B2a included a relatively large number of very small particles (see Figure 7.11) which started to oxidize changing the shape of char oxidation curve yet in the first measurements in Figure 8.6.

The model outputs for pyrolysis of the particles of B2b are presented in Figure 8.7. Both models gave similar outputs for the pyrolysis curves and there were no notable differences in single particle conversion curves either.

Figure 8.7. *Pyrolysis model results for B2b. On the left Kobayashi pyrolysis model and on the right single rate pyrolysis model.*

In Figure 8.8 the model outputs for B2c are presented. Similarly, to B2b, there are no notable differences between the models. The conversion curves of B2b and B2c are alike in many ways due to the relatively same size distribution (see Figure 7.8). Both B2b and B2c seem to contain relatively wide size distribution due to incapability of the particle sizes and shapes identifying software to recognize highly curved particles. The particles of B2c still had the widest size distribution and thus, discretization of the size distribution into ten size fractions is rather coarse. Due to the wide discretized size distribution the single particle conversion curves rise very sharply in Figure 8.8.
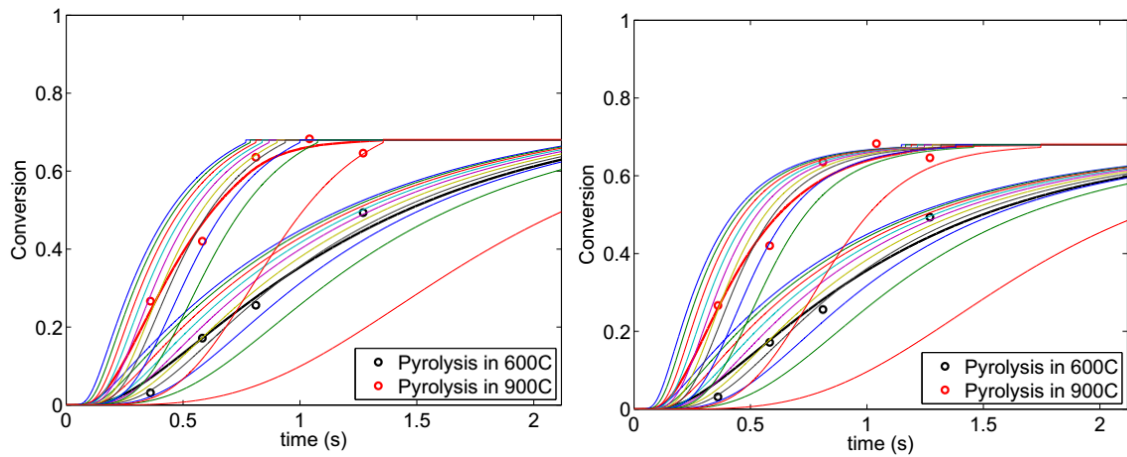

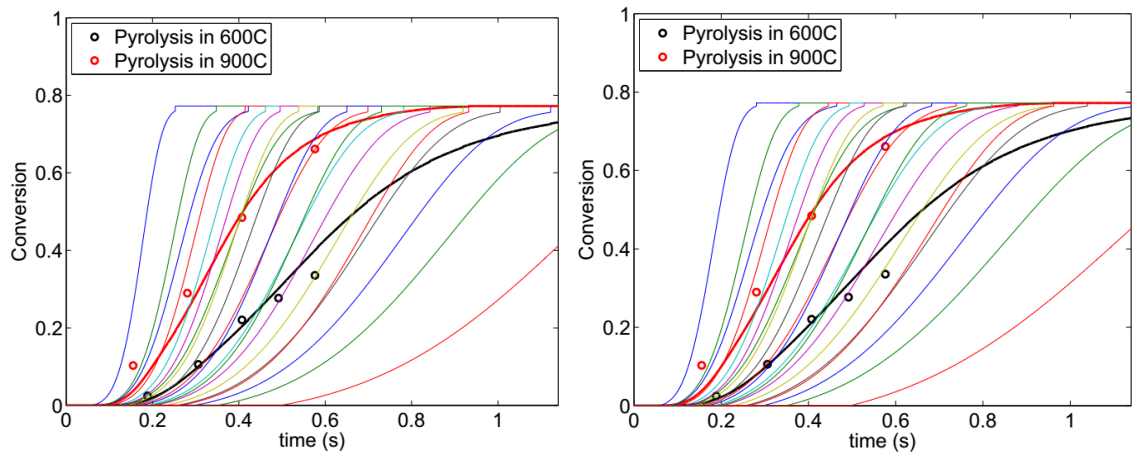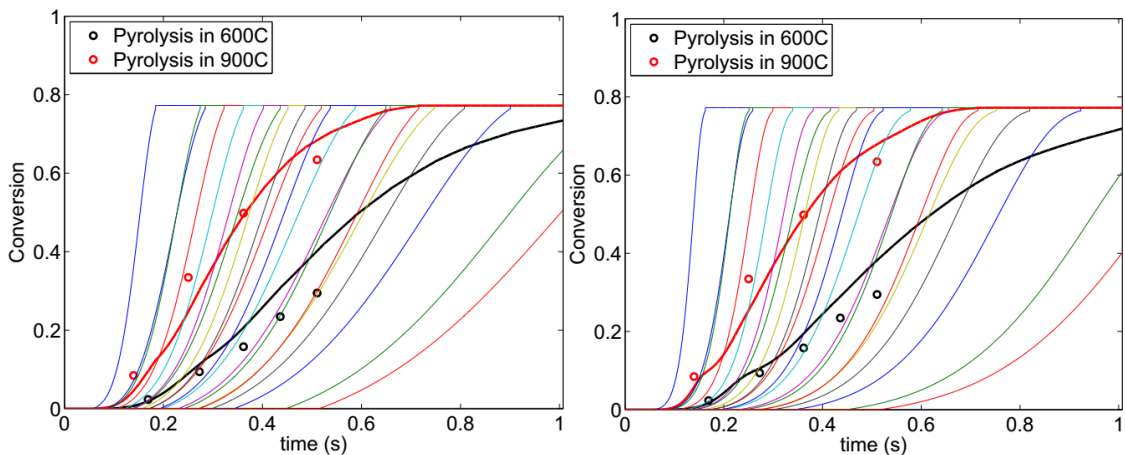***Figure 8.8.*** *Pyrolysis model results for B2c. On the left Kobayashi pyrolysis model and on the right single rate pyrolysis model.*

The kinetic parameters for pyrolysis of different models and biomass batches are presented in Table 9. Once again, it should be noted that the Kobayashi parameters were highly dependent on the optimization constraints. The Kobayashi model constraints were individually tuned for small and larger particle sizes. For the pre-exponential factor, the lower limit was 300 and the higher limit was 300 000. The lower and higher limits for exponential factor were 30 000 and 200 000, respectively. These constraints were used for parameter optimization of all the biomass samples. However, yield factors had to be tuned more individually. The low limits of the yield factors for slow and fast pyrolysis α_1 and α_2, respectively, were set for B1a to 0.5 and 0.9, respectively. However, with B2a the low limits for slow and fast pyrolysis were 0.7 and 0.8, respectively. For the larger particles of biomass B1 and B2, the values of 0.8 and 0.9 were used as the low limits of yield factors for slow and fast pyrolysis, respectively.

The optimized parameters of Kobayashi model for different size fractions differ quite much from each other. This is a result of lack of measurements. If there had been measurements from higher drop-heights the results would have been more accurate. Now the predictions of the shape of the conversion curve are just guesses and there is no knowledge of how the results will extrapolate further.

Table 9. *Optimized parameters for Kobayashi and single-rate pyrolysis models. The first six parameters are for Kobayashi model and the last two are for single-rate model.*

Fuel	A_1	A_2	E_1	E_2	α_1	α_2	A	E
B1a	1.00E2	4.97E5	2.08E4	7.76E4	0.59	1.0	2.99E6	8.87E4
B1b	3.05E2	3.79E2	3.00E4	1.97E5	0.80	0.97	1.54E2	2.64E4
B1c	4.67E2	3.00E5	3.00E4	8.83E4	0.80	0.97	1.30E2	2.25E4
B2a	3.00E2	3.47E3	4.07E4	1.99E5	0.77	0.99	1.77E2	3.55E4
B2b	1.64E3	1.66E3	3.00E4	3.40E4	0.80	0.90	1.18E3	2.69E4
B2c	8.57E2	6.16E3	3.08E4	3.14E4	0.80	0.90	3.45E5	4.73E4

In the optimization of the char oxidation parameters the lower limit for the exponential factor E_r of char oxidation in Equation 24 was determined as 60 000 in order to prevent the char oxidation to occur in too low temperatures. The value for diffusion constant $C_1 = 5e^{-12} s/K^{0.75}$ is used in Equation 24 as mentioned earlier. The char oxidation parameters are presented in Table 10. The parameters for the same fuel with the different pyrolysis model differ notably. Thus, the pyrolysis and char oxidation parameters are coupled and should be used only with the appropriate model, i.e. the char oxidation

parameters obtained with the single reaction rate pyrolysis model should be used only with the single rate model.

Table 10. *Optimized char oxidation parameters for Equation 24 with Kobayashi and single rate pyrolysis models.*

Fuel	C_2 (Kobayashi)	E_r (Kobayashi)	C_2 (single rate)	E_r (single rate)
B1a	1.70E-3	6.00E4	2.05E-3	6.00E4
B2a	2.00E10	6.01E4	2.21E+11	6.11E4

The modeled conversion curves could be tuned to match the experimental data rather well, at least pyrolysis was presented reasonably well. However, in the validation of the model and the model parameters one has to remember that the results had to be extrapolated to higher temperatures as well. Thus, an additional 500 ºC was added to the temperature profiles, both wall and gas temperatures, in order to test the model behavior in the higher temperatures which are closer to the peak temperatures of an industrial boiler. The conversion behavior of B1a is presented in Figure 8.9 when the gas and wall temperatures are 1100 C and 1400 C. Both models extrapolate similarly to higher temperature levels and the combustion process is described similarly in higher temperatures as well. The model predicted the same behavior with B1b but with B1c the Kobayashi model predicted faster conversion response in higher temperatures than the single-rate model. This is obvious since according to experiments only the beginning of the conversion curve could be fitted by the model output. The rest of the curve is just a guess.
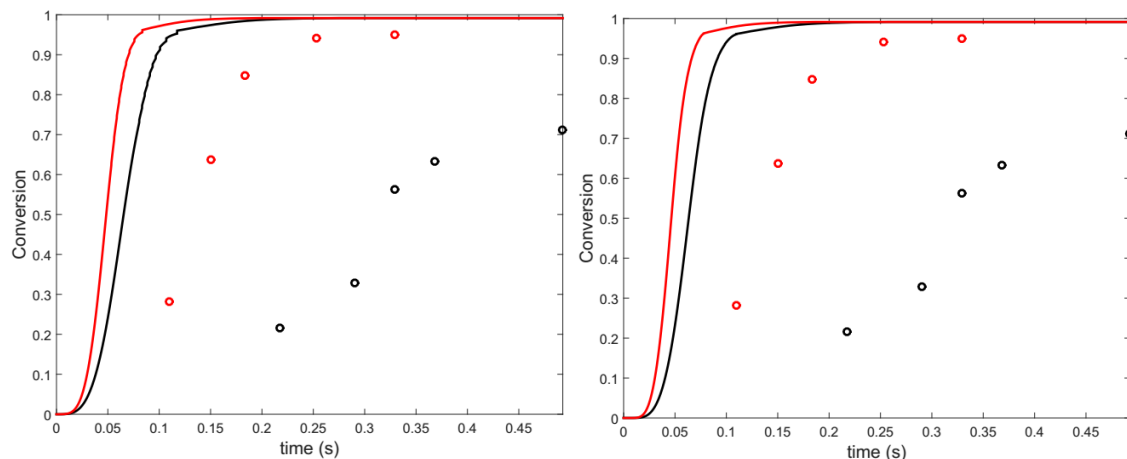

Figure 8.9. *Model outputs in 1100 ºC and 1400 ºC in 3 % oxygen with the pyrolysis experiments. Kobayashi pyrolysis model on the left and single-rate model on the right.*

Even though both models described the conversion process rather similarly in higher temperatures as well, there are no measurements from these temperatures, and therefore

it is impossible to say anything how well the high temperature devolatilization is described.

The reactivity parameters obtained by optimization were also used in CFD simulations with Fluent. The simulations in DTR were conducted by the other thesis worker in this project, M.Sc. Niko Niemelä. The results of the CFD simulations were very promising and Fluent was predicting the conversion process in the DTR similarly as the model programmed with Matlab. [78] Thus, the results of this thesis were successful and the parameters were applicable for the direct CFD simulations.

8.2   Discussion on the results

Even though the models were able to predict the conversion process of all biomass samples relatively well there are multiple sources of error in the experiments. The conditions in DTR were not the same in different experiments and many mistakes were done during them which caused deviation to the results. Assumptions used in modeling were also highly arguable and the solid fuel combustion modeling procedure that may be valid for pulverized coal combustion is problematic for pulverized biomass combustion. Also the modeling could be conducted differently in order to improve the suitability of the results for CFD modeling.

The wall temperature profile of the DTR was obtained from the eight wall temperature measurements. With the low drop heights, the particle feeding probe could extend lower than the lowest wall temperature measurement was located. The lowest wall measurement was at the height of 11.5 cm from the bottom of the reactor and thus, the wall temperature profile at the lowest drop heights was mainly guessed. It was noticed that the thermocouple tended to read more the wall temperature than the gas temperature. Therefore, the readings of the thermoelement could have been used to approximate the local wall temperatures at the end of the reactor. It was possible that the reactor was heated excessively at low drop heights, and therefore particles experienced more aggressive temperature rising speed in the experiments of lower drop heights than in the higher ones. Analyzing the thermocouple readings more accurately showed that the temperature rising speed at lower drop heights was notably higher than those at higher drop heights which affected the first two measurements in Figure 8.1and Figure 8.2.

The averaging of the analytical formula used in describing the wall temperature profile of the DTR to speed up the calculation skewed the results. It is worth noting that the thermal profile of the gas in the DTR is calculated by using CFD and it is far from being isothermal. The gas temperature profile also depends on the position of the particle injection probe, and therefore the averaging produces error in the modeling. In the future experiments the thermocouple and wall temperature measurements should be plotted in the same picture and the reactor should be adjusted in a way that the temperature profiles match the previous measurements. Thus, the particle temperature histories could be

more comparable between the experiments with different drop heights. Also the individual temperature profiles of the reactor of different drop-heights could have been used in the optimization routine even though it would have reduced the calculation speed and made the illustrative presentation of the results harder.

One the greatest errors in the results occurred due to incapability of the particle analysis software to present large and non-uniform particles as whole particles. Thus, the smallest size fraction was over-emphasized at the expense of the larger particles with the particles of B1b and B1c which made the results more inaccurate. The software identified less large particles, and thus the size distribution of B1b and B1c was incorrect. In addition, the particle aspect ratio was calculated by using the particle amount and it is not determined mass based. Therefore, the sphere-equivalent Rosin-Rammler size distribution in Figure 7.10 could be inaccurate. Also, in order to obtain accurate sphere-equivalent size distribution of the particles, the individual aspects ratios for different size fractions should be used. This could make the Rosin-Rammler fitting more difficult and it is possible that the obtained size distribution cannot be described with the Rosin-Rammler equation. However, Rosin-Rammler size distribution is not necessarily needed in CFD simulations with Fluent.

The particles of biomass B2 were found to be extremely problematic for the particle identification setup as well as for the experimental setup. The smallest size fraction of biomass B2 dropped as clusters and the particle injecting procedure was not the same when injecting them into the reactor and on the light diffuser plate. Thus, the cluster size may have varied and the results could be highly uncertain. The larger particles of biomass B2 on the other hand were curved and highly elongated which made the particle analyzing software to cut them in pieces. Therefore, the sizes of the particles of B2b and B2c presented in Figure 7.12 could be multiple times smaller than in reality. In Table 4 the aspect ratios of the particles of B2b and B2c rather similar to those of the particles of B1b and B1c which cannot be true according to Figure 7.11. Thus, the particle identification software should be improved in order to enhance the identification of irregular, fuzzy and highly curved particles.

The particle size distribution was discretized rather coarsely. Thus, it would have been interesting to see if thinner discretization had changed the results. Especially with the fuel samples with wide size distribution, e.g. B2a, B2b and B2c, a thinner discretization could have affected the results. However, the particle identification was inaccurate, and thus the size distribution was already more or less false.

Velocities of the particles were measured only in 600 ºC for the small particles of biomasses B1 and B2. However, the velocity profile obtained in 600 ºC may not be valid in 900 ºC due to higher mass loss of the particles. This may have affected the char oxidation parameters as well as the pyrolysis parameters. Thus, the particle velocity measurements should have been conducted also in higher temperatures in order to model the

particle residence time in the reactor more accurately. In addition, the particle velocity was obtained by taking average of all the velocity measurements and the particle size was not taken into consideration. Thus, the velocity of the smallest size fraction is over-emphasized due to a larger amount of smaller particles in the pictures. In addition, all sizes of particles of the same particle size group, e.g. B1a, were assumed to travel in the DTR with the same velocity which could be misleading. The velocities of the different sizes of particles should be taken into account in order to model the particle conversion process more accurately. Mass averaging the particle velocities or dividing the particle velocities into the velocities of different sizes of particles may be beneficial for the future.

The velocity profile for the largest size fraction of biomass B1 was obtained by CFD calculations. However, this was the only one the velocity profile was obtained that way. The fitted velocity profile and the profile from CFD calculations of the particles of B1b differed notably, and thus using the CFD velocity profile for only B1c is doubtful. The particles of different sizes of biomass B1 were rather evenly shaped, and therefore the velocity profile should have determined only for the smallest size fraction of B1 for which the amount of pictures in the velocity measurements was the highest. The velocity data of B1a should have been used in determining the shape factor for Fluent simulations and then the same shape factor could be used for larger particles to determine the velocity profile for them with CFD. CFD could be used as well in determining the particle velocity profile in 900 ºC.

Specific heat capacities of the fuels were approximated and not determined accurately. Thus, the accurate temperature history of the particles was not possible to obtain. The particle temperatures are modeled but they are dependent on the chosen specific heats, and therefore reactivity parameters only compensate their effect on conversion curve. Also the specific heat of the fuel is assumed to remain constant during the whole conversion process by Fluent even though the virgin biomass and the char coal have very different specific heats. Thus, in the future creating a user defined function in Fluent which ables the specific heat to change according to conversion could be useful.

One of the greatest disadvantages of the pyrolysis models used by Fluent is the pre-determined volatile yield. Even though Kobayashi two-competing rate model which is developed for modeling varying volatile yield could be used, the pre-determined volatile yield has to be reached in every condition. Both models suffered from this and therefore, their model outputs were quite similar. The single rate model is computationally less heavy model due to the smaller amount of variables, and thus there is nothing requiring the use of heavier Kobayashi model in this case.

An assumption of consecutive combustion processes could be valid for very small particles but it produces error in modeling the conversion process of larger particles. The 21 % oxygen concentration was clearly too high for the model being able to describe the

combustion. However, according to the measurements there was no notable difference between the pyrolysis experiments and combustion experiments in low oxygen concentration up to 60 % conversion. Thus, it is essential to conduct the combustion experiments also in the highest oxygen concentration that can exist in the real world applications, e.g. 10 % of oxygen. If the differences between the pyrolysis and combustion experiments were as negligible in 10 % oxygen as they were in 3 % oxygen, using the assumption of consecutive combustion phases would be justified. If the differences were significant with 10 % of oxygen, a user defined method allowing pyrolysis and char oxidation to occur simultaneously could enhance the modeling accuracy. It was little surprising that the biggest differences between the pyrolysis and low oxygen combustion experiments were observed with the smallest size fractions of both biomasses (Figure 7.24 and Figure 7.28). However, this phenomenon could be related to measurement accuracy and the coarse discretization of the size distributions.

Particle shapes have not been taken into consideration in heat transfer modeling, and thus the effect of heat transfer between the particles and the surroundings in the reactor is under estimated. Especially for the larger particles of the biomass B2 the assumption of spherical particles is extremely misleading. Fluent uses the shape factor to represent the drag force of the aspherical particle and thus, the shape factor could be used in enhancing the particle heat transfer area. Once again, reduced heat transfer is compensated by the reactivity parameters but the modeled particle heating could be notably less than in reality. The reactivity parameters are not only fuel dependent but they depend on the particle shapes as well because the parameters are compensating the effect of particle shapes on the particle conversion time. Thus, the same parameters would not be valid for the same fuel prepared with different milling system if the particle shape was not the same.

In order to determine the conversion behavior of the large particles accurately, the longer drop tube reactor is required. In this thesis the shape of the end of the conversion curve is mainly guessed and the char oxidation parameters could not be obtained for the larger particles of both fuels. Thus, the particle residence time in the heated reactor should be high enough in order to achieve full or almost full conversion level.

In conclusion many things could have been done better in the measurements. In the future, more concentration on the temperature tuning of the reactor during the experiments should be focused. Also major improvements on the particle identification software are needed in order to identify the larger particles properly. Various improvements are needed for the modeling setup as well. However, many of the improvements needed for modeling could be solved by conducting the modeling with Fluent and only the optimization of the parameters with Matlab. The particle modeling with Fluent is very fast because the particle stream does not affect the flow field in the reactor and they can be solved separately. Thus, the switching conditions of the sub-models would be automatically correct, and the particle motion, heat exchange and reaction modeling would be

exactly the same. The velocities of the different sizes of particles would be also taken into account by Fluent. Moreover, the transition to the total Fluent modeling would be smooth because the gas temperature and the particle velocity profiles are already at least partly modeled with Fluent. This would also make the modeling more consistent because in this thesis a part of the particle velocities was obtained from the measurements while the other part was modeled with Fluent.

Even though many rather coarse assumptions were made in the modeling and the experiments were not as accurate as they could have been, the modeling results were mainly successful. Despite the model being coarse, the conversion process of both fuels were able to be described with it relatively well. Thus, the solid fuel combustion model of Fluent can be used in pulverized biomass combustion if the reactivity parameters are achieved with a model using the same assumptions and modeling procedure as Fluent uses.

9. CONCLUSIONS

Limited supply of fossil fuels and global warming have forced to search for alternative fuels replacing fossil fuels, and biomass has proven to be one promising alternative. Using biomass in energy production has many other benefits than just decreased greenhouse gas emissions, such as reducing acid emissions and providing local employment. However, increasing the use of biomass in energy production requires careful planning and development. Even though biomass can be basically used in the pulverized coal firing boilers, biomass differs greatly from coal. Biomass combustion and slagging properties should be acknowledged and taken into account already in planning to start using or increasing the share of biomass in the boilers.

Computational Fluid Dynamics (CFD) has become one significant tool in designing different combustion processes, and thus it can be used in designing new biomass boilers or adapting the existing ones for new fuels, e.g. biomass. Specific information of combustion properties of the fuel is needed in order to predict the conversion process correctly. The combustion properties, i.e. reactivity parameters, are dependent on the used fuel, model and even particle size, and if specific information of those is not available the reactivity parameters have to be determined experimentally. The particle size distribution of the fuel is also needed in order to conduct the CFD simulations correctly.

Ansys Fluent is popular CFD software and it has several particle combustion models already programmed. Thus, using the tools existing in CFD programs in simulation of biomass firing would be highly straightforward and cost-efficient. However, Fluent uses several assumption and simplifications in modeling solid fuel combustion which may be valid for pulverized coal firing but not necessarily for pulverized biomass firing. Thus, the main objective of this thesis was to investigate how the solid fuel combustion modeling of Fluent is able to describe the conversion process of biomass by creating a model which describes the conversion process of a solid fuel particle similar to Fluent. Optimizing the reactivity parameters for two biomass fuels with the model revealed how well the particle combustion can be described.

The literature part of this thesis cover the use of biomass in energy production, properties of biomass and the solid fuel combustion, concerning especially biomass. In the fifth chapter solid fuel combustion is expressed, and the modeling procedure used in this thesis is presented. The modeling of the particle combustion process is trying to imitate the combustion modeling in a CFD code Ansys Fluent as well as possible. Help of Ansys product support is used to discover all the boundary conditions of the models

that are not described in Ansys Fluent Theory Guide. All the assumptions and conditions made in modeling are presented in the end of the fifth chapter.

In the sixth chapter the experimental setup is introduced. The first part of the experimental part was the analysis of the solid fuel particles in order to obtain the specific size and shape information of the fuels. Two different biomass fuels were examined and the details of the particle shapes and sizes are presented in the seventh chapter. In addition to the particle analysis, the industrial partner of this thesis project, Valmet Oy, was interested in examining how the grinding process of the pelletized fuel affects the particle size and shape. Thus, in the beginning of the seventh chapter comparison between two different grinders is presented. Also the size distribution of the grinder used by Valmet in its solutions is presented.

The experiments with a drop tube reactor (DTR) in the laboratory of Tampere University of Technology were the main part of the experimental section and they form the other part of the seventh chapter. The experiments were conducted with three different size groups of both fuels in order to present the whole size distribution of the ground fuel particles. The experiments were successful and they formed a good basis for the optimization of the reactivity parameters.

The optimization of the reactivity parameters was conducted by fitting the model output to match the experimental data. The fitting was mainly successful but limitedness of the modeling reduced the accuracy of modeling the combustion in high oxygen concentration. The results and obtained reactivity parameters are presented in the eighth chapter. The reactivity parameters should be directly suitable for CFD simulations with Fluent because the modeling was imitating the Fluent combustion modeling. CFD simulations with Fluent confirmed the suitability of the results for the direct use of the parameters.

TABLE OF REFERENCES

[1]   Key World Energy Statistics, International Energy Agency, 2015, 77 p. Available:
http://www.iea.org/publications/freepublications/publication/KeyWorld_Statistics_2015.pdf

[2]   BP Statistical Review of World Energy June 2015, 44 p. Available:
http://www.bp.com/content/dam/bp/pdf/Energy-economics/statistical-review-2015/bp-statistical-review-of-world-energy-2015-full-report.pdf

[3]   R. Raiko, J. Saastamoinen, M. Hupa, I. Kurki-Suonio, Poltto ja palaminen, 2nd edition, International Flame Research Foundation – Suomen kansallinen osasto, 2002, p. 60.

[4]   P. Grammelis, Solid Biofuels For Energy, Springer-Verlag London Ltd, 2011, pp. 43-67.

[5]   P. Grammelis, Solid Biofuels For Energy, Springer-Verlag London Ltd, 2011, p. 203.

[6]   T. Li, L. Wang, X. Ku, B. Guell, T. Lovås, C. Shaddix, Experimental and Modeling Study of the Effect of Torrefaction on the Rapid Devolatilization of Biomass, Energy & Fuels, 2015, pp. 4328-4338. Available:
http://pubs.acs.org/doi/pdf/10.1021/acs.energyfuels.5b00348

[7]   B.M. Wegenaar, W. Prins, W.P.M Swaaij, Flash Pyrolysis Kinetics of Pine Wood, Fuel Processing Technology 36, 1993, pp. 291-298. Available:
http://doc.utwente.nl/57393/1/Wagenaar93flash.pdf

[8]   J. Li, G. Bonvicini, L. Tognotti, W. Yang, W. Blasiak, High-temperature rapid devolatilization of biomasses with varying degrees of torrefaction, Fuel 122, 2014, pp. 261-269. Available:
http://www.sciencedirect.com/science/article/pii/S0016236114000155/pdfft?md5=2f1765deb6fc44cab10e9380ebb6f1e3&pid=1-s2.0-S0016236114000155-main.pdf

[9]   S. Jimenez, P. Remacha, J.C. Ballesteros, A. Gimenez, J. Ballester, Kinetics of devolatilization and oxidation of a pulverized biomass in an entrained flow reactor under realistic combustion conditions, Combustion and Flame 152, 2008, pp. 588-603. Available:
http://www.sciencedirect.com/science/article/pii/S0010218007002891/pdfft?md5=914615d9c67b9906adea45b6a37cea4b&pid=1-s2.0-S0010218007002891-main.pdf

[10]   C. Di Blasi, C. Branca, Kinetics of Primary Product Formation from Wood Py-
        rolysis, Industrial & Engineering Chemistry 40, 2001, pp. 5547-5556. Available:
        http://pubs.acs.org/doi/pdf/10.1021/ie000997e

[11]   O. Senneca, Kinetics of pyrolysis, combustion and gasification of three biomass
        fuels, Fuel Processing Technology 88, 2007, pp. 87-97. Available:
        http://www.sciencedirect.com/science/article/pii/S0378382006001378/pdfft?md
        5=e7ec24d0029c4925d153d3317f1415b5&pid=1-s2.0-S0378382006001378-
        main.pdf

[12]   H. Tolvanen, L. Kokko, R. Raiko, Fast pyrolysis of coal, peat and torrefied
        wood: Mass loss study with a drop-tube reactor, particle analysis, and kinetics
        modeling, Fuel 111, 2013, pp. 148-156. Available:
        http://www.sciencedirect.com/science/article/pii/S0016236113003165

[13]   Technology Roadmap - Bioenergy for Heat and Power, International Energy
        Agency, 2012, pp. 10-19. Available:
        http://www.iea.org/publications/freepublications/publication/2012_Bioenergy_R
        oadmap_2nd_Edition_WEB.pdf

[14]   Pulverised coal combustion (PCC), International Energy Agency Clean Coal
        Center. Available: http://www.iea-coal.org.uk/site/2010/database-
        section/ccts/pulverised-coal-combustion-pcc?

[15]   P. Basu, Biomass Gasification, Pyrolysis and Torrefaction, Practical Design and
        Theory, 2nd Edition, Elsevier, 2013, pp. 353-368.

[16]   M. Flyktman, J. Kärki, M. Hurskainen, S. Helynen, K. Sipilä, Kivihiilen kor-
        vaaminen biomassoilla yhteistuotannon pölypolttokattiloissa, VTT tiedotteita
        2595, 2011, 26 p. Available:
        https://www.tem.fi/files/31233/Kivihiilen_korvaaminen_biomassoilla_yhteistuot
        annon_polyvpolttokattiloissa_VTT_tiedotteita_2595.pdf

[17]   International Energy Agency, Database of biomass cofiring initiatives, Availa-
        ble: http://www.ieabcc.nl/database/cofiring.php

[18]   P.C.A. Bergman, A.R. Boersma, R.W.R. Zwart, J.H.A. Kiel, Torrefaction for
        biomass co-firing in existing coal-fired power stations, Energy research Center
        of the Neatherlands (ECN), 2005, pp. 11-20. Available:
        http://www.ecn.nl/docs/library/report/2005/c05013.pdf

[19]   J. Saastamoinen, M. Aho, A. Moilanen, L. H. Sörensen, S. Clausen, M. Berg,
        Burnout of pulverized biomass particles in large scale boiler – Single particle

model approach, Biomass and Bioenergy 34, 2010, pp. 728-736. Available: http://www.sciencedirect.com/science/article/pii/S0961953410000164

[20]   H.J. Veringa, Advanced techniques for generation of energy from biomass and waste, Energy research Centre of the Netherlands, 24 p. Available: https://www.ecn.nl/fileadmin/ecn/units/bio/Overig/pdf/Biomassa_voordelen.pdf

[21]   T. Joronen, T. Heinonen, Pulverized Pellet-fired Heat Plant for Rapid Load Control of CHP Networks, Power-Gen 2013, 9 p. Available: http://pennwell.sds06.websds.net//2013/vienna/rewe/papers/T2S6O2-paper.pdf

[22]   Bioenergy Project Development & Biomass Supply, International Energy Agency, Goor Practisce Guidelines, 2007, pp. 22-53. Available: https://www.iea.org/publications/freepublications/publication/biomass.pdf

[23]   P. McKendry, Energy production form biomass (part 1): overview of biomass, Bioresource Technology 83, 2002, pp. 37-46. Available: http://faculty.washington.edu/stevehar/Biomass-Overview.pdf

[24]   L. Zhang, C. Xu, P. Champagne, Overview of recent advances in thermo-chemical conversion of biomass, Energy Conversion and Management 51, 2010, pp. 969-982. Available: http://www.sciencedirect.com/science/article/pii/S0196890409004889

[25]   Revised 1996 IPCC Guidelines for National Greenhouse Gas Inventories, Wordbook, volume 2, 22 p. Available: http://www.ipcc-nggip.iges.or.jp/public/gl/guidelin/ch1wb1.pdf

[26]   R. Raiko, J. Saastamoinen, M. Hupa, I. Kurki-Suonio, Poltto ja palaminen, 2nd edition, International Flame Research Foundation – Suomen kansallinen osasto, 2002, pp. 186-216.

[27]   R. Raiko, J. Saastamoinen, M. Hupa, I. Kurki-Suonio, Poltto ja palaminen, 2nd edition, International Flame Research Foundation – Suomen kansallinen osasto, 2002, pp. 269-287.

[28]   P. Basu, Biomass Gasification, Pyrolysis and Torrefaction, Practical Design and Theory, 2nd Edition, Elsevier, 2013, pp. 87-120.

[29]   P. Jukola, M. Huttunen, CFD simulation of biofuel and coal co-combustion in a pulverized coal fired furnace, VTT Technical Research Centre of Finland, Finnish – Swedish Flame Days 2013, 9 p. Available: http://www.ffrc.fi/FlameDays_2013/Papers/Jukola1.pdf

[30]   Renewable energy in the EU – Share of renewables in energy consumption up to 15% in the EU in 2013, Eurostat newsrelease, 2015, 4 p. Avalable: http://ec.europa.eu/eurostat/documents/2995521/6734513/8-10032015-AP-EN.pdf/3a8c018d-3d9f-4f1d-95ad-832ed3a20a6b

[31]   E. Alakangas, EUBIONET III – Classification of biomass origin in European solid biofuel standard, Available: standardspro-posals.bsigroup.com/Home/getPDF/757

[32]   P. Basu, Biomass Gasification, Pyrolysis and Torrefaction, Practical Design and Theory, 2nd Edition, Elsevier, 2013, pp. 47-80.

[33]   Structure of wood, Wood Handbook – Wood as an Engineering Material, U.S. Department of Agriculture, Forest Service, Forest Products Laboratory, 2000, 463 p. Available: http://www.fpl.fs.fed.us/documnts/fplgtr/fpl_gtr190.pdf

[34]   M. Ek, G. Gellerstedt, G. Henriksson, Paper Chemistry and Technology, Walter de Gruyter, 2010, p. 16-17.

[35]   S. Mani, S. Sokhansanj, X. Bi, A. Turhollow, Economics of producing fuel pellets from biomass, Applied Engineering in Agriculture 22, 2006, pp. 421-426. Available: http://www.researchgate.net/publication/236999846_Economics_of_producing_fuel_pellets_from_biomass

[36]   S. Döring, Power from Pellets, Springer-Verlag Berlin Heidelberg, 2013, pp. 99-102.

[37]   S. Döring, Power from Pellets, Springer-Verlag Berlin Heidelberg, 2013, pp. 13-19.

[38]   R. Raiko, J. Saastamoinen, M. Hupa, I. Kurki-Suonio, Poltto ja palaminen, 2nd edition, International Flame Research Foundation – Suomen kansallinen osasto, 2002, pp. 131-137.

[39]   P. Grammelis, Solid Biofuels For Energy, Springer-Verlag London Ltd, 2011, p. 130.

[40]   T. Keipi, H. Tolvanen, L. Kokko, R. Raiko, The effect of torrefaction on the chorine content and heating value of eight woody biomass samples, Biomass and Bioenergy 66, 2014, pp. 232-239. Available: http://www.sciencedirect.com/science/journal/09619534

[41]   L. Kokko, H. Tolvanen, K. Hämäläinen, R. Raiko, Comparing the energy required for fine grinding torrefied and fast heat treated pine, Biomass and Bioen-

ergy 42, 2012, pp. 219-223. Available:
http://www.sciencedirect.com/science/journal/09619534

[42]   K. W. Ragland, D. J. Aerts, A. J. Baker, Properties of wood for Combustion Analysis, Bioresource Technology 37, 1991, pp. 161-168. Available: http://www.sciencedirect.com/science/article/pii/096085249190205X

[43]   H. Lu, E. Ip, J. Scott, P. Foster, M. Vickers, L. L. Baxter, Effects of particle shape and size on devolatilization of biomass particle, Fuel 89, 2010, pp. 1156-1168. Available: http://www.sciencedirect.com/science/journal/00162361

[44]   Y. B. Yang, V. N. Sharifi, J. Swithenbank, L. Ma, L. I. Darvell, J. M. Jones, M. Pourkashanian, A. Williams, Combustion of a Single Particle of Biomass, Energy & Fuels 22, 2008, pp. 306-316. Available: http://www.researchgate.net/publication/231273171_Combustion_of_a_Single_Particle_of_Biomass

[45]   A. Bharadwaj, L. L. Baxter, A. L. Robinson, Effects of Intraparticle Heat and Mass Transfer on Biomass Devolatilization: Experimental Results and Model Predictions, Energy & Fuels 18, 2004, pp. 1021-1031. Available: http://pubs.acs.org/doi/abs/10.1021/ef0340357

[46]   P. Basu, Biomass Gasification, Pyrolysis and Torrefaction, Practical Design and Theory, 2nd Edition, Elsevier, 2013, pp. 147-166.

[47]   M. G. Grönli, A Theoretical and Experimental Study of the Thermal Degradation of Biomass, dissertation, Norwegian University of Science and Technology, 1996, pp. 31-41. Available: http://www.diva-portal.org/smash/get/diva2:321540/FULLTEXT01.pdf

[48]   I. Milosavljevic, V. Oja, E. M. Suuberg, Thermal effects in cellulose pyrolysis: Relationship to char formation process. Ind. Eng. Chem. Res. Vol. 35, 1996. pp. 653-662. Available: http://pubs.acs.org/doi/pdf/10.1021/ie950438l

[49]   C. Di Blasi, Modeling chemical and physical processes of wood and biomass pyrolysis, Progress in Energy and Combustion Science 34, 2008, pp. 47-90. Available: http://www.sciencedirect.com/science/article/pii/S0360128507000214

[50]   J. Lehto, Development and Characterization of Test Reactor with Results of Its Application to Pyrolysis Kinetics of Peat and Biomass Fuels, dissertation, Tampere University of Technology, Publication 665, 2007, 101 p.

[51]   Q. Yu, C. Brage, G. Chen, K. Sjöström, Temperature impact on the formation of tar from biomass pyrolysis in a free-fall reactor, Journal of Analytical and Ap-

plied Pyrolysis 40-41, 1997, pp. 481-489. Available:
http://www.sciencedirect.com/science/article/pii/S016523709700017X

[52]   S. Li, S. Xu, S. Liu, C. Yang, Q. Lu, Fast pyrolysis of biomass in free-fall reactor
       for hydrogen-rich gas, Fuel Processing Technology 85, 2004, pp. 1201-1211.
       Available: http://www.sciencedirect.com/science/article/pii/S0378382003003151

[53]   R. Zanzi, K. Sjöström, E. Björnholm, Rapid high-temperature pyrolysis of bio-
       mass in free-fall reactor, Fuel 75, 1996, pp. 545-550. Available:
       http://www.sciencedirect.com/science/article/pii/0016236195003045

[54]   P.R. Solomon, M. A. Serio, E. M. Suuberg, Coal pyrolysis: experiments, kinetic
       rater and mechanisms, Progress in Energy and Combustion Science 18, 1992, pp.
       133-220. Available:
       http://www.sciencedirect.com/science/article/pii/036012859290021R

[55]   O. Karlström, Drying, devolatilization and char oxidation of solid fuel, Åbo
       Academi, 2013. Available:
       http://www.users.abo.fi/maengblo/FPK_I_2015/Dry_devol_char_in_solid_fuel_c
       onversion_FPK_I_2015.pdf

[56]   E. Biagini, M. Simone, L. Tognotti, Characterization of high heating rate chars
       of biomass fuels, Proceedings of the Combustion Institute 32, 2009, pp. 2043-
       2050. Available:
       http://www.sciencedirect.com/science/article/pii/S1540748908001508

[57]   J. Li, G. Bonvicini, X. Zhang, W. Yang, L. Tognotti, Char oxidation of torrefied
       biomass at high temperatures and high heating rates, Energy Procedia 61, 2014,
       pp. 582-586. Available:
       http://www.sciencedirect.com/science/article/pii/S1876610214030057

[58]   M. Geier, C. R. Shaddix, F. Holzleithner, A mechanistic char oxidation model
       consistent with observed CO_2/CO ratios, Proceedings of the Combustion Insti-
       tute 34, 2013. pp. 2411-2418. Available:
       http://www.sciencedirect.com/science/article/pii/S1540748912003008

[59]   Y. Wang, L. Yan, CFD Studies on Biomass Thermochemical Conversion, Inter-
       national Journal of Molecular Sciences 9, 2008, pp. 1108-1130. Available:
       http://www.ncbi.nlm.nih.gov/pmc/articles/PMC2658784/

[60]   P. Grammelis, Solid Biofuels For Energy, Springer-Verlag London Ltd, 2011, p.
       85.

[61]   A. F. Mills, Basic Heat and Mass Transfer 2nd Edition, Prentice Hall, 1999, pp.
       30-32.

[62]   Ansys Fluent Theory Guide, Release 15.0, 2013, pp. 385-408.

[63]   R. Weber, Combustion Fundamentals with Elements of Chemical Thermody-
        namics 2nd Edition, International studies in science and engineering, Pa-
        pierflieger, 2011, 319 p.

[64]   S. Zahirovic, R. Scharler, I. Obernberger, Advanced CFD modeling of pulver-
        ized biomass combustion, Bios Bioenergysysteme GmbH, 2004, 18 p. Available:
        http://www.bios-bioenergy.at/uploads/media/Paper-Zahirovic-
        CFDPulvBiomassComb-Vancouver-2004-09-10.pdf

[65]   R. Mehrablan, S. Stangl, R. Scharler, I. Obernberger, A. Welssinger, CFD simu-
        lation of biomass grate furnaces with a comprehensive 3D packed bed model,
        Proceedings of the 25th German Flame Day, 2011, 10 p. Available:
        http://www.bios-bioenergy.at/uploads/media/Paper-Mehrabian-3DBedModel-
        with-Layer-Model-09-2011.pdf

[66]   H. Kobayashi, Devolatilization of pulverized coal at high temperatures, Massa-
        chusetts Institute of Technology, 1976, 423 p.

[67]   D. L. Pyle, C. A. Zaror, Heat Transfer and Kinetics in the Low Temperature Py-
        rolysis of Solids, Chemical Engineering Science 39:1, 1987, pp. 147-158.

[68]   O. Karlström, A. Brink, J. Hercog, M. Hupa, L. Tognotti, Kinetic combustion
        parameters for chars using the IFRF solid fuel data base, 14 p. Available:
        http://content.lib.utah.edu:81/cgi-bin/showfile.exe?CISOROOT=/ir-
        admin2&CISOPTR=21384&filename=21101.pdf

[69]   Ultra Centrifugal Mill ZM 200, Retsch Solutions in Milling and Sieving, 2016.
        Available: http://www.retsch.com/products/miling/rotor-mills/zm-200

[70]   M. Honkanen, Direct Optical Measurement of Fluid Dynamics and Dispersed
        Phase Morphology in Multiphase Flows, dissertation, Tampere University of
        Technology, 2006, 79 p. Available:
        https://tutcris.tut.fi/portal/files/2314589/honkanen.pdf

[71]   H. Tolvanen, Advanced Solid Fuel Characterization for Reactivity and Physical
        Property comparison, dissertation, Tampere University of Technology, 2016, 66
        p. Available: https://tutcris.tut.fi/portal/files/4615590/tolvanen_1359.pdf

[72]   A. F. Mills, Basic Heat and Mass Transfer 2nd Edition, Prentice Hall, 1999, p.
        925.

[73]   A. Aho, Putoavien hiukkasten tunnistaminen ja niiden nopeuden määrittäminen kaksoisvalotetuista kuvista, bachelor's thesis, Tampere University of Technology, 2014, 18p.

[74]   H. Tolvanen, R. Raiko, An experimental study and numerical modeling of combusting two coal chars in a drop-tube reactor: A comparison between N_2/O_2, CO_2/O_2, and $N_2/CO_2/O_2$ atmospheres, Fuel 124, 2014, pp. 190-201. Available: http://www.sciencedirect.com/science/article/pii/S0016236114001227

[75]   M. G. Grönli, A Theoretical and Experimental Study of the Thermal Degradation of Biomass, dissertation, Norwegian University of Science and Technology, 1996, pp. 126-130. Available: http://www.diva-portal.org/smash/get/diva2:321540/FULLTEXT01.pdf

[76]   B. B. Nyakuma, A. Johari, A. Ahmad, T. A. T. Abdullah, Comparative Analysis of the Pyrolytic Properties of Empty Fruit Bunch Briquettes, Energy Procedia 52, 2014, pp. 466-473. Available: http://www.sciencedirect.com/science/article/pii/S1876610214009618

[77]   H. Giesche, Mercury Porosimetry: a General (Practical) Overview, Particle & Particle Systems Characterization 23, 2006, pp. 1-11. Available: http://people.alfred.edu/~giesche/Publications_files/06-1-PPSC%20%28Hg-poro%20practical%29.pdf

[78]   N. Niemelä, Computational fluid dynamics modeling of pulverized biomass combustion using optimized reactivity parameters, Master of science thesis, Tampere University of Technology, 2016, Available: https://dspace.cc.tut.fi/dpub/handle/123456789/23832

[79]   A. F. Mills, Basic Heat and Mass Transfer 2nd Edition, Prentice Hall, 1999, p. 517.

APPENDIX A: THE CODE FOR PARTICLE COMBUSTION MOD-EL

```
function [time, T_p, X, X_daf, X_daf_pyr, X_daf_co, d_p, vel_p] = ...
    hiukkanen(n, dl, d_p0, v_0, v_fin, gamma, beta, delta, alfa1, alfa2,
A1,...
    E1, A2, E2, C1, C2, Er, Vol, Ash, Y_ox, Tw_initial, Tw_final,...
    Tg_initial, Tg_final, tau_w, tau_g, C_sw, roo_p, c_p, k_p, vel_s, Pr,...
    nyy, T_pyr, dh_pyr, dh_co)

d_p = d_p0*ones(n,1);
m_p0 = 4*pi*d_p0^3/(8*3)*roo_p;
eps = 0.9;
stef = 5.67*10^-8;
Ru = 8.314;
m_ash = Ash*m_p0;
p0 = 101300;
p_ox = Y_ox*p0;
T_p = zeros(n,1);
T_p(1,1) = 293;
m_p = zeros(n,1);
m_p(1,1) = m_p0;
dm_pyr = zeros(n,1);
dm_co = zeros(n,1);
R1 = zeros(n,1);
R2 = zeros(n,1);
cum_sum = 0;
X_daf = zeros(n,1);
X_daf_pyr = zeros(n,1);
X_daf_co = zeros(n,1);
sum_pyr = zeros(n,1);
D0 = zeros(n,1);
R = zeros(n,1);
sum_co = zeros(n,1);
X_daf_max = 1;
X = zeros(n,1);
theta = zeros(n,1);
Re_d = vel_s*d_p0/nyy;
Nu = 2.0 + 0.6*Re_d^0.5*Pr^(1/3);
hc = zeros(n,1);
hc(1) = Nu*0.0559/d_p0;
hs = zeros(n,1);
Sc = zeros(n,1);
Sc(1) = nyy/d_p0;
Bi = zeros(n,1);
Bi(1) = hc(1)*d_p0/2/k_p;
vel_p = (v_0 + (gamma*exp(-0/beta))*(-0/beta) - (v_0 - v_fin)*(1 - exp(-
0/delta)))*ones(n,1);
l = zeros(n,1);
time = zeros(n,1);
j = 0;
for i=2:n
    l(i) = l(i-1) + dl;
    dist = l(i);
    vel_p(i) = v_0 + (gamma*exp(-(dist)/beta))*(-(dist)/beta) - (v_0 -
v_fin)*(1 - exp(-(dist)/delta));
    dt = dl/vel_p(i-1);
```

```
    time(i) = time(i-1) + dt;
    T_w = Tw_initial + (1-exp(-dist/tau_w)) * (Tw_final-Tw_initial);
    T_g = Tg_initial + (1-exp(-dist/tau_g)) * (Tg_final-Tg_initial);
    if T_p(i-1) > T_pyr
        if m_p(i-1) > m_p0 - 0.99*Vol*m_p0
            R1(i) = A1*exp(-E1/(Ru*T_p(i-1)));
            R2(i) = A2*exp(-E2/(Ru*T_p(i-1)));
 cum_sum = cum_sum + (R1(i) + R2(i))*dt;
            X_daf_pyr(i)    =    X_daf_pyr(i-1)    +    ((alfa1*R1(i)    +    al-
fa2*R2(i))*exp(-cum_sum))*dt;
            if (X_daf_pyr(i) > Vol/(1-Ash)) || (exp(-cum_sum)<0.01)
                X_daf_pyr(i) = Vol/(1-Ash);
                j=1;
            end
            d_p(i) = d_p0*(1 + (C_sw - 1)*(m_p0 - m_p(i-1))/(Vol*m_p0));
            sum_pyr(i) = (m_p0 - m_ash)*X_daf_pyr(i);
            dm_pyr(i) = sum_pyr(i) - sum_pyr(i-1);
        else
            X_daf_pyr(i) = Vol/(1-Ash);
            sum_pyr(i) = (m_p0 - m_ash)*X_daf_pyr(i);
            dm_pyr(i) = sum_pyr(i) - sum_pyr(i-1);
            d_p(i) = d_p0*(1 + (C_sw - 1)*(m_p0 - sum_pyr(i))/(Vol*m_p0));
            if j>0
                d_p(i) = d_p(i-1);
                D0(i) = C1*((T_p(i-1) + T_g)/2)^0.75/d_p(i-1);
                R(i) = C2*exp(-Er/(Ru*T_p(i-1)));
                dm_co(i)    =    (pi*d_p(i-1)^2)*p_ox*(D0(i)*R(i)/(D0(i)    +
R(i)))*dt;
                sum_co(i) = sum_co(i-1) + dm_co(i);
                X_daf_co(i) = sum_co(i)/(m_p0 - m_ash);
            end
            j = 1;
            if X_daf_pyr(i) + X_daf_co(i) > X_daf_max
                dm_co(i) = (m_p0 - m_ash - sum_co(i-1) - sum_pyr(i));
                sum_co(i) = sum_co(i-1) + dm_co(i);
                X_daf_co(i) = sum_co(i)/(m_p0 - m_ash);
            end
        end
    else
        X_daf_pyr(i) = X_daf_pyr(i-1);
        X_daf_co(i) = X_daf_co(i-1);
        sum_pyr(i) = sum_pyr(i-1);
        dm_pyr(i) = 0;
    end
    X_daf(i) = X_daf_pyr(i) + X_daf_co(i);
    m_p(i) = m_p(i-1) - dm_pyr(i) - dm_co(i); %
    X(i) = 1 - m_p(i)/m_p0;
    Re_d = vel_s*d_p(i)/nyy;
    Nu = 2.0 + 0.6*Re_d^0.5*Pr^(1/3);
    hc(i) = Nu*0.0559/d_p(i);
    Sc(i) = nyy/d_p(i);
    Bi(i) = hc(i)*d_p(i)/2/k_p;
    ap = (hc(i)*(pi*d_p(i)^2)*T_g + (pi*d_p(i)^2)*eps*stef*T_w^4)/...
        (hc(i)*(pi*d_p(i)^2)+eps*(pi*d_p(i)^2)*stef*T_p(i-1)^3);
    bp = (pi*d_p(i)^2)*(hc(i) + eps*stef*T_p(i-1)^3)/(m_p(i-1)*c_p);
    T_p(i) = ap + (T_p(i-1) - ap)*exp(-bp*dt);
    if T_p(i) < T_p(1)
        T_p(i) = T_p(i-1);
    end
```

```
    end
    end
```

APPENDIX B: OPTIMIZATION PROCEDURE OF TWO-COMPETING RATES PYROLYSIS MODEL

```matlab
for j=1:23
    if mod(j,4) == 0
        C_sw = 1;
    else
        C_sw = 0.9;
    end
    kinetics_pyr_initial = [A1, E1, A2, E2, alfa1, alfa2];
    fun = @(p)errorpyr( p, n, dl, d_p1, v_0, v_fin, gamma, beta, ...
        delta, Vol, Ash, tw_init, tw_fin, tg_init, tg_fin, tau_w, tau_g,
C_sw,...
        x600, X600, x900, X900, roo_p, c_p, k_p, vel_s, Pr,...
        nyy, T_pyr, dh_pyr, dh_co, limit);
    [p,fval] = fminsearch(fun, kinetics_pyr_initial, optionsf);
    alfa1 = p(5); alfa2 = p(6);
    A1 = p(1); E1 = p(2); A2 = p(3); E2 = p(4);
end
function [ error ] = errorpyr( p, n, dl, d_p1, v_0, v_fin, gamma, beta, ...
    delta, Vol, Ash, tw_init, tw_fin, tg_init, tg_fin, tau_w, tau_g, C_sw,...
    x600, X600, x900, X900, roo_p, c_p, k_p, vel_s, Pr, nyy, T_pyr, dh_pyr,
dh_co, limit)
size_classes = length(d_p1);
Xerror = 0;
X_avg = zeros(n,1);
d_pavg = zeros(n,1);
for j = 1:2
    for i=1:size_classes
        [time, T_p, X, X_daf, X_daf_pyr, X_daf_co, d_p, vel_p] = ...
            hiukkanen(n, dl, d_p1(i), v_0, v_fin, gamma, beta, delta, p(5),
p(6), p(1),...
            p(2), p(3), p(4), 1, 1, 1, Vol, Ash, 0, tw_init(j),...
            tw_fin(j), tg_init(j), tg_fin(j), tau_w(j), tau_g(j), C_sw,
roo_p,...
            c_p, k_p, vel_s, Pr, nyy, T_pyr, dh_pyr, dh_co);
        X_avg = X_avg + 1/size_classes*X(:,1);
    end
    if j == 1
        Xm = X600;
        xm = x600;
        weight = 1;
    else
        Xm = X900;
        xm = x900;
        weight = 4;
    end
    for k = 1:length(Xm)
        if isnan(xm(k)) == false && isnan(Xm(k)) == false
        indeks = round(xm(k)/dl);
        Xerror = Xerror + weight*(100*(X_avg(indeks) - Xm(k)))^2;
        end
    end
        X_avg = zeros(n,1);
    d_pavg = zeros(n,1);
end
```